POLITECNICO DI MILANO

FACOLTÀ DI INGEGNERIA INDUSTRIALE

Corso di Laurea Magistrale in
Ingegneria Meccanica

Numerical investigation of the solidity effect on a linear compressor cascade performance and stability

Prof. Giacomo Bruno Persico
Prof. Jean François Brouckaert

Tesi di Laurea di:
Matteo Resmini Matr.:755188

Anno Accademico 2011/2012

Riassunto

La riduzione delle emissioni di sostanze inquinanti e di rumore, insieme con la ricerca delle massime prestazioni sono sfide che richiedono ai progettisti di motori non solo lo sviluppo di nuove architetture e soluzioni costruttive, ma anche l'ottimizzazione degli strumenti di progettazione ed il consolidamento delle correlazioni utilizzati per determinare le scelte progettuali. In un compressore assiale la solidity rappresenta il rapporto fra la corda aerodinamica ed il passo interpalare ed è dunque legata al numero di pale e quindi al peso dello stadio. Il presente studio, sviluppato all'interno di una collaborazione fra il Von Karman Insitute for Fluid Dynamics e l'azienda privata Techspace Aero, analizza l'effetto di solidità sulle performance e sulla stabilità di una schiera piana in regime transonico. Le principali correlazioni di letteratura sono utilizzate per analizzare l'effetto della solidity su deviazione, incidenza e perdite, considerando anche alcune problematiche legate alla ricerca di una condizione di efficienza ottima. Si propone quindi un approccio numerico per l'analisi, utilizzando un modello CFD sviluppato con il software FINE/Turbo di Numeca International. Il modello è messo a punto attraverso uno studio di sensitività sulla mesh e sul modello di turbolenza. Si analizzano otto diverse configurazioni di passo e corda, che permettono di valutare 5 diversi valori di solidity e i differenti effetti di una riduzione di corda rispetto ad un aumento del passo. Il range di incidenza testato si estende dal choke allo stallo per numeri di Mach in ingresso che variano da 0.4 a 0.8. Tre diversi modelli di turbolenza sono messi a confronto, così come due diverse tipologie di condizioni al contorno. Dal momento che a valle del presente studio sarà realizzata una campagna sperimentale del modello simulato, l'analisi è volta anche a sottolineare gli aspetti critici per la messa a punto dei futuri test.

I. Introduzione

La solidity è il rapporto fra la corda aerodinamica e il passo interpalare. La determinazione di questa grandezza rappresenta uno dei primi passi da compiere nell'iter progettuale di una schiera e le implicazioni che essa determina sul carico palare rendono la sua scelta un aspetto critico. Nonostante siano stati perpetrati alcuni tentativi alla ricerca di una condizione di ottimo, in termini di carico o di efficienza, non è disponibile alcuna regola generale per la determinazione di questo parametro.

Nelle ultime decadi, i requisiti sempre più stringenti in termini di carico hanno orientato i progettisti a valori di solidity sempre crescenti, come illustrato in Figura 1. Questa scelta risulta essere in gran parte determinata dall'utilizzo di profili a corda lunga, per i quali numerose evidenze sperimentali dimostrano migliori performance in termini di stabilità e perdite legate ai flussi secondari. L'allungamento della corda è tuttavia limitato dal vincolo sull'estensione assiale della macchina. Nella stessa direzione la riduzione del passo e quindi l'aumento del numero di pale, potrebbe consentire ulteriori benefici. Il vero limite di queste due linee progettuali è tuttavia rappresentato dal loro impatto sul peso della macchina e alle dirette conseguenze sul consumo di combustibile ed emissione di inquinanti. La comprensione dei costi e dei benefici derivanti dalla scelta di questi parametri risulta quindi essenziale per una buona progettazione.

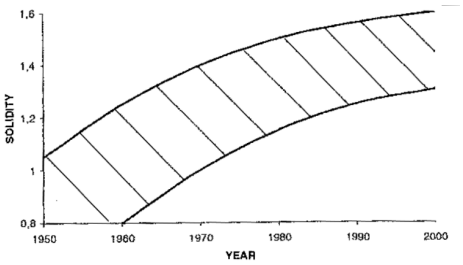

Figura 1: *Andamento storico dei valori di solidity*

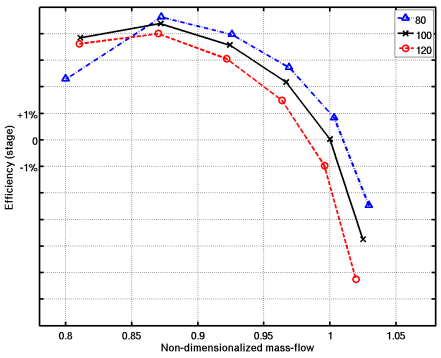

Figura 2: *Efficienza dello statore del booster di TSAper diversi numeri di pale*

Uno studio numerico preliminare (ref. [1]) su un primo stadio di compressione progettato e realizzato da TechspaceAero (TSA), ha evidenziato l'opportunità di mantenere un alto livello di prestazioni riducendo la solidity dello statore, seppur accettando una riduzione dei margini operativi, come mostrato in Figura 2. A valle di questi incoraggianti risultati si rende necessaria un'analisi più approfondita dell'effetto della solidity sulle prestazioni e sulla stabilità di una schiera, al fine di formalizzare e verificare correlazioni utilizzabili nel corso della progettazione. Numerosi sforzi e risorse sono state dedicate in passato allo studio del problema, da parte dei principali istituti di ricerca del mondo; ciononostante non sono ad oggi disponibili correlazioni di validità generale che permettano di descrivere gli effetti della solidity in forte regime di comprimibilità.

A partire da un'analisi delle ricerche già svolte, il presente studio si prefigge l'obiettivo di analizzare le prestazioni ed il campo operativo di otto diverse configurazioni di passo e di corda (Tab. 1) attraverso un approccio numerico, che non risulta finora intrapreso nello studio del problema. I risultati del modello numerico saranno confrontati con le correlazioni storiche anche per valutare l'introduzione di possibili modifiche a queste ultime per l'adattamento al tipo di profilo e al regime di flusso di interesse.

σ		s (mm)			
		24	26.74	30.2	34.67
c (mm)	33.09	**1.38**	**1.24**	**1.10**	**0.95**
	29.7	**1.24**	*1.11*	*0.98*	*0.86*
	26.3	**1.10**	*0.98*	*0.87*	*0.76*
	22.91	**0.95**	*0.86*	*0.76*	**0.66**

Tabella 1: *Valori di solidity testati (in grassetto)*

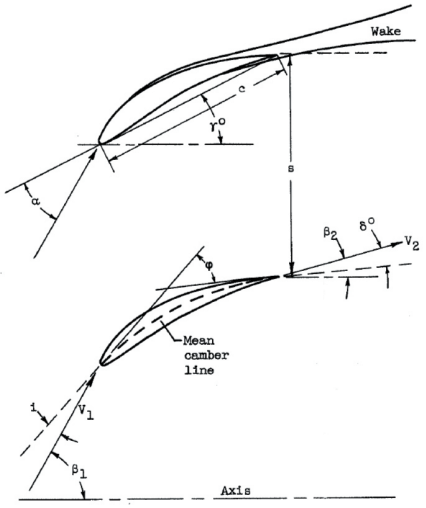

Figura 3: *Geometria di una schiera piana*

II. Rassegna bibliografica

Fin dagli albori della moderna storia delle turbomacchine la spaziatura delle pale è riconosciuta come un elemento di primaria importanza per la progettazione di un compressore: si consideri a questo proposito il brevetto depositato da Sir Parsons nel 1902 (ref. [2]). Le principali ricerche sull'argomento, di carattere prettamente sperimentale, sono sviluppate a partire dagli anni sessanta su schiere piane e anulari; si riportano in questa sezione le principali correlazioni e risultati, riguardanti l'effetto di solidità sull'angolo del flusso allo scarico e sulle prestazioni della schiera, rimandando al testo della tesi per un'analisi completa e dettagliata.

II.I Correlazioni per schiere piane

La notazione geometrica è riportata in Figura 3; sono state utilizzate le convenzioni in conformità con il documento NASA SP-36 (ref. [3]). Le seguenti correlazioni sono valide generalmente in condizione "di progetto", definita da Howell come l'80% della deflessione di stallo e dagli altri autori come l'incidenza media fra stallo destro e sinistro, sovente non lontano dalla condizione di minimo del coefficiente di perdita definito come segue:

$$\omega = \frac{p_{02} - p_{01}}{p_{02} - p_{s1}} \tag{1}$$

Per quanto riguarda l'effetto della solidity sulla deviazione, è possibile fare riferimento essenzialmente alle correlazioni di Howell, Carter e Lieblein. Laddove il primo, a valle di una serie di studi teorici individua una relazione fra la tangente degli angoli in ingresso e in uscita della schiera:

$$\tan(\beta_1) - \tan(\beta_2) = \frac{1.55}{1 + \frac{1.5}{\sigma}} \tag{2}$$

il secondo esplicita anche la dipendenza dalla forma della linea media e dell'angolo di calettamento e una dipendenza lineare con l'inarcamento del profilo, così come descritto dalla seguente relazione

$$\delta = m\phi \left(\frac{1}{\sigma}\right)^n \tag{3}$$

Il coefficiente n è posto pari a 1 per turbine e a $1/2$ per compressori. Rispetto alla semplicità dell'espressione di Carter, le correlazioni di Lieblein presentano una formulazione più complessa che presenta tuttavia il pregio di una validità più generale: vengono infatti introdotti nel calcolo anche parametri legati allo spessore del profilo nonché al valore dell'angolo in ingresso, rappresentati nella seguente formula all'interno dei coefficienti b e δ_0 ed m, generalmente forniti attraverso dei grafici:

$$\delta = \delta_0 + \frac{m\ \phi}{\sigma^b} \tag{4}$$

La solidity gioca inoltre un ruolo fondamentale nella determinazione del carico palare, la cui quantificazione risulta esseziale per descrivere il comportamento della pala e il margine rispetto alla condizione di stallo. Un primo approccio alla caratterizzazione del carico fu teorizzato da Zweifel nel 1945; esso è basato sulla comparazione del coefficiente di portanza della pala e di un coefficiente di portanza ideale basato sulla velocità di scarico. Tale coefficiente può essere espresso nella seguente forma:

$$\Psi_a = \frac{\Delta v_\theta\ (v_1 + v_2)}{\sigma v_2^2} \tag{5}$$

Il grafico in Figura 4 presenta il rapporto fra il coefficiente di portanza e di resistenza in funzione del coefficiente di Zweifel. Le curve relative a diverse

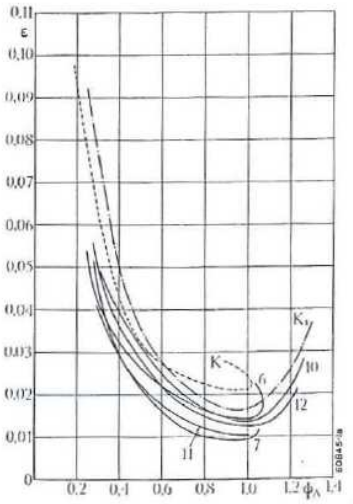

Figura 4: *Finezza dela profilo in funzione del coefficiente di Zweifel*

schiere sono molto raggruppate a testimonianza della buona indipendenza di questo parametro rispetto agli angoli in ingresso ed uscita. Si osserva inoltre, fra i valori 0.9 e 1.1, una condizione di minimo che può essere utilizzata per definire una condizione di ottimo per la solidity. Anche se questo parametro è stato definito principalmente a partire da prove su stadi di turbina, numerosi sono gli esempi dell'utilizzo di questo criterio anche per compressori (ref. [4],[5] et al.)

Il criterio di Carter si basa sulla definizione di una condizione ideale di spessore del bordo di uscita della pala nullo:

$$C_{L,V_{20}} = 2\frac{1}{\sigma}\left(\frac{s}{s'}\right)^2 (\tan\beta_1 - \tan\beta_2)\,\frac{\cos^2\alpha_2}{\cos\alpha_\infty} \tag{6}$$

dove s' rappresenta il passo effettivo della pala $s' = s - t_\theta$, con $t_\theta = t_n / \cos\beta_\infty$; imponendo un limite a questo coefficiente, è possibile valutare la solidity:

$$C_{L,V_{20}} \leq 1.35 \tag{7}$$

Il maggior contributo alla comprensione e rappresentazione del problema è rappresentato dal lavoro di Lieblein e dalla definizione del diffusion factor, riportata nel 1953 (ref. [6]). Lo studio è basato sulla teoria dello strato limite e mette in relazione le dissipazioni con i gradienti di velocità sulla pala nelle regione di diffusione. Frutto di un primo tentativo in questa direzione è la definizione di un fattore di diffusione locale, basato sulla differenza fra la massima velocità sul profilo e la velocità allo scarico:

$$D_{loc} = \frac{v_{max} - v_2}{v_2} \tag{8}$$

La complessità del calcolo di questo parametro e la sua scarsa praticità hanno portato ad una definizione basata esclusivamente sui flussi in ingresso e in

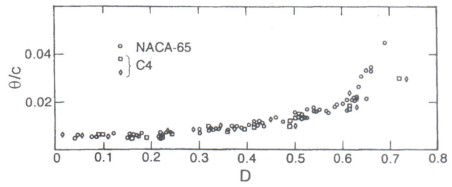

Figura 5: *Spessore di quantità di moto in funzione del diffusion factor per diverse tipologie di schiera*

uscita dalla schiera:

$$DF = \left(1 - \frac{v_2}{v_1}\right) + \frac{\Delta v_\theta}{2\, v_1\, \sigma} \tag{9}$$

Lo spessore di quantità di moto viene successivamente messo in relazione con il fattore di diffusione per diverse tipologie di schiera; dai risultati riportati in Figura 5, è possibile osservare un aumento marco delle perdite a partire da un valore del fattore di diffusione pari a 0.6: questa condizione può quindi essere considerata per indicare lo stallo incipiente. Per esprimere direttamente le perdite a partire dallo spessore di quantità di moto è possibile utilizzare tre diversi parametri, qui riportati in ordine crescente di complessità di calcolo e accurattezza:

$$\zeta_1 = \frac{\theta}{c} \approx \frac{\omega\, \cos\beta_2}{2\,\sigma} \tag{10}$$

$$\zeta_2 = \frac{\theta}{c} \approx \frac{\omega\, \cos\beta_2}{2\,\sigma} \left(\frac{\cos\beta_2}{\cos\beta_1}\right)^2 \tag{11}$$

$$\zeta_3 = \frac{\theta}{c} \approx \frac{\omega\, \cos\beta_2}{2\,\sigma} \left(\frac{v_1}{v_2}\right)^2 \tag{12}$$

La definizione 10 risulta, grazie alla sua semplicità, la più utilizzata; il suo comportamento, riportato in Figura 6(b), presenta un andamento piatto fino a $DF = 0.6$. Il parametro ζ_2 risulta più indicativo della condizione di stallo, perchè più sensibile all'incremento di diffusione.

Un ulteriore apporto all'analisi del problema della solidity fu fornito nuovamente dallo stesso Lieblein nel 1959 (ref. [7]) attraverso la definizione di un rapporto di diffusione equivalente (D_{eq}), che permette di esprimere attraverso una relazione empirica la dipendenza delle perdite dal rapporto fra le velocità assiali, dall'incidenza e, ancora una volta, dalla solidity e dalla differenza delle velocità tangenziali. Numerosi autori hanno in seguito elaborato modelli per la descrizione delle perdite basati su questo fattore. Si ricordano in particolare i modelli di Koch e Smith (1976, ref. [8]) e di Wright e Miller (1991, ref. [9]). Si riporta di quest'ultimo la dipendenza delle perdite dal rapporto di diffusione equivalente in Figura 7; la dipendenza del numero di Mach risulta evidente, in accordo con evidenze sperimentali presentate da altri autori (Heilmann et al., 1968, ref. [10]).

A valle di questi risultati è possibile delineare due condizioni antitetiche:

- **σ elevata**: DF ridotto, perdite elevate (ampie superfici bagnate), rapporto di diffusione ridotto e, di conseguenza, ampio margine di stallo

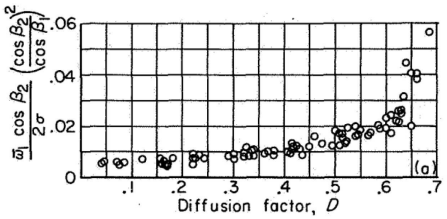

(a)

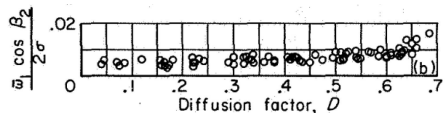

(b)

Figura 6: *Differenti espressioni di spessore di quantitià di moto in funzione del diffusion factor*

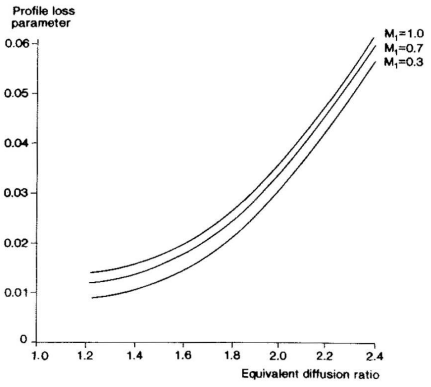

Figura 7: *Modello di Wright e Miller, spessore di quantità di moto in funzione del fattore di diffusione equivalente e del numero di Mach*

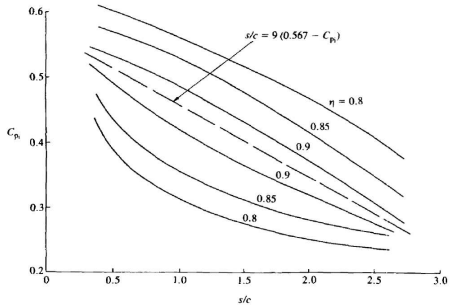

Figura 8: *Coefficiente di pressione di McKenzie per diversi valori di solidity*

- σ **ridotte**: DF elevato, riduzione delle perdite per superfici bagnate e aumento delle perdite di profilo; riduzione del margine di stallo

Una condizione di minima perdita risulta quindi intuitivamente presente.

II.II Solidity ottima

Come anticipato nel precedente paragrafo, per il calcolo di una solidity è possibile utilizzare le relazioni di Zweifel, o Carter imponendo un limite al fattore di carico della pala. Tale relazioni, tuttavia, non sono stati elaborati studiando specificamente gli effetti sulle perdite.

Negli anni '80 McKenzie (ref. [11] e [12]) elabora un differente approccio al problema, correlando la condizione di ottimo con un rapporto di pressione statica ideale, così definito:

$$C_{p_i} = \frac{p_{s2} - p_{s1}}{1/2\,\rho_1 v_1^2} = 1 - \frac{\rho_2}{\rho_1}\left(\frac{v_2}{v_1}\right)^2 \tag{13}$$

Il valore di rapporto passo corda ($\frac{1}{\sigma}$ per cui si registra la massima efficienza risulta essere funzione lineare del rapporto di compressione statico, secondo laa relazione:

$$\frac{s}{c} = 9\,\left(0.567 - C_{p_i}\right) \tag{14}$$

così come riportato in Figura 8.

Nello stesso periodo Hearsey (ref. [13]) propone un calcolo della solidity ottimale basato sull'annullamento della derivata di ζ_1 e ζ_2 rispetto a DF. Le seguenti interpolazioni vengono proposte:

$$\zeta_1 = 0.004 + 0.004722\,DF + 0.095679 DF^3 \tag{15}$$

$$\zeta_2 = 0.004\,e^{6.16773\,DF^{1.436794}} \tag{16}$$

Imposti i triangoli delle velocità, il fattore di diffusione -e quindi le perdite- è esclusivamente funzione della solidity, e risulta possibile quindi individuare la condizione di minima perdita.

Nel 1993, Liu propone i risultati di uno studio teorico (ref. [14]) che mette in luce il duplice problema legato alla condizione di ottima solidity per una schiera piana:

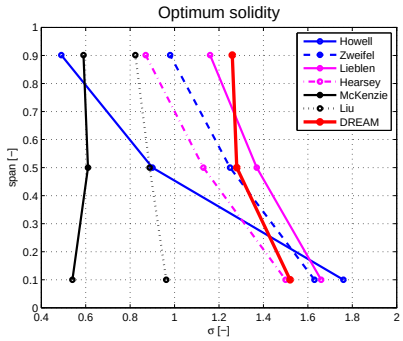

Figura 9: *Valori di ottima solidity per diverse altezze di pala secondo diversi autori*

1. minimizzazione delle perdite
2. massimizzazione della circolazione intorno al profilo (che massimizza il carico del profilo)

Alcuni vincoli vengono imposti al valore del fattore di diffusione e alcune semplici equazioni vengono proposte per il calcolo della solidity ottima.

In Figura 9 è riportato il confronto di diversi metodi per il calcolo della solidity ottimale applicati in tre diversi punti lungo l'altezza di pala di uno statore rappresentativo dello statore dell'arte ed indica in legenda con l'etichetta "DREAM". A corredo del grafico è possibile notare i seguenti commenti:

- I valori suggeriti da McKenzie e Liu risultano molto inferiori rispetto allo stato dell'arte
- I valori calolati attraverso la correlazione di Howell (eq. 2) risultano essere molto variabili fra apice e radice della pala
- I valori proposti da Lieblein, Zweifel, Hearsey sono coerenti con la configurazione dello statore DREAM
- Mentre le correlazioni di Zweifel e Lieblein consentono un adattamento e un controllo del carico lungo l'altezza di pala, i metodi di Hearsey e McKenzie sono strettamente legati alla condizione di minima perdita su cui sono centrati

II.III Schiere anulari

Si riportano le conclusioni comuni alle numerose prove sperimentali su schiere anulari studiate e riportate con maggiori dettagli nell'elaborato di tesi:

1. il rapporto di compressione cresce con la solidity, poichè il flusso risulta maggiormente guidato
2. l'incidenza di stallo cresce con la solidity, grazie alla riduzione del carico palare
3. a causa della riduzione di superficie bagnata, l'efficienza cresce al diminuire della solidity
4. la portata fluente si riduce al crescere della solidity a causa del maggior effetto di bloccaggio delle pale

Quantity	Maxim. uncertainty
α_2	0.3°
P_{T1}	50 Pa
P_{T2}	200 Pa (3 hole prb.)
P_S	50 Pa
T_T	1°
M_1	$2.5E-4$
M_2	$3.2E-4$
PR	$9.7E-4$
ω	$6E-3$

Tabella 2: *Valori di incertezza utilizzati per lo sviluppo del modello*

III. Sviluppo del modello

Il modello è stato preparato e testato utilizzando la suite di programmi CFD di NUMECA International; per processare i dati si è inoltre fatto ricorso all'uso del software MATLAB di Mathworks.

Nella fase di messa a punto del modello si è tenuto conto di due fondamentali esigenze: da un lato l'accuratezza dei risultati e dall'altro la minimizzazione del tempo di calcolo. Per quanto riguarda il primo requisito si è scelto, anziché ricercare il valore asintotico, di raffinare la mesh in modo tale che l'incertezza dei risultati calcolati sia confrontabile con quella attesa per i risultati sperimentali che verranno misurati in futuro (cfr. Tabella 2). L'esigenza di minimizzare il costo computazionale è dettata da un lato, dal procedimento iterativo legato alla determinazione del numero di Mach in ingresso che non può essere imposto direttamente ma deve essere estrapolato dalla pressione totale e, dall'altro, dal consistente numero di simulazioni da effettuare (9 valori di incidenza per 5 diversi numeri di Mach per 8 diverse configurazioni di passo e corda per ciascuno dei 3 modelli di turbolenza testati).

Il modello geometrico testato è rappresentato in Figura 10, ed è costituito da una pala di sezione costante lungo l'altezza; le sezioni di ingresso e di uscita sono poste ad una distanza pari ad una lunghezza di corda dal bordo di attacco e dal bordo di uscita della pala.

III.I Condizioni al contorno e schema numerico

Sulla sezione di ingresso vengono imposti la pressione e la temperatura totali e la direzione del flusso in ingresso. Sulla sezione in uscita viene imposto il valor medio della pressione statica, pari alla pressione atmosferica rispettando l'equilibrio radiale. Sulla superficie palare è sempre imposta una condizione adiabatica e no-slip. Una condizione di periodicità è imposta sulle superfici interpalari mentre sulle superfici piane è imposta una condizione di adiabaticità

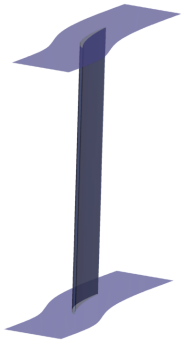

Figura 10: *Geometria del modello*

e vengono inoltre considerate sia condizioni slip (euler walls) che no-slip (navier-stokes walls).

Per tutte le simulazioni effettuate si utilizza uno schema centrale per le sue caratteristiche di robustezza e generalità, dal momento che la topologia del flusso è incognita.

III.II Mesh

La discretizzazione del modello è risultato di uno studio di sensitività compiuto su quindici diverse configurazioni di alcuni parametri ritenuti essenziali per la descrizione dei fenomeni di interesse, in particolare:

1. numero complessivo di celle
2. discretizzazione lungo l'altezza di pala
3. discretizzazione nel piano blade to blade
4. y^+ sulle superfici piane (hub e shroud)
5. y^+ sulla superficie palare

Per quanto riguarda la topologia della mesh è stato scelto uno schema O4H, che consente la discretizzazione automatica ed è molto flessibile rispetto all'applicazione per cui viene utilizzata. L'analisi è stata eseguita utilizzando il modello di turbolenza $\kappa - \varepsilon$ nella versione di Yang Shih (YS). Tutte le simulazioni sono state effettuate imponendo condizioni al contorno sulle superfici piane sia slip che no-slip. Si è considerata una condizione $M_1 = 0.5$ e di incidenza $i = -1.5°$.

Per analizzare i risultati sono stati considerati tre differenti aspetti: l'effetto delle modifiche sui parametri di qualità della mesh (Rapporto di forma, di espansione, indice di skewness), la velocità e la qualità della convergenza dei residui, della portata e del rapporto di compressione ed infine l'impatto sulle prestazioni (perdite, rapporto di compressione, Mach e angolo del flusso allo scarico) calcolate come media pesata sulla massa sull'intera superficie (valore "globale") e a metà altezza del canale (valore "locale"). A titolo di esempio si riporta la dipendenza dei rapporti di compressione statico e totale dalla

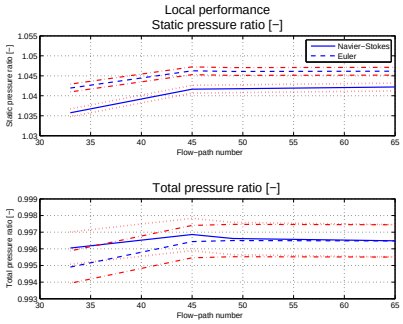

Figura 11: *Effetto della discretizzazione lungo l'altezza di pala sui rapporto di pressione statica e totale*

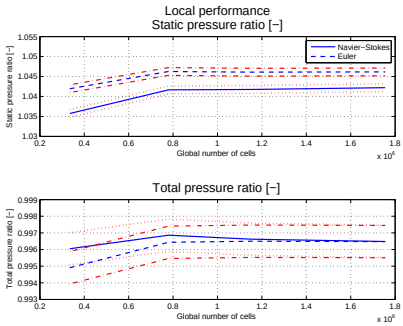

Figura 12: *Effetto del numero di celle sui rapporto di pressione statica e totale*

discretizzazione sul piano interpalare e dal numero totale di celle. Sui grafici sono anche riportate le fasce di incertezza previste.

L'analisi di sensitività ha quindi permesso di determinare le caratteristiche del modello riportate in Tabella 3, mentre in Figura 13 è riportata la topologia della mesh. Nelle configurazioni che prevedono una riduzione di corda il numero di celle della mesh e le altre caratteristiche rimangono invariate, determinando una discretizzazione più raffinata del dominio; l'analisi di sensitività ha permesso di garantire che questo "infittimento indotto" non compromette la comparabilità dei risultati.

III.III Modello di turbolenza

Nella fase di messa a punto del modello sono stati analizzati gli effetti di 5 modelli di turbolenza:

- ✓ Baldwin Lomax (Zero-equations)
- ✓ Spalart Allmaras (One-equation)
- ✓ Yang Shih (two-equations, $\kappa - \varepsilon$)
- ✓ Shear Stress Transport (SST) (two-equations, $\kappa - \omega$)

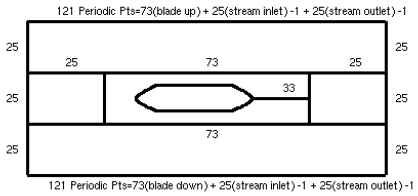

Figura 13: *Topologia della mesh sul piano interpalare*

Grandezza	**Valore**
Numero totale di celle	800000
Dimensione minima cella	10^{-6} mm[a]
Discretizzazione span	45
Min. Skewness	48.233
Max Aspect Ratio	13430
Max Expansion Ratio	1.61

[a] Tale dimensione determina un valore di y^+ largamente inferiore all'unità su ogni superficie del modello.

Tabella 3: *Caratteristiche della mesh*

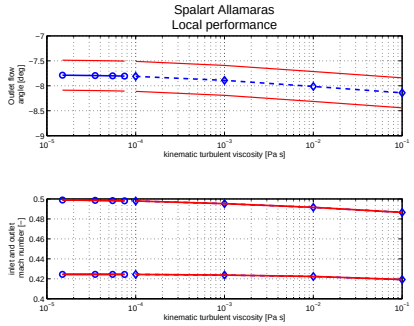

Figura 14: *Effetti del modello di turbolenza su angolo di flusso allo scarico e Mach in ingresso ed uscita*

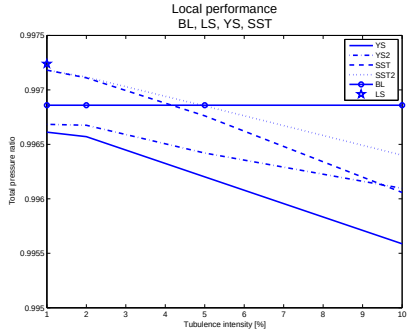

Figura 15: *Rapporto di pressioni totali secondo diversi modelli di turbolenza*

✗ Launder Sharma (two-equations, $\kappa - \varepsilon$)

Per il modello Baldwin Lomax (BL) non è possibile imporre alcun valore di intensità di turbolenza, pertanto si è assunto che i risultati con esso calcolati fossero indipendenti da questa grandezza; il modello ad una equazione permette l'imposizione di una viscosità turbolenta; non è stato tuttavia possibile valutare una relazione generale per legare questa grandezza all'intesità di turbolenza e di conseguenza non è possibile confrontare i risultati ottenuti con questo modello con gli altri. A titolo di esempio si riporta in Figura 14 la dipendenza dell'angolo del flusso in uscita e dei numeri di Mach in ingresso ed in uscita dalla viscosità turbolenta con i relativi intervalli di incertezza.

Tutti i modelli a due equazioni sono stati testati per valori di intensità di turbolenza pari a 1%, 2%, 5% e 10% ad eccezione del modello di Launder and Sharma, per cui la convergenza è garantita solo per il valore minimo. Si riporta a titolo di esempio la variazione del rapporto di pressioni totali per diversi modelli di turbulenza in funzione dell'intensità di turbolenza per diversi valori di condizioni al contorno imposte.

Questa analisi ha permesso di stabilire che le grandezze di interesse possono essere considerate indipendenti dall'intensità di turbolenza e ha consentito si

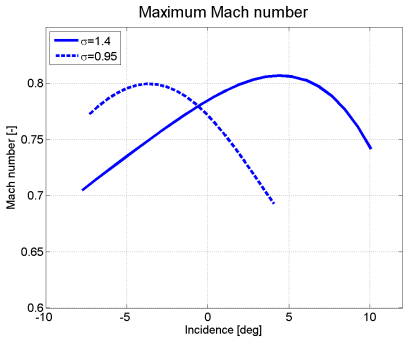

Figura 16: *Massimo numero di Mach raggiungnto in due diverse configurazioni di solidity*

individuare i modelli di turbolenza con cui effettuare l'analisi; l'analisi delle prestazioni ed il confronto con i dati di lettera sono realizzati con il modello SST per la sua solidità e il tradizionale impiego in campo turbomacchinistico; la buona esperienza riportata sia all'interno del gruppo di lavoro, sia nel contesto aziendale con il modello YS hanno destato l'interesse per un confronto dei risultati. L'analisi è stata effettuata anche con il modello BL che, nonostante la sua semplicità e l'alto grado di approssimazione dei risultati, viene talvolta impiegato per la sua solidità ed il ridotto costo computazionale.

IV. Risultati

Si è scelto di mantenere come riferimento i risultati del modello SST sia per quanto riguarda l'analisi delle prestazione al variare dell'incidenza e del numero di Mach, sia per quanto riguarda il confronto con le principali correlazioni e gli effetti si una variazione di corda piuttosto che di passo. Infine tali risultati vengono confrontati con quelli degli altri due modelli.

IV.I Intervalli di incidenza e numero di Mach considerati

La variazione del numero di Mach in ingresso imposta è legata alle condizioni di funzionamento dello stadio, che è compresa fra 0.45 e 0.6; per garantire una estensione della validità dei risultati e del loro campo di applicabilità, è stata operata un'estensione fra 0.4 e 0.8; in condizioni di incidenza molto positiva e molto negativa non è stato tuttavia possibile raggiungere l'estremo superiore, a causa delle condizioni di incipiente choke e stallo. In condizioni intermedie di incidenza, viceversa, sarebbe risultato possibile raggiungere condizioni di moto più critiche (Figura 16), in conformità con la condizione di incidenza unica per cui si registra il massimo della velocità in ingresso al canale.

Per quanto riguarda l'incidenza, il limite minimo per tutte le configurazioni di solidity è risultato pari a -7.5°; non è stato infatti possibile portare a convergenza le simulazioni testate con incidenze inferiori. Il limite di stallo varia con la solidity, così come riportato in Tabella 4.

Per quanto riguarda il range di solidity analizzato, tutte le analisi effettuate presentano residui, portata massica e rapporto di compressione convergenti; i

σ	incidence range [°]
1.38	-7.5:+8
1.24	-7.5:+6.5
1.10	-7.5:+4.5
0.95	-7.5:+2.5
0.66	-7.5:+0

Tabella 4: *Intervalli di incidenza al variare della solidity*

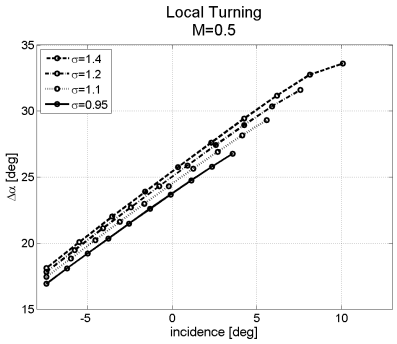

Figura 17: *Deflessione in funzione dell'incidenza per diversi valori di σ*

risultati calcolati per la configurazione di solidity minima, tuttavia, presentano forti incoerenze ed incongruenza sia con i risultati attesi, sia con quelli delle altre configurazioni e verranno pertanto omessi nella presente trattazione.

IV.II Analisi delle prestazioni della schiera

Un'analisi fenomenologica delle condizioni limite è riportata nel dettaglio nel testo completo; si presentano in questa sede i principali risultati relativi alle grandezze di interesse progettuale.

La deflessione (Figura 17) presenta un trend linear con l'incidenza in tutto il range considerato ad eccezione delle condizioni vicine allo stallo per la massima solidity; essa si riduce con la solidity, soprattutto ad elevata incidenza e ad elevati numeri di Mach; La differenza fra valore globale (media sulla sezione) e locale (media a metà altezza di pala) è sempre inferiore al limite misurabile 0.3°.

Le perdite (Figura 18) presentano un andamento pressoché costante in un ampio range di incidenza, la cui ampiezza cresce al ridursi del Mach; questa condizione risulta molto favorevole per garantire una buona regolabilità dello stadio; è presente una condizione di minimo per incidenze leggermente positive. La differenza fra le grandezze locali e globali può essere considerata come un indice dello sviluppo del flussi sugli end-walls: essa risulta ridursi con il numero di Mach e cresce al crescere dell'incidenza, presentando una condizione di massimo appena prima dello stallo. Per quanto riguarda la

dipendenza dalla solidity, è possibile osservare che, al crescere di questo parametro:

- le perdite nella regione di stallo crescono
- l'inicidenza corrispondente alla condizione di minimo si riduce
- in condizioni di choke le perdite sono più influenzate dalla solidity
- l'effetto di solidità cresce con il Mach

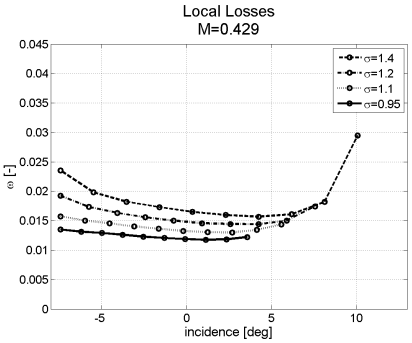

Figura 18: *Perdite in funzione dell'incidenza per diversi valori di σ*

Il diffusion factor (Figura 19) presenta un trend lineare con l'incidenza e con il numero di Mach; è possibile notare che la solidity influenza considerevolmente questo parametro con una dipendenza pari alla quarta potenza del suo inverso.

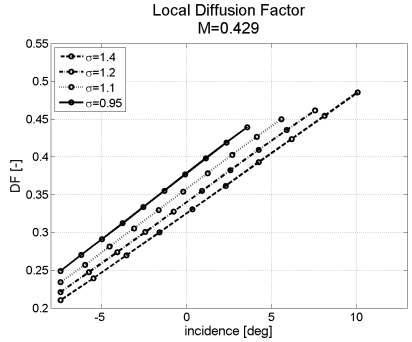

Figura 19: *Diffusion factor in funzione dell'incidenza per diversi valori di σ*

La portata massica presenta un trend lineare con la solidity, coerente con la variazione di passo imposta. L'effetto della solidity aumenta al crescere dell'incidenza; poichè essa rappresenta uno dei fondamentali parametri di progettazione dello stadio la sua dipendenza dalla solidity deve essere attentamente considerata, adottando modifiche considerevoli alla geometria del canale, come ad esempio una riduzione dell'altezza di pala.

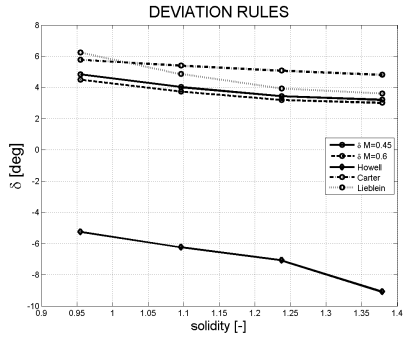

Figura 20: *Correlazioni per l'angolo allo scarico*

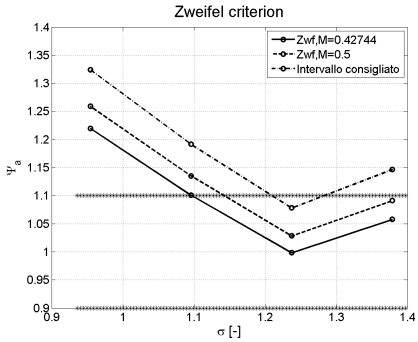

Figura 21: *Coefficiente di Zweifel al variare della solidity*

IV.III Confronto con le correlazioni

In Figura 20 è rappresentato il cofronto con le correlazioni per il calcolo dell'angolo allo scarico della schiera; la prima considerazione è che la deviazione varia al variare del Mach, in particolare si riduce; le prove a basse velocità non permisero agli autori di registrare questa variazione. La correlazione di Howell fornisce una previsione errata di angolo allo scarico, tale che la deviazione risulta negativa. La correlazione di Carter tende a sovrastimare la deviazione in maniera consistente la deviazione (sempre $> 1^\circ$) mentre la correlazione di Lieblein rispecchia molto bene i risultati numerici soprattutto per i valori di solidity più alti.

Per quanto riguarda il coefficiente di Zweifel, i cui valori sono rappresentati in Figura 21, è possibile notare che la maggior parte delle condizioni di funzionamento eccedono i limiti proposti dal criterio, soprattutto considerando i numeri di Mach più elevati per bassi valori di solidity.

Per quanto riguarda il criterio di Carter il coefficiente $C_{L,V_{20}}$, esso risulta sempre inferiore al limite di 1.35 proposto(fig. 22); bisogna tuttavia sottolineare che la scarsa variabilità del parametro rispetto alla solidity sembrerebbe scoraggiarne l'impiego.

In Figura 23 è rappresentato l'andamento dei tre coefficienti di perdite

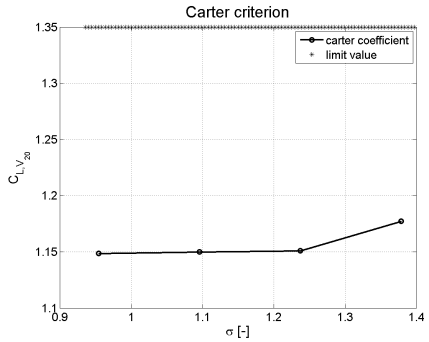

Figura 22: *Coefficiente di Carter al variare della solidity*

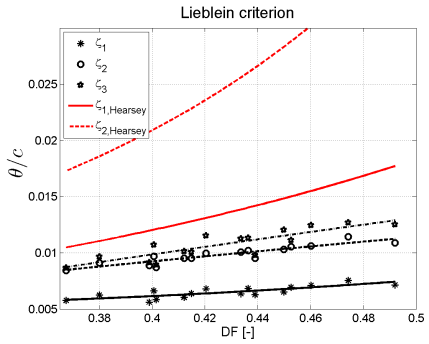

Figura 23: *Correlazioni di Lieblein rispetto al diffusion factor*

definiti in eq. 10, 11 e 12 e delle rispettive correlazioni di Hearsey (eq. 15 e 16). Mentre è possibile individuare una buona corrispondenza con i risultati di Lieblein, le interpolazioni di Hearsey sembrano sovrastimare eccessivamente le perdite; l'espressione esponenziale proposta per ζ_2, inoltre, non risponde all'andamento effettivo calcolato. Il rapporto delle velocità assiali (AVDR) gioca un ruolo importante nel caso in esame, come mostrato dalla differenza fra le curve ζ_2 e ζ_3, soprattutto all'aumentare del diffusion factor.

Per quanto riguarda la dipendenza delle perdite dall'equivalent diffusion ratio, si riporta in Figura 24, a titolo d'esempio, l'andamento di ζ_3 per diversi numeri di Mach; Sebbene il range considerato sia alquanto ridotto, risulta comunque possibile riconoscere il trend dei risultati di Lieblein considerando però le variazioni, non trascurabili, legate agli effetti di comprimibilità.

Si è valutata la possibilità di estendere le correlazioni per valori diversi dell'incidenza ottima; in particolare, per il caso in esame, risulta possibile utilizzare i risultati di Lieblein a partire da valori di incidenza $i > -4.5°$.

IV.IV Confronto fra variazione di corda e di passo

Uno degli obiettivi dell'analisi era lo studio dei differenti effetti generati sul comportamento di due schiere aventi la stessa solidity determinata da una

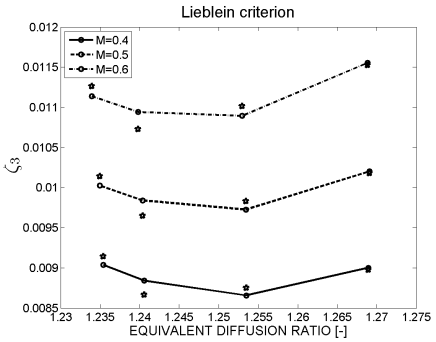

Figura 24: *Correlazioni di Lieblein rispetto al rapporto di diffusione equivalente*

riduzione di corda piuttosto che da un incremento del passo.

Si è verificato che la variazioni del numero di Reynolds, generate dalla variazione di corda, possono essere trascurate; è possibile tuttavia registrare alcune differenze fra le prestazioni registrate fra le diverse configurazioni, tuttavia bisogna sottolineare che esse sono generalmente inferiori al minimo valore misurabile sperimentalmente. La spiegazione di queste perdite risiede dunque nelle differenze presenti nella mesh: nelle configurazioni a corda ridotta, infatti, è stata ridotta anche la distanza fra la sezione di ingresso e di uscita dai bordi della pala e conseguente le perdite legato allo sviluppo di strato limite sugli end-walls sono meno accentuate.

IV.V Confronto fra diversi modelli di turbolenza

L'analisi è stata effettuata, oltre che con il modello SST già presentato, utilizzando i modelli di turbolenza BL, YS.

La prima differenza riguarda l'estensione del range di incidenza investigabile: con il modello $\kappa - \varepsilon$ e BL è stato infatti possibile portare a convergenza le simulazioni effettuate fino ad un'incidenza negativa pari $i = -13.5°$. Anche il limite di stallo risulta più esteso utilizzando questi due modelli, anche se le differenze sono meno marcate rispetto al ramo negativo e, ad eccezione della configurazione con solidity più elevata, non eccedono il grado.

Per quanto riguarda la differenza in termini di prestazioni, bisogna sottolineare che le previsioni di deflessione e diffusion factor a metà altezza del canale non variano consistentemente se non agli estremi del range di incidenza analizzati, dove le differenze sono apprezzabili. Per quanto riguarda le perdite le differenze sono generalmente maggiori in tutto il range di incidenza; YS fornisce le previsioni più elevate mentre gli altri due modelli forniscono valori molto simili. La variazione di solidity non sembra modificare il comportamento dei modelli: le differenze presenti fra i risultati, infatti, rimangono generalmente costanti al variare di questo parametro.

Una descrizione fenomenologica ha permesso di spiegare le differenze presenti fra i diversi modelli nelle condizioni di choke e stallo. In generale è possibile affermare che i modelli a due equazioni forniscono sempre una

topologia del flusso similare, sebbene gli stessi fenomeni descritti siano caratterizzati da diverse intensità; il modello di Baldwin Lomax fornisce risultati che si discostano, talvolta in modo consistente, dagli altri modelli, in particolare nella presenza, localizzazione ed estensione degli urti e delle scie. In particolare in condizioni di stallo, il comportamento del flusso descritto da questo modello non sembra affidabile, sebbene residui, flusso di massa e rapporto di compressione convergano perfettamente. Per quanto riguarda i modelli a due equazioni, risulta complesso esprimere un giudizio di merito; sebbene il modello SST appaia più sensibile alle variazioni di comportamento del flusso e alle condizioni imposte, soltanto attraverso le prove sperimentali sarà possibile individuare il modello più adeguato per la corrente analisi.

V. Conclusioni e sviluppi futuri

Attraverso uno studio numerico è stato analizzato l'effetto della solidity sulle prestazioni e sulla stabilità di una schiera piana di compressore assiale costituita da profili progettati da TechspaceAero in regime di comprimibilità. Il confronto con i risultati di letteratura ha permesso di evidenziare un comportamento conforme agli studi precedentemente effettuati e di mettere in luce le variazioni legate all'incremento delle velocità in ingresso alla schiera.

Lo sviluppo del presente lavoro si articolerà in tre fondamentali direzioni:

- il modello numerico verrà ampliato attraverso il confronto con i risultati del modello di turbolenza di Spallart-Almaras e con l'utilizzo di diverse tipologie di profili(Double circular arc (DCA), Multi-circular arc (MCA))
- i risultati saranno validati attraverso una campagna sperimentale presso la galleria del vento C3 del Von Karman Institute for Fluid Dynamics
- le correlazioni ricavate verranno formalizzate e integrate in strumenti di progettazione attualmente in fase di sviluppo presso il Von Karman Institute for Fluid Dynamics (VKI) e TSA.

References

[1] J. Sans. The effect of solidity on compressor performance and stability. Technical report, Von Karman Institute for Fluid Dynamics, 2011.

[2] Sir C.A. Parsons. Turbo-compressor and pump. 710,884, October 1902.

[3] R.J. Robbins, W.H.and Jackson and S. Lieblein. *Aerodynamic design of axial-flow compressor*, 1965. NASA SP-36.

[4] T. Obrecht. Hp compressor preliminary design. In *Advances in axial compressor aerodynamics*. 2006.

[5] S.L. Dixon. *Fluid Mechanics, Thermodynamics of Turbomachinery*. Butterworth-Heinemann, 1998.

[6] S. Lieblein, Schwenk F.C., and R.L. Broderick. Diffusion factor for estimating losses and limiting blade loadings in axial-flow-compressor blade

elements. Research Memorandum E53D01, NACA, Cleveland, Ohio, June 1953.

[7] S. Lieblein. Loss and stall analysis of compressor cascades. *Journal of Basic Engineering*, 81(4):387–400, July 1959.

[8] C. C. Koch and L. H. Jr. Smith. Loss sources and magnitudes of axial compressors. *Journal of engineering for power*, 98:411–424, 1976.

[9] P.I. Wright and D.C. Miller. An improved compressor performance prediction model. In *Turbomachinery : Latest developments in a changing scene*, pages 69–82. Bury St Edmunds, UK, Mechanical Engineering Publications Ltd, 1991.

[10] W. Heilmann, H. Starken, and H. Weyer. Cascade wind tunnel tests on blades designed for transonic and supersonic compressors. In *AGARD Conference Proceeding*, volume 34.

[11] A.B. McKenzie. The selection of fan blade geometry for optimum efficiency. In *Proceedings of institution of mechanical engineering*, 1988.

[12] A.B. McKenzie. The design of axial compressor blading based on tests of a low speed compressor. In *Proceedings of institution of mechanical engineering*, 1980.

[13] R.M. Hearsey. Practical compressor aerodynamic design. In *Advanced topics in turbomachinery design*. 1986.

[14] G.L. Liu. Simple formulae for optimal solidity of two-dimensional compressor cascades based on diffusion concept. *International Journal of Turbo and Jet engines*, 1993.

Contents

List of Figures

List of Tables

Abstract

The challenges issued to engine designers by the standard on pollutant and noise emissions, together with performance maximisation require the development of new architectures and concept as well as the consolidation and optimization of engineering tools and correlations regarding the main design parameters. In a axial flow compressor, the solidity represents the ratio of the aerodynamic chord over the pitch and it is related, then, to the blade number and to engine weight. This study, developed in the framework of a collaboration between the Von Karman Institute for Fluid Dynamics and the private company TechspaceAero, investigates the solidity effect on performance and stability of a high speed linear cascade. The main compressor correlations are considered to determine the influence of solidity on deviation, incidence and losses, together with the issue represented by the optimum condition determination. A CFD approach is then proposed to investigate the effect of solidity through the software FINE/Turbo by NUMECA International. The mesh and the turbulence model effects are studied to setup the model. The behaviour of eight different configurations of pitch and chord is tested, allowing to assess five different solidity values and compare the effect of a decrease in chord rather than an increase in pitch. The incidence is varied from choke to stall, within an inlet Mach number range between 0.4 and 0.8. The analysis is performed with three different turbulence models, considering two different boundary condition types. As the follow up of the present work will be the experimental campaign, this study is also intended to highlight the most critical aspects of the future tests.

Chapter 1

Introduction

Since the publications about the goals of the Advisory Council for Aviation Research and Innovation in Europe (ACARE), many efforts have been put by many companies and institutions, to fulfil new requirements in terms of pollutant and acoustic emissions and fuel consumption of aero-engines. The development of new engine architectures and concepts has become an essential activity moving through many different paths and directions:

1. Development and optimization of new types of engines
2. Investigation on technologies to reduce vibrations, to design compact mid-frame structures and highly efficient low pressure turbines
3. Demonstration of the suitability of alternative fuels for aircraft engines

As far as concern the new architectures, the Counter-Rotating Turbofan, the Geared Turbofan and Direct Drive Open Rotor (DDOR) engine (Figure 1.1) can be cited. The foundations of the present work lay in the results of the last item,

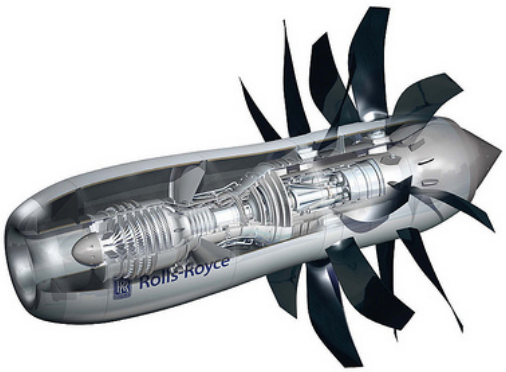

Figure 1.1: Direct Drive Open Rotor

the Validation of Radical Engine Architecture systems (DREAM) project. In the past years the Von Karman Institute for Fluid Dynamics (VKI) was in charge of the numerical and experimental assessment of the low pressure (LP) section of the DDOR, whose aerodynamic design was carried out by the private Belgian company TechSpace Aero . As a follow-on of the good work performed, the partnership has continued with the development of a new project, focusing on the effect of solidity on compressor performance and stability. The research plan is presented at the end of this chapter, after a short presentation of the two organizations involved.

1.1 The organisations involved in the project

1.1.1 The Von Karman Institute for Fluid Dynamics

In the course of 1955, Professor Theodore von Karman proposed the establishment of an institution devoted to training and research in aerodynamics which would be open to young engineers and scientists of the NATO nations. It was strongly felt that this form of international undertaking would fulfil the important objective of fostering fruitful exchanges and understanding between the participating nations in a well-defined technical field.

The von Karman Institute was established in October 1956 in the buildings which previously hosted the aeronautical laboratory of the Civil Aviation Authority of the Belgian Ministry of Communications. The VKI hosts three departments (aeronautics and aerospace, environmental and applied fluid dynamics, and turbomachinery and propulsion). It provides post-graduate education in fluid dynamics (a research master in fluid dynamics, doctoral programs, stagiaire programs and lecture series) and encourages "training in research through research". The institute undertakes and promotes research in the field of fluid dynamics. It possesses about fifty different wind tunnels, turbomachinery and other specialized test facilities, some of which are unique or the largest in the world. Extensive research on experimental, computational and theoretical aspects of gas and liquid flows is carried out at the VKI under the direction of the faculty and research engineers, sponsored mainly by governmental and international agencies as well as industries.

The present work was developed during an internship at the Turbomachinery and Propulsion department, specialized in the aero-thermal aspects of turbomachinery components for aero-engines and industrial gas turbines, space propulsion units, steam turbines and process industry compressors and pumps. It has accumulated wide skills in high speed wind tunnel testing and related measurement techniques, developments and applications. The department has acquired a world recognised expertise on steady/unsteady aerodynamic and aero/thermal aspects of high pressure, including cooling, and low pressure turbomachinery components through the design, development and use of a number of unique wind tunnels. On the computational side, the department has over 20 years of

Figure 1.2: The VKI laboratories, in Rhode Saint Genese, Belgium

experience in the analysis of flow in turbomachines, and in the design techniques and multi-disciplinary optimization methods or their components.

1.1.2 TechSpace Aero

Safran is a leading international high-technology group with three core businesses: aerospace, defence and security; as part of this group, TechSpace Aero designs, develops and manufactures modules, equipment and test facilities for aerospace engines. Located near Liège in Belgium, TechSpace Aero employs 1,200 people and has two American subsidiaries: Cenco Inc (Minnesota) and ACI (Florida). As far as concerns the propulsion area, the company is recognised worldwide as an expert in the design, development, production and assembly of low pressure compressors and front bearing supports for turbo-reactors. Through partnership agreements with Snecma, General Electric and Pratt Whitney, the company designs and manufactures low pressure compressors and front bearing supports for the majority of commercial engines across all thrust ranges. TechSpace Aero 's role is to be a technological specialist making an important contribution to assist engine manufacturers in developing new engine architecture. In the past 10 years 6 new low pressure compressors were developed and the 15% of the company's turnover is invested in preparing for the future and for overcoming the environmental challenges facing the aviation industry, while striving to minimise the cost of engines and equipment.

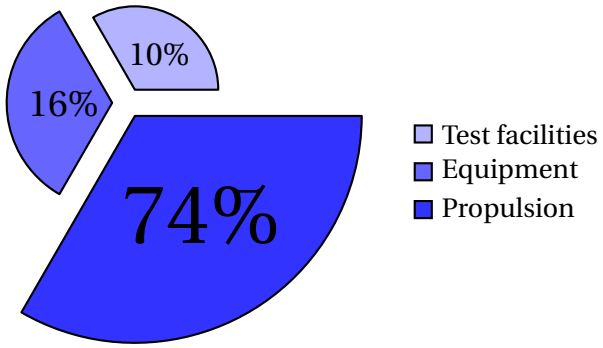

Figure 1.3: TechSpace Aero turnover

1.2 The solidity in axial flow compressor design

The preliminary design process of an axial flow compressor, according to Obrecht (ref. [1]), is represented in Figure 1.4. This phase leads to the ultimate definition of the main geometrical and aerodynamic characteristics, which should not be changed during the remaining parts of the process. Since the very beginning, three main issues must be taken into account: the aerodynamic performance, the weight and the cost of the system; the solidity, namely the ratio of the airfoil chord to the peripheral spacing between two adjacent blades of the cascade, appears to be deeply involved in each of these aspects, making its choice a crucial issue for the designer.

The very first step, the thermodynamic cycle definition, makes the designer translate the customer requirements into constraints: the thrust specification determines the pressure ratio, while the fuel consumption constraint requires a definite level of efficiency and weight; the acceleration time and operability concerns are addressed by the stall margin specification and the weight of the compressor is mainly a consequence of the number of stages and compressor overall size; in the end the maintenance costs and the mean time between overhaul are strongly dependent on the number of parts and thus on the number of stages and blades. Considering the following definition of solidity, explicitly expressed in function of the number of blades, it could be understood how much this parameter has a central role when linked to all the aspects mentioned above:

$$\sigma = \frac{c \cdot Z}{2\pi r} \tag{1.1}$$

As a matter of fact, one can directly see the connection of to the number of blade Z, implying consequences on the weight of the engine-and then on its global efficiency- and on manufacturing and maintenance costs; at the same time, the proportionality to the chord over the radius can drop a hint on the influence on the engine dimensions, as the axial extent of a compressor depends on the

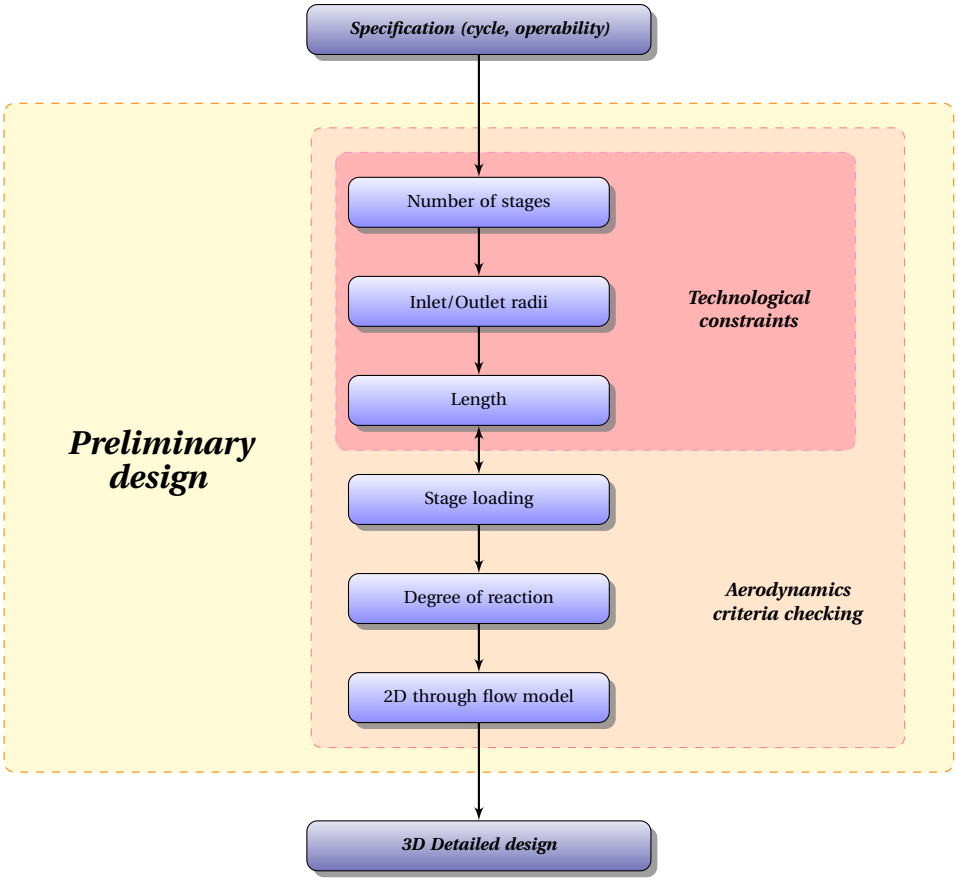

Figure 1.4: Axial Compressor preliminary design process

spacing between two different rows and on the axial chord of each single row, defined as follows:

$$c_{ax} = c \cdot \cos\gamma \tag{1.2}$$

where γ is the angle between the chord and the axial direction, named "stagger". The aerodynamic effects can be summarized as follows:

Flow turning

Considering the stagger fixed, it is possible to see that the turning effectiveness of the row strongly depends on the driving capability of the vane, determined by its blade to blade aspect ratio and then by the solidity. It can be clearly inferred that an increase in the number of blade, keeping the same chord and radius, leads to smaller passage sections and then allows to achieve a higher stream deflection through proper blade profiles.

Blade loading and losses

The inlet and outlet angles of the flux are assigned according to a single-dimensional analysis based on the performance required and the rotation speed limit and it could be said that the same deflection of the flux can be obtained with different configurations of the row particularly regarding the solidity. In theory, however, an optimum value for solidity can be found, laying between two opposite conditions:

- *high solidity*: this situation corresponds to a low blade load and then to a smooth pressure profile along the airfoil, leading to a low friction coefficient and low pressure losses per area unit. However the lapped surface is more extensive and the losses are high.
- *low solidity*: the blade loading is high and the pressure gradient is rough and characterized by high diffusion and then high friction coefficient and consequent high losses.

Unfortunately the minimum loss condition usually corresponds at very low solidity value(Figure 1.5) and really close to flow separation.

Stability

As blade loading increases, stall condition can be easily reached.

Due to the importance of this parameter, many efforts have been put, mostly in the past, to understand the solidity effect on compressor performances and the first part of this work (Chapter 2) is aimed to review the main literature references. The works on this subject can be divided into two different groups, in terms of different type of analysis performed. The early works published from 1945 to 1955 consisted mainly in theoretical studies analysis and two-dimensional low-speed experimental campaigns. Howell, Carter, Zweifel, Lieblein laid strong foundations for all the future researches. In the following years till the late seventies, many experiments were conducted to investigate the phenomenon though

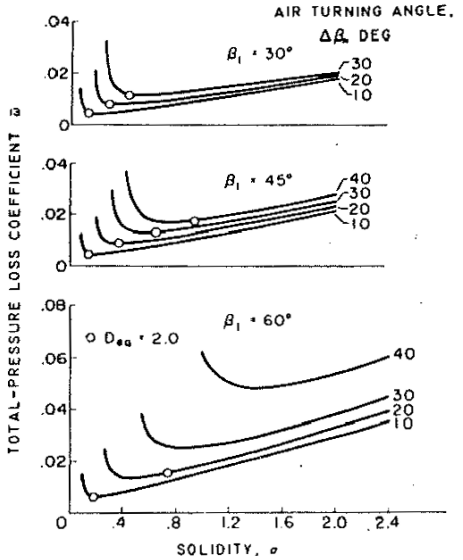

Figure 1.5: Loss coefficient versus solidity

three-dimensional analysis. However, despite the extended amount of time and resources spent in these projects, no general rule has been published for choosing optimum solidity neither in terms of loading nor efficiency. As a matter of fact the solidity choice appears to be based on the experience of the designer and on the common practice of each company, as a result of a trade-off between weigth, blade loading and efficiency requirements.

In the past decades, to fulfil the requirements in terms of stages loading both the solidity and aspect ratio, namely the blade height over the chord, have been increased, as presented in Figure 1.6. These design trends are mostly due to a better behaviour of long-chord airfoil but, as consequence of the effects mentioned before, it is clear that an inversion of these tendencies can really improve the efficiency of the engines allowing to accomplish the new constraints in terms of fuel consumption and pollutant emissions, and would also likely lead to cut the manufacturing costs.

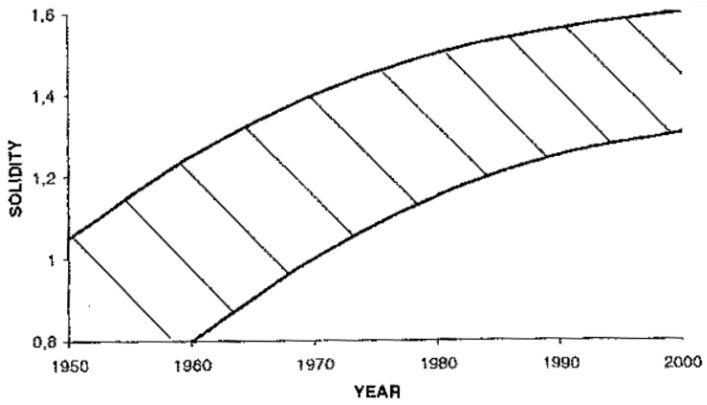

Figure 1.6: Historical design values for solidity and aspect ratio

1.3 Objectives of the present work

In the framework of the collaboration between VKI and TechSpace Aero on the DREAM booster, both a numerical and experimental analysis on the solidity effect have been conducted on the first stage, comprehensive of the Inlet guide vane (IGV) row. The results are partially presented in [2] and show that good performances can be easily achieved decreasing the solidity of the stator,as shown in Figure 1.7. As far as concerns the rotor performances, the results cannot still be used for general conclusions, as the decrease in the number of blade causes also a reduction in the incidence range (Figure 1.8). As this kind of analysis was performed *a posteriori*, they can underestimate the performances and could be taken into account just for a preliminary assessment. A different choice in the number of blades involves different physical and structural issues that usually leads to radical change in the design path. However an objective has been set for the design of the new booster: a 15% reduction in the solidity of the stator. To validate this choice and to evaluate its feasibility and consequences, an extended research is conducted. The main investigation will be performed through an experimental analysis on a linear compressor cascade in the VKI C-3 facility; to set up the test and foresee the possible issues, a numerical simulation of the experiment is required. The subject of the present work is the assessment of the steady performance from choke to stall in cruise conditions through the Numeca International solver for computational fluid dynamics (CFD). The global performance is examined for 8 different configurations, varying separately the pitch and the aerodynamic chord, as reported in Table1.1. Because of the main objective of the investigation, an important focus of this project is to analyse the obstacles which will possibly appear during the tests and to highlight that improvements can be achieved in order to decrease measurement uncertainties and their influence on efficiency calculation.

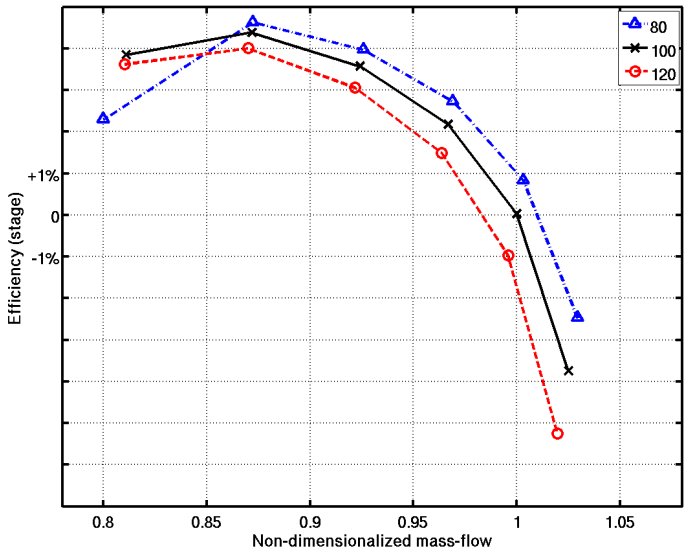

Figure 1.7: Stator efficiency of DDOR booster for different number of blades

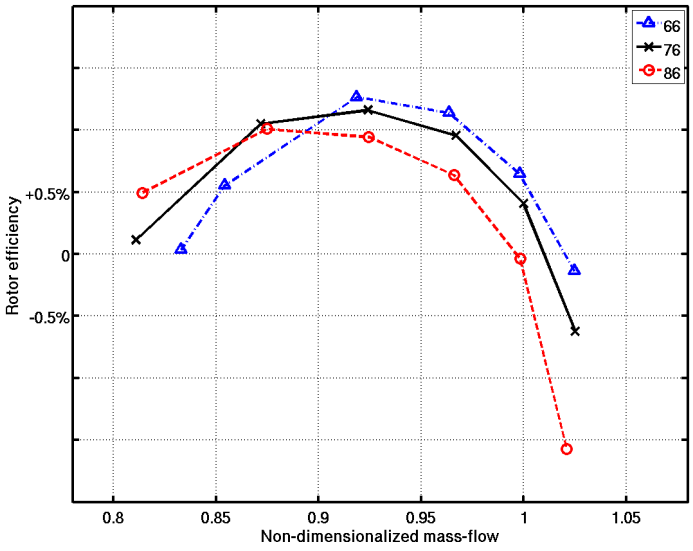

Figure 1.8: Rotor efficiency of DDOR booster for different number of blades

SOLIDITY VALUES			**PITCH** (mm)			
			24	26.74	30.2	34.67
			100%	*89.7%*	*79.5%*	*69.2%*
CHORD (mm)	33.09	*100%*	**1.38**	**1.24**	**1.1**	**0.95**
	29.7	*89.7%*	**1.24**	*1.11*	*0.98*	*0.86*
	26.3	*79.5%*	**1.1**	*0.98*	*0.87*	*0.76*
	22.91	*69.2%*	**0.95**	*0.86*	*0.76*	**0.66**

Table 1.1: Investigated solidity values

Chapter 2

Literature survey

Sir Charles Parsons, in one of the first patents on axial flow compressor (ref. [3]), states: *"My invention consists in a compressor or pump of the turbine type, operating by the motion of sets of movable blades or vanes between sets of fixed blades, the movable blades being* ***more widely spaced*** *than in my steam turbines and constructed with curved surfaces on the delivery side, and set at a suitable angle to the axis of rotation."*. These few lines bear witness that the problem of solidity, or at least the problem of the determination of the blade spacing, was clearly identified as a very import issue since the beginning of turbomachinery modern history. The cited patent was published in 1902 and represents just a first hint to a problem that has been faced, studied and analysed by thousands of engineers and scientists in the last and present century.

After a brief introduction on the different approaches followed by the researchers and a short review of the notation, this chapter presents the main literary background of this study. The review of some of the most relevant theories and studies about the importance of solidity is here divided in three parts, firstly considering the two-dimensional investigations (sec. 2.3), which led to the definition of some correlations between the blade incidence and deviation, as well as the blade loading; in the second part , the three-dimensional studies (sec. 2.4) will be considered, to have a reference to understand how the results from the present analysis will impact the real compressor row. Eventually the optimum solidity correlations (sec. 2.5) will be presented, for better understanding the results.

2.1 Introduction

In the design and optimization of axial compressor and turbomachines in general, six different sources can be used to get blade information data:

1. theoretical (potential-flow) solutions of the flow past airfoil cascades

2. two-dimensional cascade experiments

3. three-dimensional annular-cascade experiments
4. two-dimensional cascade numerical computations
5. three-dimensional annular-cascade numerical computations
6. genetic algorithms

As known, the behaviour of the flow in an axial compressor is mainly characterized by three dimensional effects; however the main behaviour of the fluid and the machine itself could be really well predicted through accurate two-dimensional investigations, which are usually less expensive, less difficult to set up and can give more reliable and general results; for this reason, various methods have been developed to avoid the characterization of the three dimensional flow, through many different simplified approaches and models. Many efforts have been put into the study of a theoretical solution of the cascade flow, but the limitations involved in this kind of calculation don't permit them to be adopted for design purpose. It must be said that the last three items of the previous list should be considered as recent improvements in the study of turbomachinery while the knowledge-base on compressor behaviour was developed almost entirely on experimental analysis. As a matter of fact, since the postwar years, many systematic and extended tests have been performed and presented by the scientist of both European and north-American institutions.

2.2 Cascade notation and definitions

In Figure 2.1 and in Table 2.1 the geometrical definition and the nomenclature used in the present work are presented. This notation system was defined by National Advisory Committee for Aeronautics (NACA) and is fully presented in [4]. In agreement with the Anglo-Saxon convention, the angles are referred to the axial direction.

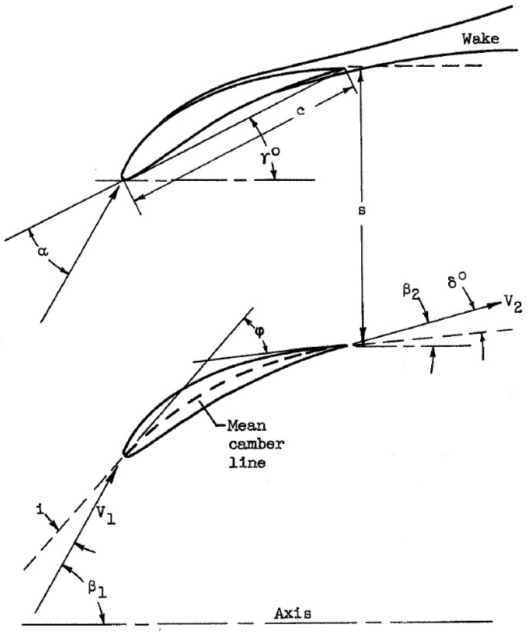

Figure 2.1: geometrical definition of a cascade

Symbol	Quantity
α_1	absolute inlet flow angle
α_2	absolute outlet flow angle
β_1	relative inlet flow angle
β_2	relative outlet flow angle
κ_1	inlet blade metal angle
κ_2	outlet blade metal angle
ϕ	camber angle
i	incidence angle
δ	deviation angle
γ	stagger angle
c	aerodynamic chord
s	pitch

Table 2.1: Nomenclature of a cascade

2.3 Two-dimensional investigation

The early studies about the influence of solidity were conducted in two-dimensional facilities, as part of more extensive works focusing on the behaviour of the flow within an axial flow machine in general. These works consist almost always in a first characterisation of the flow angles, and then on the calculation of the blade loading and losses, relating the different results to some parameters which seem to be of some influence by the author.

As far as concerns the prevision models of losses will be hereby considered the works by Lieblein, Koch and Smith (General Electric) [5] and by Wright and Miller (Rolls Royce) [6], dated 1976 and 1991.

Some efforts are dedicated to understand the effects of axial velocity density ratio, compressibility and viscosity, as they appear to be of primary importance for the behaviour of the cascade.

2.3.1 Incidence and deviation correlations

Howell

The first scientific investigation was published by Howell, as a result of a great experimental and theoretical works firstly set up by Constant and Griffith during the second world war. The analysis, reported in his book *The present basis of axial flow compressor design* in 1942 and later summarized in his article [7] (here used as reference) represents the basis for almost all the future works.

As far as concerns the reference conditions, Howell used a nominal deflection ϵ^*, corresponding to the 80% of the stalling low speed deflection (maximum deflection); this last condition is taken to occur when the blade loss is twice its minimum value. However, even if the author's data seems to be very useful for the preliminary evaluation of cascade performances, they are not really convenient from a designer point of view, as no indication for the choice of optimum incidence and camber are presented, left to be chosen by the "inspiration" of the engineer. Howell stated for the first time that the tangential deflection depends only on solidity, for a high range of outlet conditions, as represented by the following equation and visualized in Figure 2.2:

$$\tan(\beta_1) - \tan(\beta_2) = \frac{1.55}{1 + \frac{1.5}{\sigma}} \tag{2.1}$$

Howell also presents the deviation rule by Constant, to calculate the optimum deflection, based on solidity, camber θ and a coefficient m dependent on the camber angle, on the position of his maximum and on the ideal outlet flow angle α_2^*:

$$\delta = m\phi\sqrt{\frac{1}{\sigma}} \tag{2.2}$$

This rule permits to understand easily the role of solidity in determining the behaviour of a cascade in terms of turning: as an increase of solidity implies a

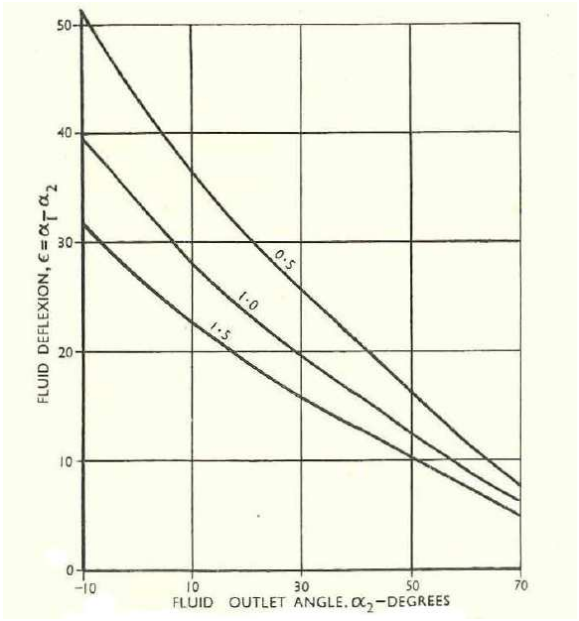

Figure 2.2: Nominal deflection versus outlet flow angle

different shape of the channel, longer and smaller, the effectiveness in turning the fluid increases itself, because the airfoils can better drive the stream; for a rotor this means an increase of the pressure ratio, as the total pressure rise mainly depends on the turning. However this rule doesn't contain any information about the airfoil shape and it cannot be used "standalone" to define the geometry of the cascade, but must be coupled with a blade loading criterion.

Carter

Few years later Carter developed the work by Howell, proposed his own deviation and blade loading rules, in [8], which are more effective for design purpose than the correlations from his predecessor.

Carter based is approach on different definitions of the reference conditions: he defined the optimum conditions for incidence and deflection, dependent on the maximum Lift to Drug ratio. The physical effect mainly determining this ratio is the position of the forward stagnation point and, as it depends strongly on camber and pitch, the solidity has an important role in it. He developed the rule 2.2 and managed to extend it introducing a coefficient n equal to one for turbines cascades:

$$\delta = m\phi\left(\frac{1}{\sigma}\right)^n \tag{2.3}$$

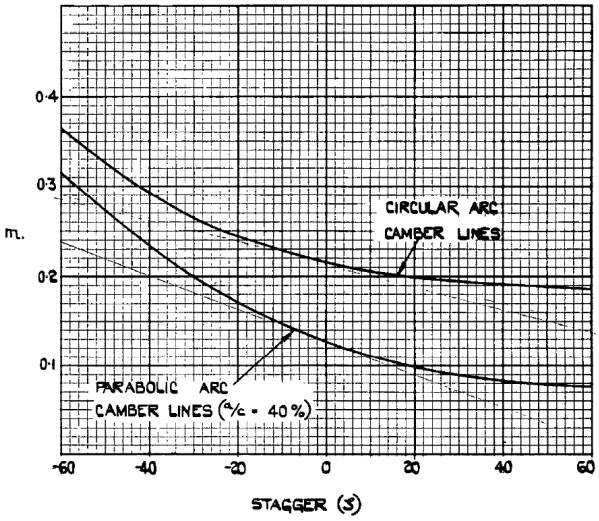

Figure 2.3: Carter rule: value for coefficient m

Lieblein

The work from the members of Compressor and Turbine Research Division (CTRD) developed in the Lewis flight propulsion laboratory of the National Advisory Committee for Aeronautics (NACA) is reported in the three volumes *Aerodynamic design of axial flow compressor* and represents a milestone for the development of the modern design technique of compressors, as it is based on strong theoretical and experimental analysis. As far as concerns this paragraph, the reference used is the article reported in [4]. In the 50s, many tests were firstly conducted on NACA 65 airfoil series at low speed, using a boundary layer removal system. These results were extended to other different kind of airfoils as, for instance, Double circular arc (DCA), Multiple circular arc, and circular mean camber line, also for high speed flow conditions.

As the mean camber definition is a mathematical impossibility, an equivalent camber must be defined, referred to the C_L parameter, which is the conventional definition for the mean line geometry of the series of airfoils:

$$\phi_e = 25\, C_L \tag{2.4}$$

The reference condition used in this work is quite different from the one used by Howell and Carter, being based on the mean incidence between left and right stall conditions, taken to occur when the loss is twice of its minimum value.

For linear incompressible cascade, the definitions of the reference incidence and consequent deviation are based on the inlet flow angle and the main geometrical feature of the airfoil: the mean line deflection, the maximum thickness and the solidity.

$$i = i_0 + n\phi \tag{2.5}$$

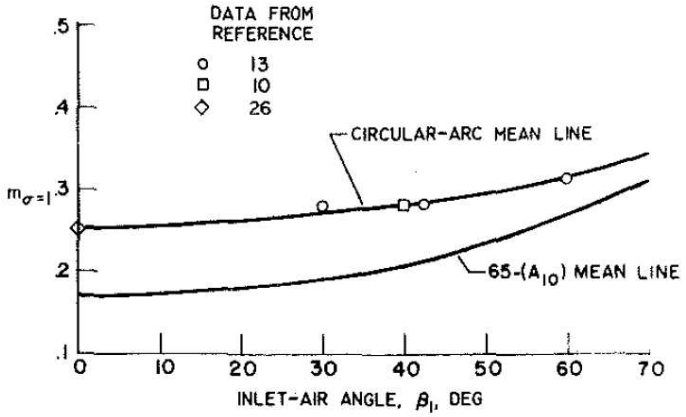

Figure 2.4: Lieblein correlation for incidence and deviation: coefficient m for different profile shapes in function of inlet flow angle for unitary solidity

$$\delta = \delta_0 + \frac{m}{\sigma^b}\phi \tag{2.6}$$

The terms i_0 and δ_0 represent respectively the incidence and the deviation in reference conditions for symmetric profiles and they can be defined from the values $(i_0)_{10}$ and $(\delta_0)_{10}$ for 10% maximum profile thickness through two different kinds of shape factors, depending on the maximum thickness and the profile shape:

$$i_0 = (K_i)_{sh}\,(K_i)_t\,(i_0)_{10} \tag{2.7}$$

$$\delta_0 = (K_\delta)_{sh}\,(K_\delta)_t\,(\delta_0)_{10} \tag{2.8}$$

The coefficient m,n and b are provided in plots in function of inlet flow angle and solidity; some examples are reported in Figure 2.4,2.5 and 2.6.

From the linear relation between ϕ and both the incidence and deviation, descends an important equations to express the cinematic deflection $\varepsilon = \phi + i - \delta$:

$$\phi = \frac{\varepsilon - i_0 + \delta_0}{1 - \frac{m}{\sigma^b} + n} \tag{2.9}$$

As all the right hand terms depend just on the solidity and on the inlet an outlet flow angles, it is possible to determine the camber, given the velocity triangles and then the incidence.

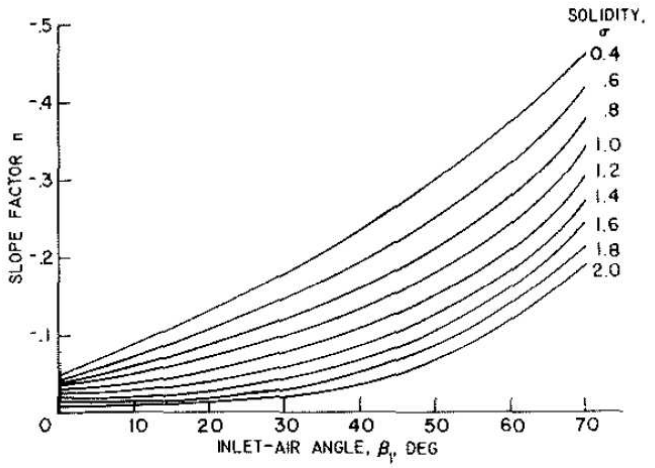

Figure 2.5: Lieblein correlation for incidence and deviation: coefficient n in function of inlet flow angle for different solidity values

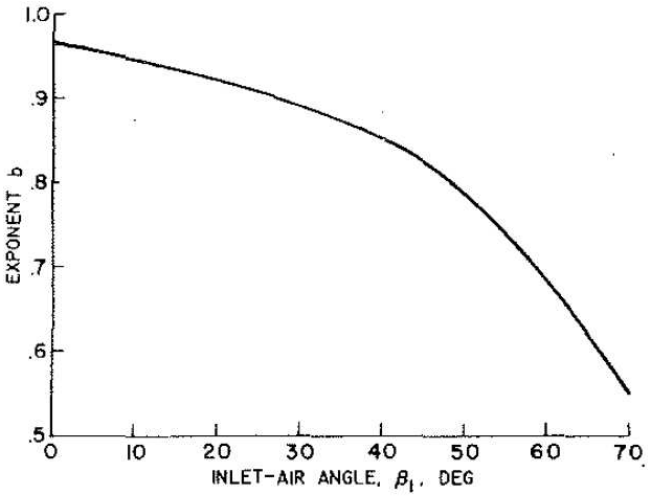

Figure 2.6: Lieblein correlation for incidence and deviation: coefficient b in function of inlet flow angle

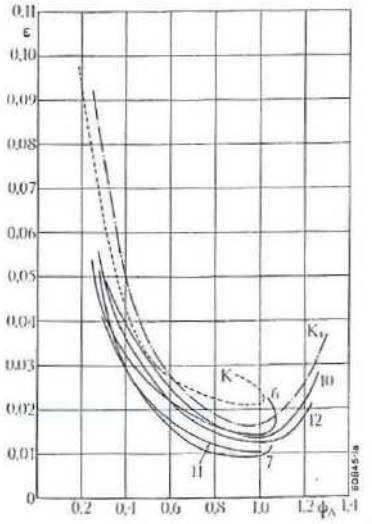

Figure 2.7: Drag-lift ratio in function of the Zweifel coefficient Ψ_a for different types of blading

2.3.2 Blade loading criteria

Zweifel

In 1945 Zweifel published his study (ref. [9]) on turbine blade spacing; after a short review of the most common loading criteria used in his days, based on the definition of different lift coefficients, very suitable for wing profile, but not really convenient for turbomachinery applications, the author defines his own method, consisting in the limitation of an adimensional coefficient Ψ_a based on the lift; due to the good results obtained with this method, many authors have been using it for compressors as well.

$$\Psi_a = \frac{\text{Lift}}{\text{Lift}_{ref}} = \frac{\Delta V_\theta \left(V_1 + V_2\right)}{\sigma v_2^2} \tag{2.10}$$

The results of different cascade tests, shown in Figure 2.7, enlighten an independence of the drag-lift ratio from the inlet and outlet flow angles, presenting also an optimum condition. The value of this coefficient always lays between 0.9 and 1. Considering the flow as incompressible, it is easy then to express the Zweifel coefficient relation with the angles and the solidity:

$$\Psi_a = \frac{\left(\cos\left(\beta_1\right) + \cos\left(\beta_2\right)\right)\left(\tan\left(\beta_1\right) - \tan\left(\beta_2\right)\right)}{\sigma \cos^2\left(\beta_2\right)} \tag{2.11}$$

Chosen a value for Ψ_a and given the velocity triangles, it is possible to compute the optimum pitch to operate at maximum lift-to-drag ratio. Many authors

(Dixon [10], Eck, Wallis) refer to this criterion for fan design and Obrecth ([1]) presents it as a possible method to compute optimum pitch for high pressure compressors stages. Nonetheless the experimentation is based mostly on turbine rows and this criterion, even if it is good for a preliminary evaluation, can not be completely trusted for the final design.

Carter

Carter follows an approach similar to the one by Zweifel, defining a lift coefficient for the single blade from a theoretical outlet velocity V_{20} in a null trailing edge thickness hypothesis. According to Carter, it is necessary to limit this coefficient to a specific value of 1.35.

$$c_{L,V_{20}} \leq 1.35 \tag{2.12}$$

Defining the effective pitch $s' = s - t_1$ and the approximate thickness of the trailing edge in the direction of the pitch as $t_t = \frac{t_n}{\cos(\alpha_\infty)}$ it is possible to express the following velocities ratio:

$$\frac{V_2}{V_{20}} = \frac{s}{s'} \tag{2.13}$$

$$\frac{V_\infty}{V_2} = \frac{\cos(\alpha_2)}{\cos(\alpha_\infty)} \tag{2.14}$$

Then it is possible to refer the coefficient $c_{L,V_{20}}$ to the definition of c_{L,V_∞} and then, for a frictionless blade, to the angles:

$$c_{L,V_{20}} = \left(\frac{V_2}{V_{20}}\right)^2 \left(\frac{V_\infty}{V_2}\right)^2 c_{L,V_\infty} = 2\frac{1}{\sigma}\left(\frac{s}{s'}\right)^2 (\tan\alpha_1 - \tan\alpha_2)\frac{\cos^2\alpha_2}{\cos\alpha_\infty} \tag{2.15}$$

From the previous relation it is then possible to compute the solidity.

Lieblein

The greatest enhancement in the study of blade loading and stability limit of cascades comes from Lieblein and his definition of the Diffusion Factor (ref. [11], 1953). The authors start from a point of view which is quite different from their predecessors, grounding the roots of their work in the boundary layer theory. Studies in this branch of the fluid dynamic, make the point that the friction coefficient and the different adimensional parameters defining the dissipation (momentum thickness, displacement thickness, etc ...) depend on the velocity gradient on the blade, particularly in the diffusion areas. Assuming the gradient roughly measurable as the difference between the maximum velocity on the blade and the outlet velocity, the local diffusion factor D_{loc} is defined, strongly experimentally related to the momentum thickness on the blade (see Figure 2.8), which is a good index for the losses.

$$D_{loc} = \frac{V_{\max} - V_2}{V_{\max}} \tag{2.16}$$

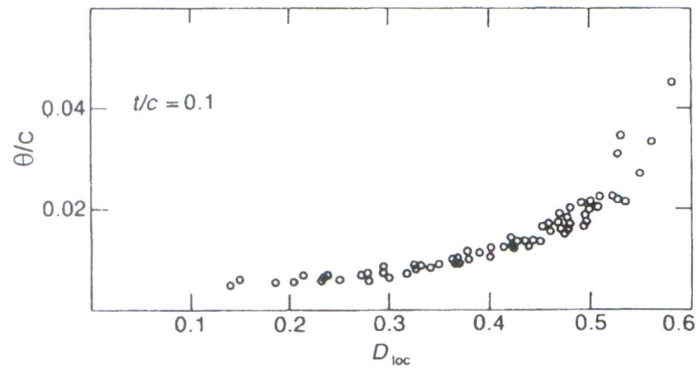

Figure 2.8: Momentum thickness in function of local diffusion factor

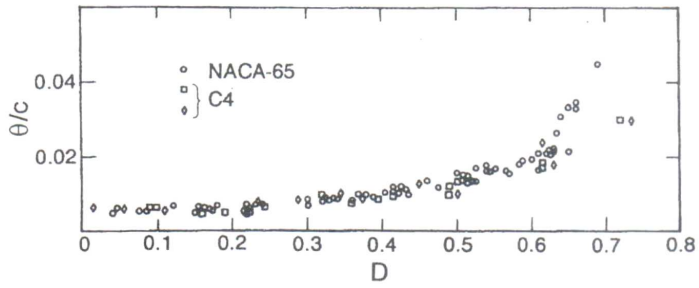

Figure 2.9: Momentum thickness in function of global diffusion factor for different aerofoils

Unfortunately the maximum velocity on the blade is not usually known or easily available; the definition of a different parameter based on the main stage design is then necessary. Lieblein suggested the adoption of a global diffusion factor, defined as follows:

$$D = \left(\frac{V_1 - V_2}{V_1}\right) + \left(\frac{V_{1t} - V_{2t}}{2\sigma V_1}\right) \tag{2.17}$$

It is also possible to express the parameter just in function of the angles:

$$D = \left(1 - \frac{\cos\alpha_1}{\cos\alpha_2}\right) + \frac{\cos\alpha_1}{2\sigma}(\tan\alpha_1 - \alpha_2) \tag{2.18}$$

The global diffusion factor is determined by two contributes: the first addendum represents the diffusion between inlet and outlet, while the second term depends on the blade loading, expressed as a momentum difference in tangential direction; the relation with solidity is clear considering that, while the mass flow is proportional to the pitch, the velocity gradient is proportional to the inverse ratio of the chord. Looking at Figure 2.9, it is possible to see a good agreement with

Figure 2.8 and to observe that the momentum thickness stays low and constant for diffusion factor lower than 0.6; as above that value the momentum thickness starts to rise more steeply, it can be considered as a blade stall inception condition. In the design a value around 0.4 is usually chosen along spanwise direction, while at hub a slightly higher value is allowed. From these imposed thresholds and from the flow angles coming from the velocity triangles, it is possible to compute a reasonable value for the solidity, which unfortunately does not represent yet the optimum configuration.

Further development in the expression of the diffusion factor, proposed by Lieblein and his co-workers, permitted to overcome some of the hypothesis of the first relation:

- Inlet and outlet radii (and consequently mean radius $\overline{r}$ and mean pitch solidity $\overline{\sigma}$) are introduced for not axial stages
- To take into account a variation of the meridional velocity, the ratio between inlet and outlet and the mean value are introduced
- If the incidence does not correspond to the reference condition, a corrective factor and an empiric coefficient a are introduced

The result is the definition of the equivalent diffusion factor:

$$D_{eq} = \frac{V_{1m}}{V_{2m}} \left[1.12 + a\left(i - i_{ref}\right)^{1.43} + 0.61 \frac{\cos^2 \alpha_1}{\sigma} \frac{r_1 V_{1t} - r_2 V_{2t}}{\overline{V_m}} \right] \tag{2.19}$$

2.3.3 Loss prediction models

Lieblein

Considering the following definition of losses, Lieblein found a relation with the diffusion factor for different solidities and air inlet angles.

$$\omega = \frac{p_{01} - p_{02}}{p_{01} - p_{s1}} \quad \text{(for a stator)} \tag{2.20}$$

$$\omega = \frac{p_{r,01} - p_{r,02}}{p_{r,01} - p_{s1}} \quad \text{(for a rotor)} \tag{2.21}$$

For an incompressible flow, the total pressure losses coefficient of a generic row could be roughly considered equal to the wake momentum thickness $\theta_t = \frac{\theta}{s \cos \alpha_2}$ where $\theta = \theta_{ventre} + \theta_{dorso}$:

$$\omega_2 = 2 \frac{\theta}{s \cos \alpha_2} = 2 \frac{\theta \sigma}{c \cos \alpha_2} \tag{2.22}$$

which can be defined using the inlet section as reference, as usually occurs for compressor application:

$$\omega_1 = 2 \frac{\theta \sigma}{c \cos \alpha_2} \left(\frac{\cos \alpha_1}{\cos \alpha_2} \right)^2 \tag{2.23}$$

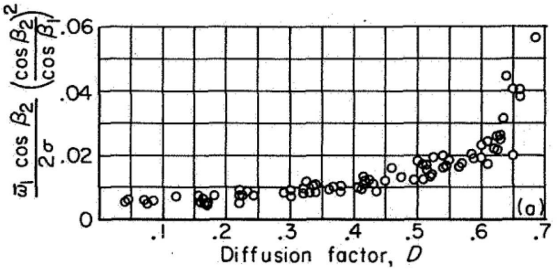

(a)

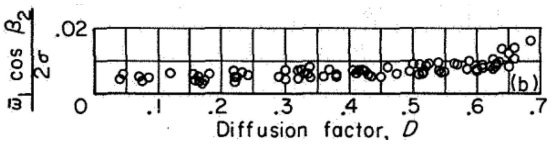

(b)

Figure 2.10: Different expression for momentum thickness in function of diffusion factor

Lieblein developed a more accurate expression, specific for axial flow compressors based on the boundary layer shape factor $H = \frac{\theta^*}{\delta}$, evaluated in the trailing edge:

$$\omega_1 = 2\frac{\theta\sigma}{c\cos\alpha_2}\left(\frac{\cos\alpha_1}{\cos\alpha_2}\right)^2\left\{\left(\frac{2H}{3H-1}\right)\left(1-\frac{\theta\sigma}{c\cos\alpha_2}H\right)^{-3}\right\} \tag{2.24}$$

Assuming $H = 1.08$ and θ/c from Figure 2.8 or 2.9, Lieblein himself pointed out that the expression inside the brackets can be considered as constant of unitary value, making the relation simple. Usually two different parameters are considered to estimate the wake momentum thickness:

$$\omega = 2\left(\frac{\theta}{c}\right)\left(\frac{\sigma}{\cos(\alpha_2)}\right)^2\begin{cases}\frac{\theta}{c}\approx\frac{\omega\cos(\alpha_2)}{2\sigma}\\ \frac{\theta}{c}\approx\frac{\omega\cos(\alpha_2)}{2\sigma}\left(\frac{\cos\alpha_1}{\cos\alpha_2}\right)^2\end{cases} \tag{2.25}$$

In Figure 2.10 are plotted the two different expressions for the momentum thickness in function of the diffusion factor; both 2.10(a) and 2.10(b) fit very well with plot in Figure 2.9, but it must be noticed that, even if it is most commonly used and widely cited, the loss parameter $\frac{\omega\cos(\alpha_2)}{2\sigma}$ is not as good as the other one to indicate the stall, because of its flat trend.

A similar plot can be drawn in function of a different parameter, which is related to the diffusion ratio $V_{max,1}/V_1$, but is based on readily calculated inlet and outlet conditions. The equivalent diffusion ratio D^*_{eq} can be empirically computed as follows:

$$D^*_{eq} = \frac{\cos(\alpha_2)}{\cos(\alpha_1)}\left[1.12 + a\left(\alpha-\alpha^*\right)^{1.43} + 0.61\frac{\cos^2\alpha_1}{\sigma}\left(\tan\alpha_1-\tan\alpha_2\right)\right] \tag{2.26}$$

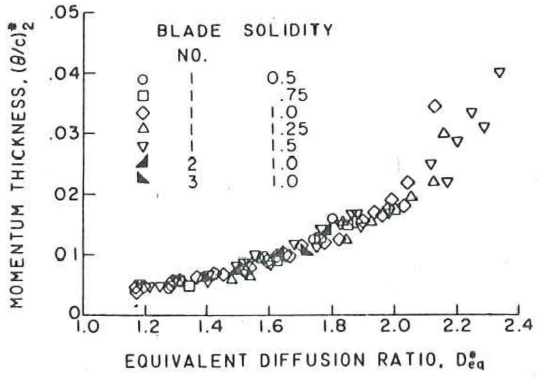

Figure 2.11: Momentum thickness in function of equivalent diffusion ratio

where α^* represents the inlet flow angle in which the losses are at the minimum value. In Figure 2.11 the wake momentum thickness chord-adimensionalized is plotted in function of equivalent diffusion ratio. It can be seen that, above a value of 1.8, the flow is separated by the suction surface.

In Figure 2.12 the losses computed according to the Lieblein correlation are plotted in function of the solidity, for different inlet flow angles and different air turning angles. The curves present a minimum for very low value of solidity, which usually would occur after the stall point (represented on the plots as a white dot).

Koch and Smith

In the '70s Koch and Smith developed the most complete loss prediction model for axial-flow compressors (ref. [5]). The work is constructed on rational fluid-dynamic elements, such as boundary layer theory and on the experimental results from a series of over 40 General Electric low-speed multi-stage compressors. The results show a good agreement with Lieblein's work but enlighten better the effects of some physical phenomena on the performances, as Axial Velocity Density Ratio (AVDR), Reynolds number and maximum thickness to chord ratio.

Wright and Miller

On the basis by Koch and Smith, Wright and Miller developed the performance prediction method used by Rolls Royce. They upgraded the definition of the diffusion factor to take into account the correction for maximum thickness and considering AVDR different than 1:

$$D_{eq} = \left[1 - \frac{W_2}{W_1} + \left(1 + \frac{t_{max}}{c}\left(10.116 - 34.15\frac{t_{mac}}{c}\right)\right)\right]\frac{W_1}{W_2} + 1 \tag{2.27}$$

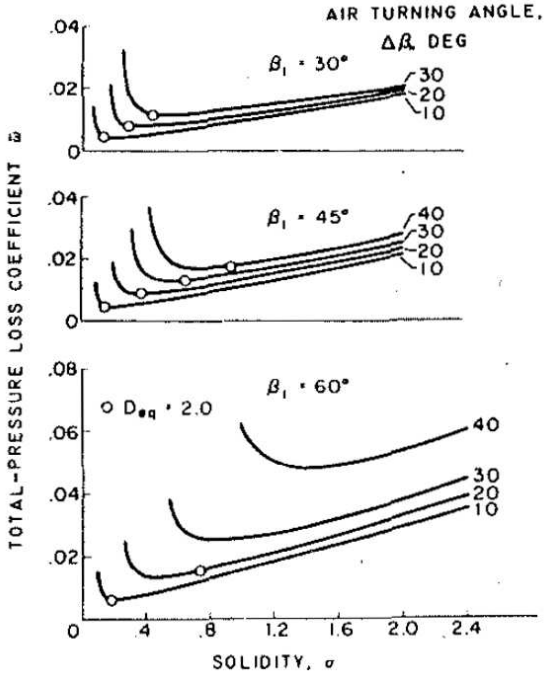

Figure 2.12: Lieblein model: Losses in function of solidity

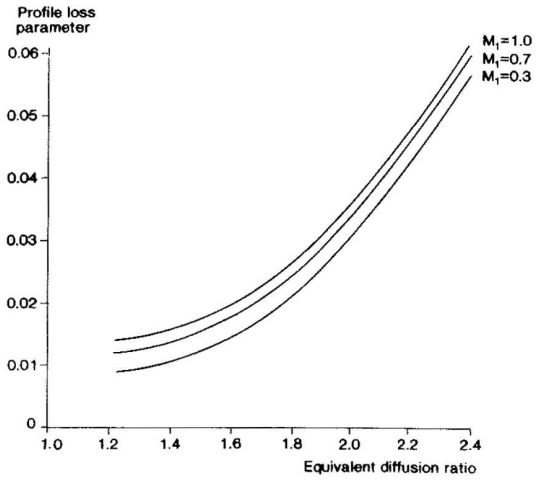

Figure 2.13: Wright and Miller model: Losses in function of equivalent diffusion ratio

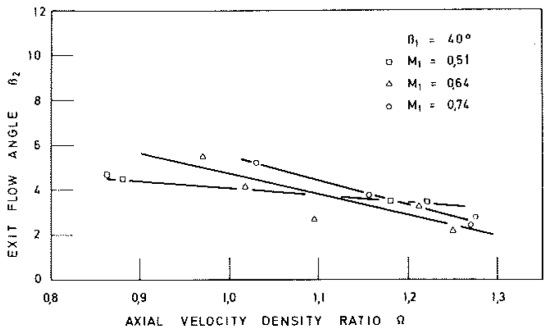

Figure 2.14: Outlet flow anlge in function of AVDR

In Figure 2.13 the correlation is shown for different mach numbers; even if the loss parameter is not declared, it is likely $\frac{\omega\cos(\beta_2)}{2\sigma}\left(\frac{W_2}{W_1}\right)^2$.

2.3.4 Effect of Axial Velocity Density Ratio

In the assessment of an axial-flow compressor cascade an important parameter which must be kept under control is the Axial Velocity Density Ratio, defined as follows:

$$AVDR = \frac{\rho_2 v_{ax2}}{\rho_1 v_{ax1}} \tag{2.28}$$

This quantity allow to quantify the two-dimensional nature of the flow, giving a hint on the stream-tube contraction due to the development of the end-wall boundary layers. Even if this parameter must be usually kept slightly above its unitary value, it is common practice, especially for low pressure turbomachinery stages, to relax this constraint, for instance because the strong change in radii of the channel would not permit a different design.

As far as concerns the effect on the deviation angle, it is interesting to note that the cascade wind tunnel which produced the results used by Lieblein (description by Emery et al. in reference [12]) was provided with system for the suction of the end-walls boundary layers, allowing to maintain a low AVDR. This circumstance plays an important role in the generalization of the results: even if Koch and Smith adapted the definition of the diffusion factor to fit different values of AVDR, no correlation is available to predict the change in the deviation angle. On the contrary Carter's experiments were conducted with an AVDR around 1.2, giving thus accurate results with a more general effectiveness for common design choices. Studies by Breugelmans and al. (ref. [13])show a decrease of the losses and of outlet flow angle with an increase in the avdr, as presented in Figure 2.14 and 2.15. These results suggest that NASA deviation rules generally overpredict the deviation angle (with a gap of 1-2 deg respect to Carter's rule) if AVDR is greater than 1. Felix and Emery showed (ref. [14])that up to 3 deg more turning in

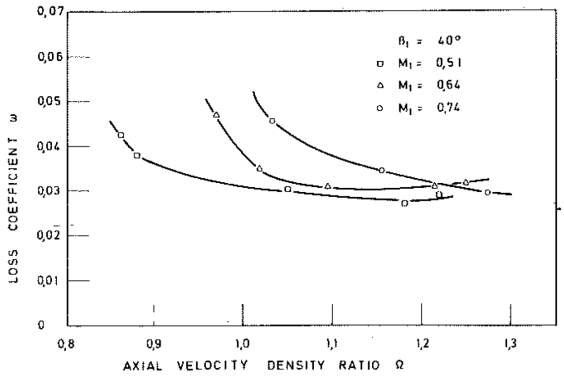

Figure 2.15: Losses in function of AVDR

the test can be attributed to the AVDR effect. Pollard and Gostelow proposed the following quantitative rule:

$$\delta - \delta_1 = \xi\,(1 - \text{AVDR}) \tag{2.29}$$

where δ_1 is the deviation for unitary AVDR. As far as concerns the value for ξ it appears to vary between 8 and 10, according to the blade shape. In the end then, a general satisfactory correlation for different values of avdr is still not available.

2.3.5 Effect of viscosity and compressibility

Most of the cited correlations do not allow to highlight the effects of viscosity and compressibility, due to the characteristics of the experimental data on which they are based, usually extracted from inlet Mach number below 0.3 for high Reynolds number, for which fully turbulent flows can be assumed. However other experiments can be considered to have at least a qualitative idea of the phenomenon.

In Figure 2.17 and 2.18 is displayed the usual behaviour of subsonic cascades in terms of losses in function of the mach number at two different Reynolds numbers; the effects of shock losses can be observed to appear in a range of Mach number from 0.7 to 0.8, depending on the profile design. Reference [15] reports the results of two years of work carried out from 1966 to 1968 by researchers of the Deutsche Versuchsanstalt für Luftfahrt (DVL) on the performance of transonic and supersonic compressor cascades. As far as concerns the role of solidity, the data are displayed in Figure 2.19; they show that, for slighlty supersonic flows, there are two different trends: if Mach number is lower the 1.2, the losses increase with the solidity, probably due to the predominant role of the profile losses in this range; when the shock losses increase the trend is inverted, decreasing for higher solidity. Considering the reduction in the pitch distance, trough which the increase in solidity was achieved by the authors, the distance between the leading

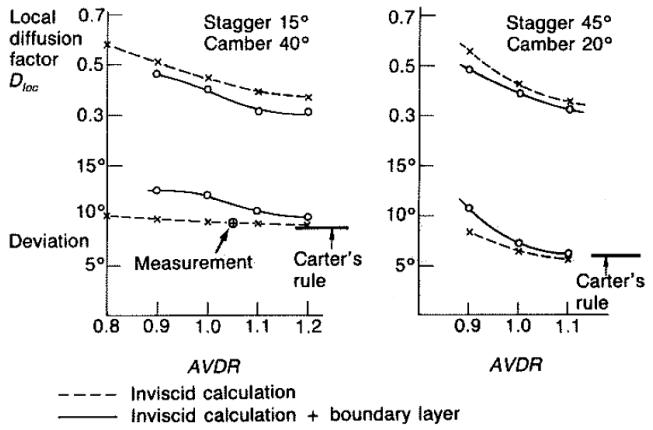

Figure 2.16: Local diffusion factor and deviation as a function of AVDR. C4 sections, $\sigma = 1.0, t/c = 10\%$, incidence zero, inlet mach number $M_1 = 0.3$

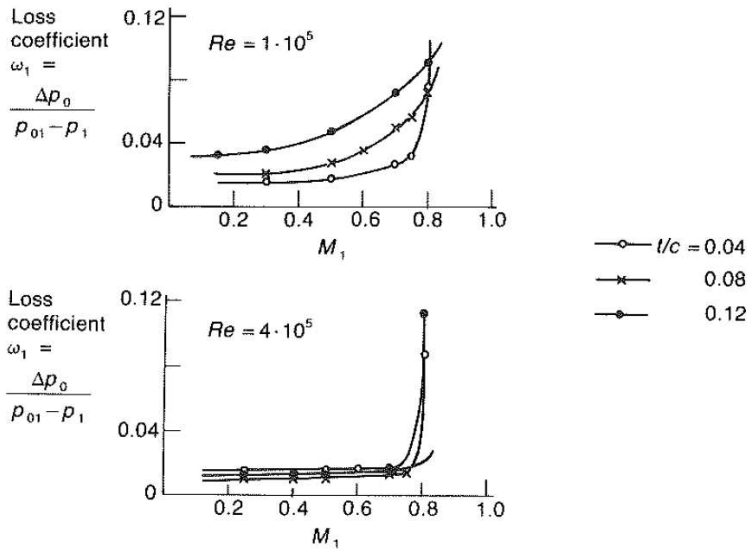

Figure 2.17: Loss versus Mach number for NACA-65 cascades of different thickness at two Reynolds numbers. Stagger 40°, approx. camber 15°, solidity 1.0, flow inlet angle $\alpha_1 = 50°$.

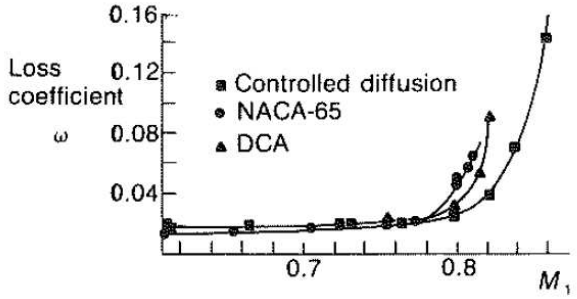

Figure 2.18: Loss and useful incidence range measured for three cascades, one a controlled diffusion (supercritical) type. (Solidity 0.933 for all cascades; at design $M_1 = 0.7$, $\alpha_1 = 60°$, $\alpha_2 = 46.4°$, AVDR = 1.07

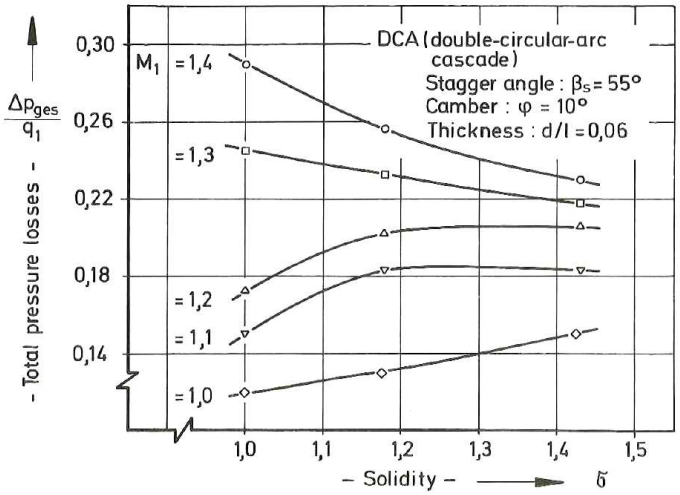

Figure 2.19: Losses in function of mach number and solidity for DCA profile.

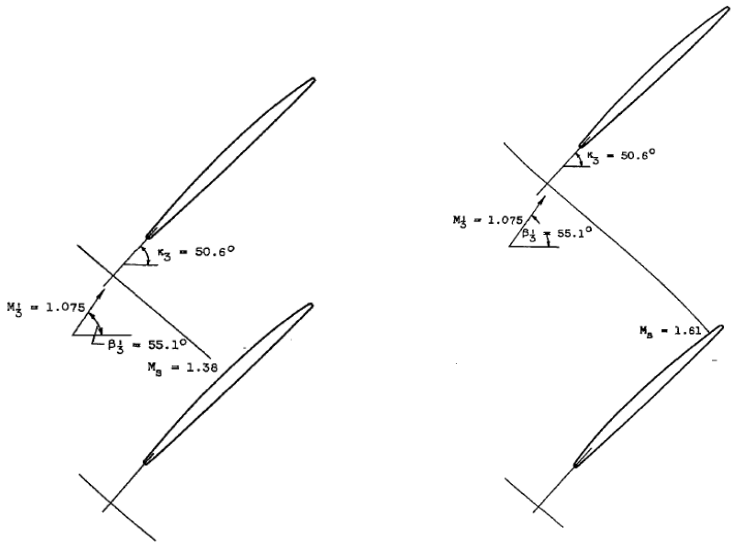

(a) 35-Blade rotor. Blade element solidity,1.00

(b) 22-Blade rotor. Blade element solidity,0.63

Figure 2.20: Supersonic flow through a cascade indicating change with solidity of location of bow Wave on blade suction surface and resulting blade auction-surface Mach numbers preceding the shock. Outlet radius, 8.60 inches.

edge and the passage shock location decreases itself, causing the expansion rate to decrease on the suction side and lowering the Mach number in front of the passage shock. The reduced shock strength causes lower losses. The same behaviour was observed and described by Schwenk and al. (ref. [16] and [17]). These phenomena are schematized in Figure 2.20

The viscosity effect can be outlined from the plots in Figure 2.17 and 2.21. The losses present a flat behaviour for $Re > 1 \cdot 10^5$, increasing abruptly below that value and specially for thicker profiles.

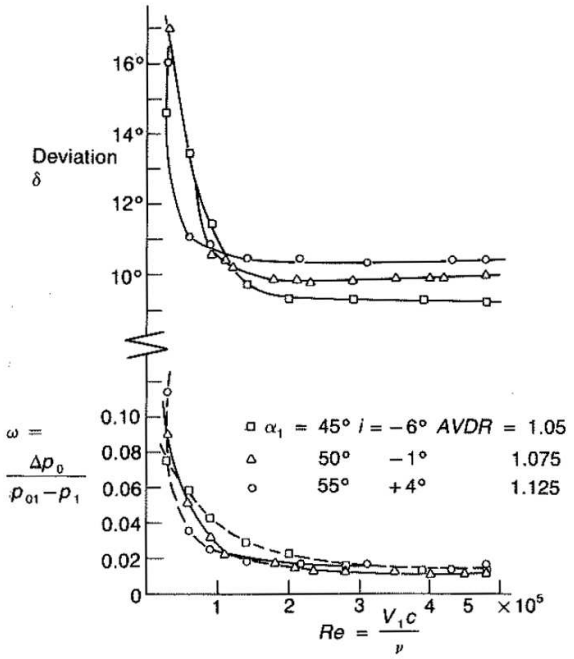

Figure 2.21: Deviation and loss versus Reynolds number for C4 blade in cascade. Incidence $i = -1°$. Stagger 36.5°, camber 30°, solidity 1.0, thickness-chord ratio 0.10. Inlet Mach number $M_1 < 0.15$. AVDR quoted at $Re = 3 \cdot 10^5$.

2.4 Three-dimensional investigation

While widely used to foresee the behaviour of two-dimensional cascades, the correlations cited above do not allow to describe the performances of three-dimensional cascades, showing big discrepancies if compared with results from 3D compressor tests. Figure2.22 shows a comparison between linear and annular cascade data for a rotor and a stator at different radii, in terms of total pressure loss parameter, defined as follows:

$$\zeta = \frac{\overline{\omega}\cos\beta_2}{2\sigma} \tag{2.30}$$

in function of diffusion factor. As far concerns the stator, a similar behaviour for the different radii can be underlined, usually showing lower losses for the cascade test. The rotor seems more sensitive because the losses are not only higher for the mean and the hub ratio but shows quite a different (and more critical) behaviour at tip.

2.4.1 Correlation between 2D and 3D data

An attempt to solve the lack of accuracy of regular cascade testing was proposed by Robinson et al. [18], providing empirical correlations to correct the the two-dimensional results based on annular cascades measurements, through the use of fitted curves, which allow to quantify the three dimensional effects on incidence, losses and deviation, for instance. An example is shown in Figure 2.23.

2.4.2 Experimental results

Standahar and Serovy

The effect of solidity in annular cascade was firstly studied by Standahar and Serovy in 1952 (ref. [19] in the Lewis Flight Propulsion Laboratory of NACA, through the assessment of the performance of a rotor row with and without downstream stator blades, varying the blade number and hence the pitch distance.

An increase in the peak pressure ratio is registered while increasing solidity, as predictable from cascade data since it depends mostly on the turning which increase for high solidity, specially for low weight flow. The higher blockage of the high solidity rotor causes a shift of the mass-flow to lower values in the correspondent throttle condition, which is reflected on the pressure ratio. The efficiency behaviour does not match directly with cascade data: for a given equivalent tip speed the peak value of efficiency for all three rotor solidities were approximately the same, but the correspondent weight flow is lower for the higher solidity. Due to the increase in losses caused by blade stall and separation, the efficiency at low weight flow is lower.

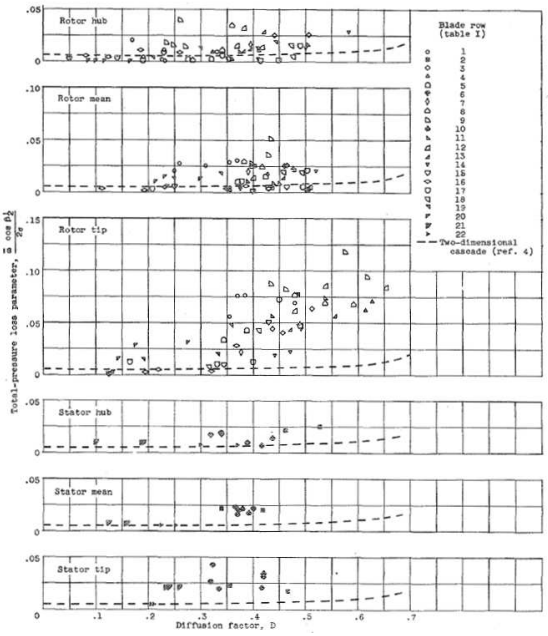

Figure 2.22: Variation of total pressure loss parameter with diffusion factor at reference incidence angle for NAca 65 (A_{10})-series and DCA blade sections

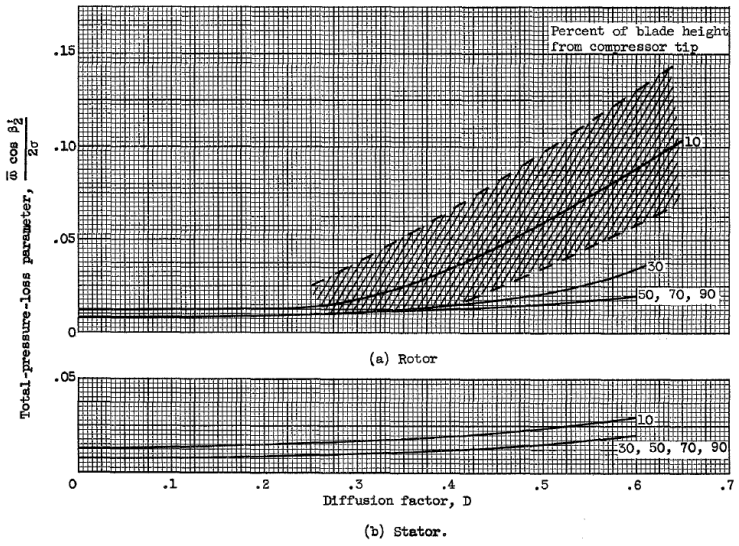

Figure 2.23: Deduced variation of total-pressure-loss parameter with diffusion factor at reference incidence angle for NACA 65(A_{10})-series and double-circular-arc blades

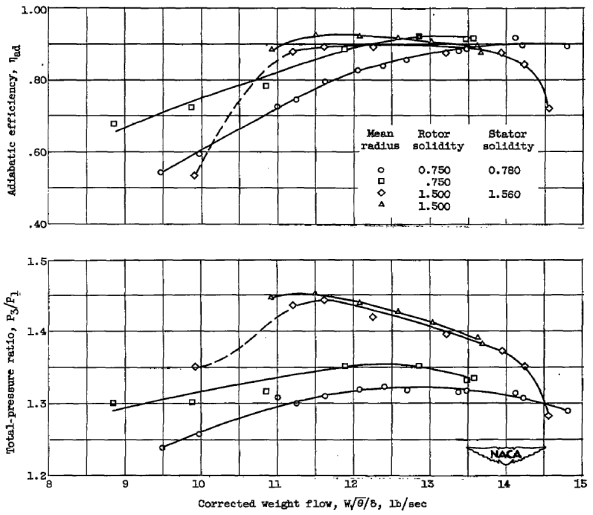

Figure 2.24: Variation of total-pressure ratio and adiabatic efficiency for complete compressor stage with corrected weight flow. Equivaelnt tip speed 836 ft/s (29 m/s)

Medeiros and Hatch

In the framework of a campaign on the effect of different blades modifications on the performance of a 16 stages axial flow compressor, Medeiros and Hatch (ref. [20]) conducted some experiments on a reduction of 20 percent in solidity on the last 3 stages, achieved by the reduction in the number of blades. The stator blade row solidity in the exit stages were not changed, because of availability problems. Their results show an increase in efficiency from 2 to 3 percentage points at equivalent speeds of 50, 65 and 80 percent of design, while at other speed the different are within the limits of the accuracy of measurement. As far as concerns the mass flow, a slight general increase is registered for all the operative condition apart from the one at 75 percent of the equivalent design speed. No change in the surge limit is registered. The change in the turning angle is less than 1/2° at lower angles of attack that would be encountered in the exit stage at part speed. The higher choking weight flow for lower solidity is indicated by the fact that the negative-stall high-drag region occurs at a lower angle of attack. The positive stall angle of attack also decreases for the lower solidity. At surge flow at design speed and at speed above design, the exit stages will operate at or near the stall angle of attack and then the surge pressure ratio at these speed will be decreased.

Schwenk, Tyls and Lewis

In the middle fifties Schwenk and other colleagues investigated the performance of two different transonic compressors for three different values of solidity; the results are reported in [16] and [17]. In both cases the reduction in solidity was achieved through a reduction in the number of blades. While the pressure ratio behaves quite predictably, unexpected effects show up in the losses and pressure ratio trends: while for hub and mean regions losses are lower than in the tip region and tended to decrease when reducing solidity for all rotating speeds, in agreement with cascade correlations, at design speed and at its 90 percent, the losses in tip region significantly increase when removing the rotor blades. As far as concerns the lower speeds, the minimum-losses levels near to the blade-tip were the same level for all rotors and no distinct solidity effect could be established. These authors investigated also different stall pattern for the different solidities, at low speed: while in the low solidities rotors large non-periodic fluctuations were observed, for the high solidities ones the periodic fluctuations registered are usually associated to a typical rotating stall; these low-amplitude oscillations are present at lower mass flow than the low-solidity stages, providing a good hint on the good effect of reduced pitch on the stability range.

Turner and Burrows

In Great Britain Turner and Burrows of the National Gas Turbine Establishment, investigated the effect of three different values of pitch chord ratio (respectively $\sigma = 2$,$\sigma = 1.52$ and $\sigma = 1.06$) on two stages low stagger free vortex blading. This work,published in 1960 and reported in [21], take as main reference the technical report *"The effect of pitch chord ratio on the low speed characteristics of a compressor"* written by Bonham in 1953; this work is unfortunately unavailable. The experiments of Turner and Burrows were conducted at low speed as well, at 900 rpm. The results show a good agreement with the cascade correlation and the similar investigation conducted overseas: decreasing the number of blades the efficiency increase and the pressure ratio decrease, as shown in Figure2.25. Notwithstanding the following different behaviour must be noticed:

- for the low solidity rotor, near to surge, both the efficiency and the pressure ratio lessen to values considerably below the other two configurations
- for the high solidity rotor, near to choke, both the efficiency and the pressure ratio substantially decrease

Osborn, Urasek and Moore

Between 1972 and 1973, Osborne, Urasek and Moore National Aeronautics and Space Administration (NASA) conducted some experiments on three different compressors with different tip solidities (respectively 1.3,1.5,1.7). The results,

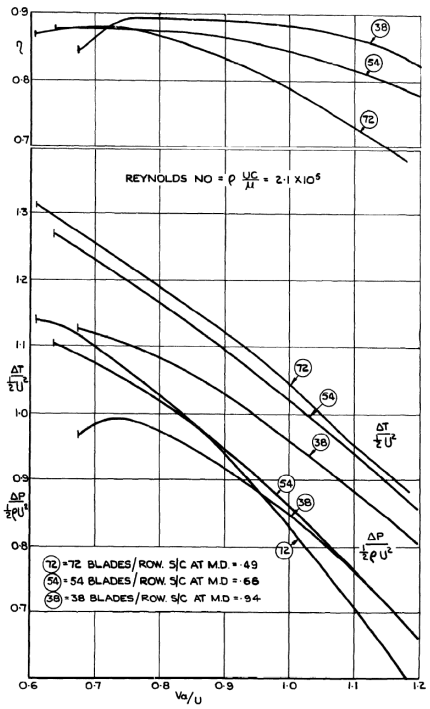

Figure 2.25: Comparison of mean span characteristics at three blade pitchings. 900 rev/min.

presented in [22], [23], [24], appears to be rather out of line with the previous works; the efficiency and the pressure ratio registered for the higher solidity fan are the worst and the stall margin is quite reduced, as well. As explanation to such unexpected results, the authors blame an underestimation of the stator performances, due to a bad design of the component.

Bissanti, Di Tommaso, Scrofani

A research conducted in the laboratories of the aeronautical institute of the University of Palermo engineering faculty investigated the solidity and incidence effect on two-dimensional transonic high-camber decelerating cascades. Considering $i = 0°$, the authors observed the behaviour of three different configurations, respectively $\sigma = 0.8$,$\sigma = 1.2$,$\sigma = 1.6$, pointing out the following conclusions:

- the higher the solidity, the higher the decelration of the fluid
- the deflection is higher for the middle configuration; in all the three cases the deflection appears quite flat in the lower range of Mach number, increasing suddenly in correspondence of three different threshold ($M_1 = 0.45$ per $\sigma = 0.8$, $M_1 = 0.6$ per $\sigma = 1.2$ and $M_1 = 0.65$ per $\sigma = 1.6$) as effect of the blockage
- the results show an analogous behaviour in term of pressure ratio, characterized by higher losses for the solidity of 1.2; furthermore the higher the solidity, the lower the influence of the incidence variation

Bristch, Osborn and Laessig

The results of an experimental campaign on the effect of diffusion factor, aspect ratio, and solidity on overall performance of 14 compressor middle stages, conducted by NASA, were published in 1979. The greater blade blockage induced by the increased number of blades for the high solidity rotor was confirmed. The shift in the performances curves to lower mass flows for an increase in solidity and the improvements in the efficiency and peak pressure ratio were observed, as well. Moreover the benefits of a decrease in solidity were outlined in terms of stall margin and considering the lower surge margin and the bad performance at high mass-flow for high solidity stages. The following statement appears to be of great interest for the present analysis: "*No significant change in the minimum-efficiency difference occurred when stator solidity was lowered. Therefore, stator designs with fewer blades, and hence lower solidity, would mean lower fabrication cost without sacrificing performance*".

2.5 The optimum solidity

The number of studies and correlations reported in the previous section, conducted by the most important research institutions all over the world, clearly

show the importance and the sensitivity of the topic; to make matters worse it must be noticed that, even if the previous researches can give useful hints on the effect of solidity for the design process, none of them allows by itself to chose the optimum solidity without the support of a loss prediction model or of an iterative process. Moreover, even coupling the loss prediction model and the blade loading criterion by each author, the comparison between the results appears to be quite difficult, each of them leading to rather different solutions.

As presented in section 1.2, after the definition of the upstream and downstream conditions, based on an isentropic radial equilibrium calculation, a blade profile must be selected in order to achieve the desired turning. The choice of stagger, camber and solidity in the range of incidence and deviation desired, can be used for a rough quantification of the losses. The correlations reported in Eq. 2.10, Eq. 2.12 and Eq. 2.17 by Zweifel, Carter and Lieblein can be used to set a reasonable value for the solidity, giving the designer a first guess to start with; the process is quite similar for each one of the three methods: a constraint is imposed for a parameter which is defined to quantify the blade loading and is linked to the losses behaviour; hence imposing a desired level of losses is it possible to compute the desired value of the blade loading parameter and eventually of the solidity. It must be said that, even if the most suitable option to calculate the parameter is usually the best efficiency point, it might be possible, in order to fulfil other requirements to choose a different design condition, admitting thus higher losses. That is the case of the TechspaceAero (TSA) profile; its design point has been chosen to guarantee a convenient incidence range.

As the approach by Lieblein seemed to be the most accurate, some developments of this method have been carried out by different authors. In the following section the works by McKenzie (ref. [25]), Hearsey (ref. [26]) and Liu (ref. [27] will be presented.

2.5.1 Correlations

Hearsey

Within his contribute to the volume "*Advanced topics in turbomachinery technology*", Hearsey proposes a simple loss model, based on the Lieblein theory of diffusion factor. To improve the estimation of the wake momentum thickness, the author prefers to use the following parameter:

$$\zeta_{Hearsey} = \frac{\omega \cos\left(\beta_2\right)}{2\sigma} \left(\frac{\cos\left(\beta_2\right)}{\cos\left(\beta_1\right)}\right)^2 \tag{2.31}$$

rather than the one mainly used by Lieblein ($\zeta = \frac{\omega \cos(\beta_2)}{2\sigma}$). Fitting the experimental data with an exponential low, it is possible, given the inlet and outlet flow values, to calculate the losses in function of D:

$$\zeta_{Hearsey} = 0.004 e^{6.16773\, D^{1.436794}} \tag{2.32}$$

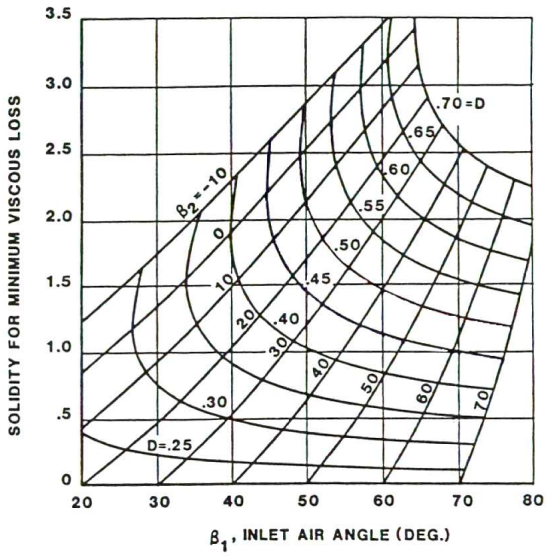

Figure 2.26: Hearsey model: Solidity and D-Factor for Minimum Viscous Loss versus Inlet and Outlet Air Angles

Putting the derivative respect to the solidity equal to zero, a minimum of the function $\zeta_{Hearsey} = \zeta_{Hearsey}(\sigma)$ is found. Considering, for instance, a rotor with a change in radius, the optimum solidity can be computed through the following implicit equation:

$$\sigma_{opt} = \frac{8.861805\,\Delta(rW_\theta)}{r_m W_1} D_{opt}^{0.436794} \tag{2.33}$$

where D_{opt} is the diffusion factor calculated with σ_{opt}. Neglecting the change in radius and axial velocity, the optimum solidity can be easily calculated from the flow angles; a map of this method is shown in Figure 2.26. As reported in the caption, this method takes into account the viscous losses and thus does not allow to take into account the shock losses, typical of some working conditions of transonic stages.

McKenzie

The Rolls Royce Aero Division conducted as well studies on the solidity effect; some of the results are reported by McKenzie in reference [25] and [28]. The choice of solidity is linked to the pressure coefficient, defined as follows:

$$C_{p_i} = 1 - AVDR^2 \frac{\cos^2\alpha_1}{\cos^2\alpha_2} \tag{2.34}$$

which can be defined otherwise as the ideal static pressure rise

$$C_{p_i} = \frac{p_{s,2} - p_{s,1}}{1/2\,\rho_1 w_1^2} \tag{2.35}$$

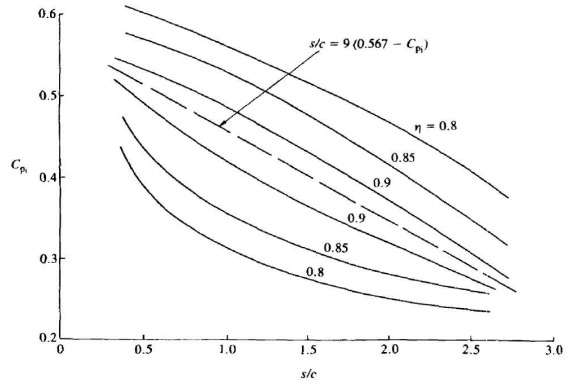

Figure 2.27: McKenzie linear model: Pressure coefficient versus $s/c = 1/\sigma$ for different efficiency levels

The relation between this parameter and the inverse of solidity appears to be linear, governed by the following equation:

$$\frac{s}{c} = 9\left(0.567 - C_{p_i}\right) \tag{2.36}$$

In Figure 2.27 are plotted the results for different efficiency.

Liu

One of the latest investigation on the present topic is reported by Liu in his article "*Simple formulae for optimal solidity of two dimensional compressor cascades based on diffusion concept*" (ref. [27]). In the theoretical study, two different kind of problems are considered:

- optimal solidity that minimizes the profile losses
- optimal solidity that maximizes the circulation around a cascade profile (and maximizes also the blade loading)

In the two cases a constraint is imposed, in terms of diffusion factor or equivalent diffusion factor. Considering the second quantity, it can be observed that

$$D_{eq} = \frac{\cos\beta_2}{\cos\beta_1}\left(1.12 + 0.61\cos^2\beta_1\left(\tan\beta_1 - \tan\beta_2\right)\tau\right) \tag{2.37}$$

where $\tau = \frac{1}{\sigma}$. Using a short notation, referring with k_2 to the contribution of the divergence of the flow channel and with k_3 to the contribution of the deflection, it is possible to express:

$$D_{eq} = k_2 + k_3 \cdot \tau \tag{2.38}$$

span	β_1	β_2	w_1	w_2
hub	49°	18°	263 m/s	207 m/s
mid	48°	28°	255 m/s	197 m/s
tip	49°	39°	252 m/s	192 m/s

Table 2.2: DREAM project booster data

Span	Howell	Zweifel (Ψ_a =0.9)	Lieblein (D=0.36)	Hearsey	McKenzie	Liu	DREAM
10%	1.76	1.63	1.66	1.5	0.54	0.96	1.52
50%	0.9	1.25	1.37	1.13	0.61	0.89	1.28
90%	0.49	0.98	1.16	0.87	0.59	0.82	1.26

Table 2.3: Optimum solidity according to different auothors for DREAM project booster

the maximum value that can be assumed by the equivalent diffusion factor, represented by k_4, lays between 1.9 and 2.0. Considering firstly the effect on the losses according to the model proposed by Scholz (1965), the optimum solidity can be found as follows

$$\sigma_{opt} = \begin{cases} \frac{k_3}{1.0534-0.434k_2} & \text{for} \quad k_2 < b \\ \frac{k_3}{k_4-k_2} & \text{for} \quad k_2 > b \end{cases} \tag{2.39}$$

where $b = (k_4 - 1.0534)/0.566$. Considering the maximization of the circulation, it is possible to get the following expression:

$$\sigma'_{opt} = \frac{k_3}{k_4 - k_2} \tag{2.40}$$

Comparing the two different problems, one can notice that, for $k_2 > b$, $\sigma_{opt} = \sigma'_{opt}$, but unfortunately, while $k_2 < b$, $\sigma_{opt} > \sigma'_{opt}$ the choice of solidity is not univocal.

2.5.2 Comparison

A comparison of almost all the previous different correlation is presented in reference [2]; the application of Liu formulation has been added in the present work. The equations are applied to the booster of the DREAM project, cited in section 1, whose velocities triangles are reported in Table 2.2.

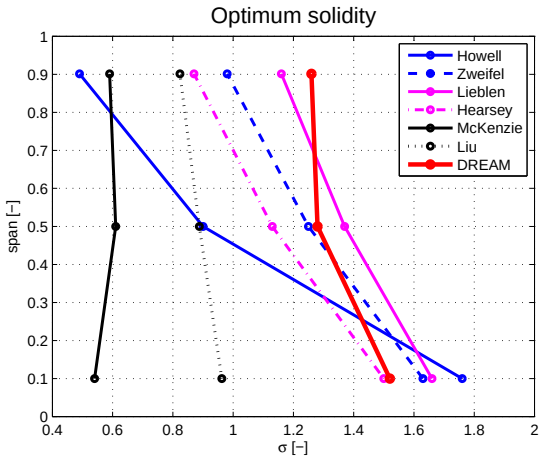

Figure 2.28: Comparison between different correlation for optimum solidity

The results of the comparison are shown in Table 2.3 and Figure 2.28. The value suggested by McKenzie and Liu appears to be quite low and far from the state of the art, represented by the DREAM solidity. As this circumstance appears to be quite reasonable for the first author, who specifies that the correlation is intended mainly for fan and highly staggered blade configurations design, is not possible to set the work by Liu in a proper framework, because it is essentially based on theoretical basis and the results of its application to machine design are still unknown. The solidity values by Howell present an extended range from tip to hub, while the correlations by Lieblein, Zweifel and Hearsey, even with differences far from neglectable, appear to be, at least for the trend consistent with the state of art design. Furthermore it must be noticed that, while Zweifel and Lieblein correlations allows to control and spread the loading among the span by adapting the solidity, Howell's, Hearsey's and McKenzie's procedures are quite strictly linked to the optimum conditions they are based on.

In terms of diffusion factor (see Figure 2.29), it can be noticed that Hearsey's and Zweifel's correlations lead to an high value of diffusion at the tip, even exceeding, sometimes, the limits usually suggested for design process ($D \cong 0.4$). Hearsey's procedure can lead to an overloading condition at certain span location, due to the fact that is based on an optimization of the efficiency rather than on diffusion control. Using Zweifel coefficient or the diffusion level, the loading can be adjusted according to the designer experience.

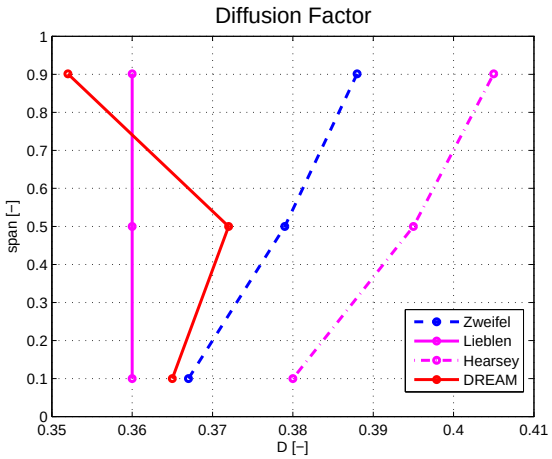

Figure 2.29: Comparison between of the diffusion factor corresponding to the correlation for optimum solidity

2.6 Conclusions

Th effect of solidity on compressor performance and stability has been investigated by numerous authors, but a complete study on the subject has not been performed yet. Moreover, computational fluid dynamics approach is still not employed for investigations on this topic.

To summarize the evidences present in literature on the subjects, the following general patterns can be outlined:

- the pressure ratio increase with the solidity, as the guidance and the turning are improved
- the stall margin increase with the solidity, due to the reduction in blade loading
- the efficiency present a negative trend respect to solidity, as consequence of the extended wet surface
- the operating mass-flow decrease while the solidity is increasing, for all the throttle positions.
- no equation or correlation is available to predict straightforward the optimum value of solidity, as the different attempts made lead to quite different results

Chapter 3

Model set-up

During the numerical model development, the following two main goals are taken into consideration, to achieve specific characteristics and performance for the present application:

Accuracy - As the simulation is mainly meant to foresee an experiment, the target accuracy should be at least the same of the experimental measurements.

Computation time - As the complete map from choke to stall is performed for eight different configurations, the number of simulations required is considerable; for this reason the computation time of each calculation should be limited at the minimum value.

As these main objectives appear to be antithetic, a trade off between them is considered. In this chapter, after a short presentation of the CFD software, all the settings of the model are given with regards to the grid generation, the mathematical and turbulence modelling, the boundary conditions and the flow solver. However, considering the final goal, the starting section is dedicated to a preliminary evaluation of the experimental uncertainty which will set the accuracy standards for the present work.

3.1 Uncertainty forecast

The objective of this work is the forecast of the experimental tests focused on the behaviour of a linear compressor cascade concerning the effect of solidity; while a proper assessment of the measurements uncertainties will be carried out for the experimental campaign (out of the present framework), a simple model to predict at least the order of magnitude of the measured quantities is necessary to set the standard accuracy of the model. The numerical model uncertainty assessment is outside the objective of the present work; however it appears useless to look for a highly accurate solution, i.e. the asymptotic value, with the model, through

Quantity	x_i	δx_i	U. d. m.
Static pressure	P_s	50	Pa
Inlet total pressure	P_{01}	50	Pa
Outlet total pressure	P_{02}	200	Pa
Flow angle	α	0.3	deg
Total temperature	T_T	1	deg

Table 3.1: Experimental uncertainty values

an extended use of time and resources, if the results can not be validated with experimental data presenting the same degree of reliability. Then the model (with special regard to the mesh) is set in a way that a further refinement will not affect the results in a measurable way.

The steady performance measurements will take place upstream and downstream of the cascade, concerning the following quantities:

- ✧ Flow angle
- ✧ Total temperature
- ✧ Static pressure
- ✧ Total pressure

The other quantities of interest, such as Mach number, density, velocity, mass flow, efficiency, pressure ratio will be computed from the measured data; it is important to understand the impact of the direct measurements uncertainty on the computed values, namely the uncertainty propagation. Considering the quantity F depending on the parameters $(x_1, x_2, \ldots, x_n)$ characterized by the uncertainty $(\delta x_1, \delta x_2, \ldots, \delta x_n)$, the uncertainty on F will be given by the following equation:

$$\delta F = \sqrt{\sum_{i=1}^{n} \left(\frac{\partial F}{\partial x_i} \delta x_i \right)^2} \tag{3.1}$$

Considering, for instance, the uncertainty of total pressure ratio β, which depends on inlet and outlet total pressures, respectively P_{01} and P_{02}, it can be computed as follows:

$$\delta \beta = \sqrt{\left(\frac{1}{P_{01}} \delta P_{02} \right)^2 + \left(-\frac{P_{02}}{P_{01}^2} \delta P_{01} \right)^2} \tag{3.2}$$

Quantity	Maxim. uncertainty
M_1	$2.5E-4$
M_2	$3.2E-4$
PR	$9.7E-4$
ω	$6E-3$

Table 3.2: Expected uncertainty values for the main design quantities

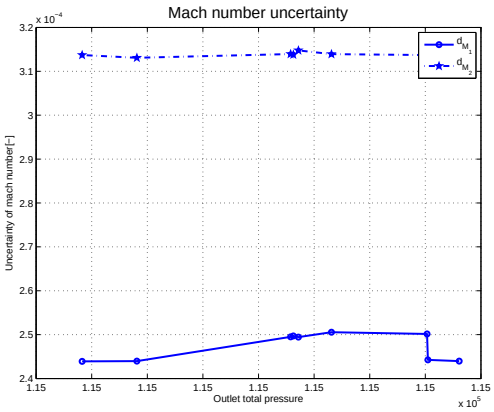

Figure 3.1: Inlet and Outlet mach number uncertainty for different grids.

The sources of the uncertainty values for the measured quantities are other experiments conducted in the same facilities with the same probes. These values represent the overall values for the whole measurement chain; they are reported in Table 3.1, while on the other side, in Table 3.2 are reported the expected uncertainties for the main design variables.

In Figure 3.1 an example is shown of the variation of the uncertainty in function of the outlet total pressure; the points on the curves correspond to different grids, as will be explained afterwards. It can be seen that the outlet Mach number presents a higher value of uncertainty, due mostly to the higher value of uncertainty of the outlet pressure probes.

3.2 Software

The project is developed using the software platform for turbomachinery applications distributed under commercial license by NUMECA International company. The package consists of the following programs:

IGG^{TM} The **I**ntegrated **G**rid **G**enerator is a general meshing utility, rendering

structured hexahedral grids with multiple blocks around 2-D and 3-D geometries using an advanced graphical user interface (GUI).

Autogrid5^{TM} is designed for automatic meshing of all types of machines (axial, radial, mixed-flow configuration) to produce high quality, complex, structured hexahedral grids.

FINE^{TM} /Turbo Flow integrated environment which includes the finite volume flowsolver Euranus. As Autogrid5^{TM}, it works with multigrid levels to increase the convergence speed and stability.

CFView^{TM} Visualization tool.

The post-treatment is performed through the software Matlab by Mathworks®; in order to prepare the data-set for the analysis, some script have been developed, using the python programming language.

3.3 Geometrical model

The study will be conducted on the geometry shown in Figure 3.2. As explained later, from the three-dimensional simulation, the performances will be extracted on a two-dimensional meridional plane, computed as the average along the pitch.

The blade profile is developed by TechSpace Aero . The height of the blade is 10 cm, due to the size of the C3 wind tunnel, used for the experiment. As far as concerns the inlet and the outlet distance from leading and trailing edges, they are taken equal to one chord. As the chord will be changed to assess different values of solidity, the absolute position of the inlet and outlet section of the model will change, as well.

To minimise the mesh size and reduce computation time, a single blade passage is meshed and rotational periodic boundary conditions are imposed. In Figure 3.3 a scheme of the blade to blade section is presented.

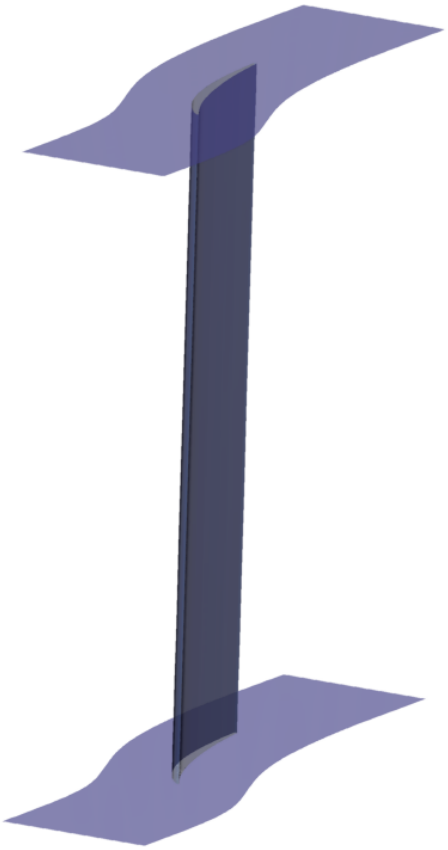

Figure 3.2: Model geometry

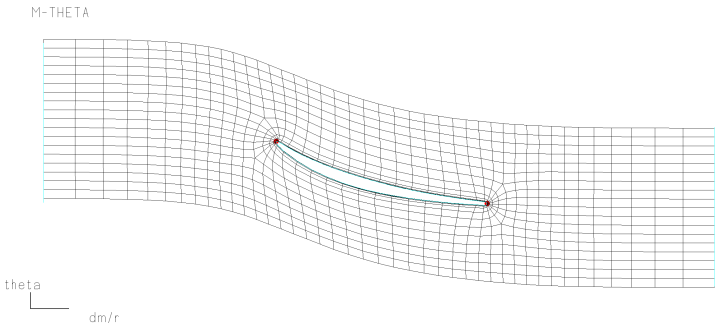

Figure 3.3: Blade to blade section of the model

3.4 Mathematical model

In general the assessment of a fluid-dynamic problem requires to set up a system of equations allowing to balance the main quantities determining the physical phenomena, namely the mass, the momentum and the energy. More hypothesis on the model of the fluid, on the geometry of the domain and the flow characteristics usually lead to the definition of a set of partial differential equations for which analytical solutions are not available. As far as concerns the turbomachinery applications, two different approaches can be usually undertaken: the Euler and the Navier-Stokes models. As they are based on different hypothesis, they can lead to different solutions, usually with a different amount of resource usage. In the present work the Navier-Stokes formulations is used. The main characteristics and hypothesis of the model are shown below.

3.4.1 Navier-Stokes formulation

General equations

Turbomachinery applications typically deal with newtonian fluids, the relation between the shear stress and the strain rate being linear and isotropic through the viscosity μ:

$$\tau_{ij} = \mu \cdot \left[\left(\frac{\partial v_j}{\partial x_i} + \frac{\partial v_i}{\partial x_j} \right) - \frac{2}{3} \left(\vec{\nabla} \cdot \vec{v} \right) \delta_{ij} \right] \tag{3.3}$$

On this assumption is based the Navier-Stokes equation system, below expressed in a general form for a cartesian frame:

$$\frac{d}{dt} \int_\Omega U d\Omega + \int_S \vec{F_I} \cdot d\vec{S} + \int_S \vec{F_V} \cdot d\vec{S} = \int S_T d\Omega \tag{3.4}$$

where U and the source terms vector are defined as follows:

$$U = \begin{bmatrix} \rho \\ \rho v_1 \\ \rho v_2 \\ \rho v_3 \\ \rho E \end{bmatrix} \tag{3.5}$$

$$S_T = \begin{bmatrix} \rho \\ \rho f_{e1} \\ \rho f_{e2} \\ \rho f_{e3} \\ W_f \end{bmatrix} \tag{3.6}$$

and $\vec{F_I}$ and $\vec{F_V}$ are respectively the inviscid and viscous flux vectors:

$$\vec{F_I} = \begin{bmatrix} \rho v_i \\ \rho v_1 v_i + p\delta_{1i} \\ \rho v_2 v_i + p\delta_{2i} \\ \rho v_3 v_i + p\delta_{3i} \\ (\rho E + p) v_i \end{bmatrix} \tag{3.7}$$

$$-\vec{F_V} = \begin{bmatrix} 0 \\ \tau_{1i} \\ \tau_{2i} \\ \tau_{3i} \\ q_i + v_j \tau_{ij} \end{bmatrix} \tag{3.8}$$

The total energy is the sum on the internal energy e and the kinetic energy:

$$E = e + \frac{1}{2} v_i v_i \tag{3.9}$$

while the heat flux component, based on the laminar thermal conductivity κ, is defined by:

$$q_i = \kappa \frac{\partial}{\partial x_i} T \tag{3.10}$$

In theory, the equation 3.4 describes both laminar and turbulent flow. However, in the field of interest of Reynolds number for turbomachinery applications, turbulence is characterized by high non-linear behaviour and by a wide range of spatial and temporal scales, making the Direct Numerical Simulation (DNS) of the Navier-Stokes equations, if not impossible, at least very inconvenient with usual computing power available nowadays. The smallest length of the grid, for instance, should be of the same order of magnitude (or smaller) of the smallest eddy scale length in all the domain, causing a gargantuan increase in the global number of cells and then in the computation duration; a similar idea can be applied to the timespan discretization. In order to solve this problem, a turbulence model is required to predict the effect of the physical phenomenon avoiding the use of prohibitively fine mesh. Two approaches can be adopted: the Large Eddy Simulation (LES) and the Reynolds Average Navier-Stokes (RANS). The first consists in the application of a spacial filter which separates the big scales, solved with the Navier-Stokes equations, and the small scales of the turbulent field. The small turbulent scales are modelled considering them homogeneous and isotropic. The finer the mesh the closer the LES solutions are to the DNS ones, but this technique is still really expensive. The second approach is commonly adopted and is introduced in the next paragraph.

Time averaging of Navier-Stokes equations

The most direct approach to the scale modelling was proposed by Osborne Reynolds himself and consists in the partitioning of the flow field into a mean and a fluctuating part, for instance for the general quantity ψ in the Navier-Stokes equations:

$$\psi = \overline{\psi} + \psi' \tag{3.11}$$

where the time averaged value $\overline{\psi}$ is defined as:

$$\overline{\psi}\left(\vec{x}, t\right) = \frac{1}{T} \int_{-\frac{T}{2}}^{\frac{T}{2}} \psi\left(\vec{x}, t+\tau\right) d\tau \tag{3.12}$$

and then, from this definition: $\overline{\psi'} = 0$. The corresponding density weighted average is defined through:

$$\tilde{\psi} = \frac{\overline{\rho \psi}}{\overline{\rho}} \tag{3.13}$$

with

$$\psi = \tilde{\psi} + \psi'' \tag{3.14}$$

and

$$\overline{\rho\psi''} = 0 \tag{3.15}$$

Density and pressure are time averaged whereas energy, velocity components and temperature are density weighted time averaged. The resulting form of the Navier-Stokes equations is the same as equation 3.4, with:

$$U = \begin{bmatrix} \overline{\rho} \\ \overline{\rho}\tilde{v}_1 \\ \overline{\rho}\rho\tilde{v}_2 \\ \overline{\rho}\rho\tilde{v}_3 \\ \overline{\rho}\tilde{E} \end{bmatrix} \tag{3.16}$$

and

$$\overrightarrow{F_I} = \begin{bmatrix} \overline{\rho}\tilde{v}_i \\ \overline{\rho}\tilde{v}_1\tilde{v}_i + \overline{\rho v_1'' v_i''} + \overline{p}\delta_{1i} \\ \overline{\rho}\tilde{v}_2\tilde{v}_i + \overline{\rho v_2'' v_i''} + \overline{p}\delta_{2i} \\ \overline{\rho}\tilde{v}_3\tilde{v}_3 + \overline{\rho v_3'' v_i''} + \overline{p}\delta_{3i} \\ \left(\overline{\rho}E + p\right) v_i \end{bmatrix} \quad -\overrightarrow{F_V} = \begin{bmatrix} 0 \\ \overline{\tau_{1i}} \\ \overline{\tau_{2i}} \\ \overline{\tau_{3i}} \\ \overline{q_i} + \overline{v_i\tau_{ij}} \end{bmatrix} \tag{3.17}$$

where density averaged total energy is given by:

$$\tilde{E} = \tilde{e} + \frac{1}{2}\tilde{v}_i\tilde{v}_i + k \tag{3.18}$$

k is the turbulent kinetic energy based on the following definition:

$$k = \frac{1}{2}\left(\frac{\overline{\rho v_i'' v_i''}}{\overline{\rho}}\right) \tag{3.19}$$

The averaging procedure introduces two unknown terms: the Reynolds stress tensor and the turbulent heat diffusion. The calculation of these quantities, strictly necessary to solve the whole system, can be achieved through different models using different theoretical hypothesis and unavoidable empirical information. A first-order closure for the Reynolds stress can be attained using the Boussinesq' assumption, considering a linear ratio with the mean strain rate tensor:

$$\overline{\rho v_i'' v_i''} = \mu_t \cdot \left[\left(\frac{\partial\tilde{v}_j}{\partial x_i} + \frac{\partial\tilde{v}_i}{\partial x_j}\right) - \frac{2}{3}\left(\overrightarrow{\nabla}\cdot\overrightarrow{v}\right)\delta_{ij}\right] - \frac{2}{3}\overline{\rho}k\delta_{ij} \tag{3.20}$$

where the new quantity μ_t, named *eddy viscosity* is introduced. As far as concerns the heat diffusion term, a gradient approximation can be used:

$$C_p\overline{\rho v_i'' T} = -\kappa_t\frac{\partial}{\partial x_i}\tilde{T} \tag{3.21}$$

the turbulent thermal conductivity κ_t can be connected to the turbulent eddy-viscosity μ_t through a turbulent Prandtl number Pr_t:

$$Pr_t = \frac{\mu_t C_p}{\kappa_t} \tag{3.22}$$

Using again the same symbology of 3.4, it is possible to evaluate the terms:

$$\vec{F_I} = \begin{bmatrix} \overline{\rho}\tilde{v}_i \\ \overline{\rho}\tilde{v}_1\tilde{v}_i + \overline{\rho v_1'' v_i''} + \overline{p^*}\delta_{1i} \\ \overline{\rho}\tilde{v}_2\tilde{v}_i + \overline{\rho v_2'' v_i''} + \overline{p^*}\delta_{2i} \\ \overline{\rho}\tilde{v}_3\tilde{v}_3 + \overline{\rho v_3'' v_i''} + \overline{p^*}\delta_{3i} \\ \left(\overline{\rho}E + p\right) v_i \end{bmatrix} \quad -\vec{F_V} = \begin{bmatrix} 0 \\ \tau_{1i} \\ \tau_{2i} \\ \tau_{3i} \\ q_i + v_i\tau_{ij} \end{bmatrix} \tag{3.23}$$

where the Reynolds stress and the heat flux components are:

$$\tau_{ij} = \left(\mu + \mu_t\right) \cdot \left[\left(\frac{\partial \tilde{v_j}}{\partial x_i} + \frac{\partial \tilde{v_i}}{\partial x_j}\right) - \frac{2}{3}\left(\vec{\nabla} \cdot \vec{v}\right)\delta_{ij}\right] \tag{3.24}$$

$$q_i = (\kappa + \kappa_t)\,\frac{\partial}{\partial x_i} T \tag{3.25}$$

The quantities μ_t and κ_t need to be solved by the turbulence model (see paragraph 3.8). in contrast to the laminar case, both the static pressure and the total energy contain contribution from the kinetic energy k and are defined as:

$$\overline{p^*} = \overline{p} + \frac{2}{3}\overline{\rho}k \tag{3.26}$$

$$\tilde{E} = \tilde{e} + \frac{1}{2}\tilde{v_i}\tilde{v_j} + k \tag{3.27}$$

3.5 Boundary condition

In Figure 3.4 a scheme of the blade to blade boundary conditions imposed is shown. The types of boundary conditions are chosen on the basis of previous experiences in modelling compressor annular and linear cascades:

3.5.1 Inlet section

Total pressure, total temperature and flow angles are imposed. The value is chosen by an iterative process to set the Mach number as near as possible to a specific value. For every incidence angle five different conditions will be tested changing the Mach number, theoretically in a range between 0.36 and 0.8; however this range is not reachable for every configuration of pitch and chord, as it will be presented afterwards.

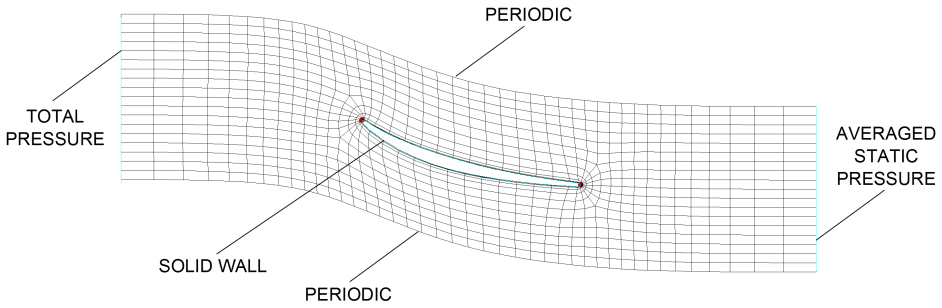

Figure 3.4: Boundary conditions

3.5.2 Outlet section

The averaged static pressure is imposed equal to atmospheric pressure, always ensuring radial equilibrium, as it will be in the experimental test.

3.5.3 Channel sides surfaces

On the sides of the channel the boundary conditions are imposed to match periodicity.

3.5.4 Solid walls: blade

The blade surface is considered adiabatic and no-slip condition is always imposed.

3.5.5 Solid walls: hub and shroud

Two different conditions have been considered for the analysis, whose characteristics are presented below.

Slip condition

This condition assumes the velocity to be tangential to the wall; an extrapolation from the interior field with zero order is performed to obtain the velocity vector on the wall:

$$\overrightarrow{w_w^*} = \overrightarrow{w_1} \tag{3.28}$$

where the subscript w, 1 denote respectively the wall and the first inner cell. The tangential part of the extrapolated velocity vector is:

$$\overrightarrow{w_w^{**}} = \overrightarrow{w_w^*} - \left(\overrightarrow{w_w^*} \cdot \overrightarrow{n}\right) \overrightarrow{n} \tag{3.29}$$

with $\vec{n}$ the normal to the wall. The velocity vector on the wall is finally found by a scaling process such that its module equals:

$$|\vec{w_w}| = |\vec{w_1}| \tag{3.30}$$

The density and the pressure on the walls are set equal to the value calculated in the first cell. This type of boundary condition is called "Euler walls" in the used software; the same nomenclature will be adopted in the present work. Viceversa the no-slip condition presented below will be named "Navier Stokes walls".

No-slip condition

The hub and shroud surfaces are always considered adiabatic; the velocity vector on the wall vanishes. The velocity relative to the wall should be zero, leading to:

$$\vec{w} = -\left(\vec{u_s} - \vec{u_w}\right) \tag{3.31}$$

subscripts s, w referring respectively the system and the wall. A relation for the pressure is obtained by projection of the momentum equation onto the wall normal direction $\vec{n}$. Written in the absolute frame of reference:

$$\vec{n} \cdot \vec{\nabla p} = -\rho \vec{n} \cdot \left(\vec{v} \cdot \vec{\nabla}\right) \vec{v} + \vec{n} \cdot \vec{n} \cdot \left(\vec{\nabla} \cdot \tau\right) \tag{3.32}$$

the normal pressure gradient can be written as a function of pressure derivatives along the coordinate lines:

$$\vec{n} \cdot \vec{\nabla p} = \frac{1}{|\vec{S_j}|\Omega} \left[\vec{S_j} \cdot \vec{S_i} \frac{\partial p}{\partial \xi} + \vec{S_j} \cdot \vec{S_j} \frac{\partial p}{\partial \eta} + \vec{S_j} \cdot \vec{S_k} \frac{\partial p}{\partial \zeta} \right] \tag{3.33}$$

where ξ, η, ζ represent the coordinates in the i,j,k directions, j direction assumed directed away from the wall (not necessarily perpendicular to it). $\vec{S}_{i,j,k}$ are the surface vectors of the corresponding cell faces. Combining equations 3.32 and 3.33 and considering the velocity vanishing on the wall, yields:

$$\frac{\partial p}{\partial \eta} = \underbrace{-1 \frac{1}{|\vec{S_j}|^2} \left[\vec{S_j} \cdot \vec{S_i} \frac{\partial p}{\partial \xi} + \vec{S_j} \cdot \vec{S_k} \frac{\partial p}{\partial \zeta} \right]}_{\lambda_1} + \underbrace{\frac{\Omega \rho}{|\vec{S_j}|} \vec{n} \cdot \left(\vec{v} \cdot \vec{\nabla}\right) \vec{v}}_{\lambda_2} + \underbrace{\frac{\Omega}{|\vec{S_j}|} \vec{n} \cdot \left(\vec{\nabla} \cdot \tau\right)}_{\lambda_3} \tag{3.34}$$

The λ_3 term is only considered while using normal momentum equation to describe the pressure derivative. If the normal pressure gradient is assumed equal to zero, as for the present analysis, only λ_1 and λ_2 are taken into account; this last term can be expressed as follows:

$$\lambda_2 = \frac{\Omega \rho}{|\vec{S_j}|^2} \vec{S_j} \cdot \vec{r}\, \omega_w^2 \tag{3.35}$$

taking into account that the appearing velocity is the velocity on the wall, which vanishes for a stator. Once the derivative of the pressure is determined, assuming the direction points inside the interior field, the pressure on the wall is obtained as:

$$p_w = p_1 - \frac{\partial p}{2\partial \eta} \tag{3.36}$$

The temperature on the wall is obtained expressing the vanishing of the normal temperature gradient, i.e. in terms of derivatives along the coordinate lines:

$$\frac{\partial T}{\partial \eta} = -\frac{1}{|\overrightarrow{S_j}|^2}\left[\overrightarrow{S_j}\cdot\overrightarrow{S_i}\frac{\partial T}{\partial \xi} + \overrightarrow{S_j}\cdot\overrightarrow{S_k}\frac{\partial T}{\partial \zeta}\right] \tag{3.37}$$

The wall temperature is then found using an equation analogous to 3.36. From pressure and temperature is then computed the density, according to the fluid characteristics.

3.6 Numerical scheme

Spatial discretization

The discretization in space is based on a cell centered control volume approach. The general Navier-Stokes equation 3.4 is discretised as:

$$\frac{d}{dt}\int_\Omega U d\Omega + \sum_{faces}\overrightarrow{F_I}\cdot\Delta\overrightarrow{S} + \sum_{faces}\overrightarrow{F_V}\cdot\Delta\overrightarrow{S} = \int_\Omega S_T d\Omega \tag{3.38}$$

where $\overrightarrow{F_I}\cdot\Delta\overrightarrow{S}$ and $\overrightarrow{F_V}\cdot\Delta\overrightarrow{S}$ are respectively the inviscid and viscous fluxes. These last ones are determined in a purely central way; they contain gradients which must be evaluated on the cell faces, applying the Gauss' theorem:

$$\overrightarrow{\nabla}\Phi = \frac{1}{\Omega}\int\overrightarrow{\nabla}\Phi d\Omega = \frac{1}{\Omega}\int\Phi d\overrightarrow{S} \tag{3.39}$$

The gradients are calculated directly on the cell faces; the gradient on face i+1/2 and j+1/2 can be computed through the control volumes illustrated in Figure 3.5. Even if this methods requires an higher computational effort in respect to the computation of the gradients in the cell corners (due to the higher number of faces compared to the number of corners), it is preferred due to its robustness. The inviscid fluxes are upwind based fluxes and therefore noted with a $*$ superscript. The inviscid numerical flux is expressed as follows:

$$\left(\overrightarrow{F}\,\overrightarrow{n}\right)^*_{i+1/2} = \frac{1}{2}\left[\left(\overrightarrow{F}\,\overrightarrow{n}\right)_i + \left(\overrightarrow{F}\,\overrightarrow{n}\right)_{i+1}\right] - d_{1+1/2} \tag{3.40}$$

while the first term in the right end side correspond to a purely central evaluation of the flux, the term $d_{1+1/2}$ represents a numerical dissipation associated with upwind schemes. In equation 3.40 an averaging technique is used; when a

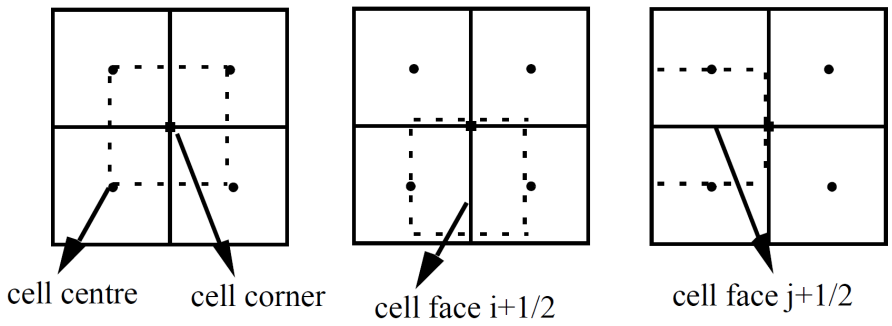

Figure 3.5: Different control volume used to calculate gradients in cell corners or cell faces

central scheme is used, however, an alternative formulation, in which the flux is computed as based on the averaged unknown, is preferred because it is more robust specially for high speed flows:

$$\left(\vec{F}\,\vec{n}\right)^{*}_{i+1/2} = \vec{F}\,\vec{n}\left(\frac{U_i + U_{i+1}}{2}\right) - d_{1+1/2} \tag{3.41}$$

Central scheme

A Jameson type dissipation is used with 2nd and 4th derivatives of the conservative variables:

$$d_{1+1/2} = \varepsilon^{(2)}_{i+1/2}\,\delta\, U_{i+1/2} + \varepsilon^{(4)}_{i+1/2}\,\delta^3\, U_{i+1} \tag{3.42}$$

the scalar coefficients ε are given by:

$$\varepsilon^{(2)}_{i+1/2} = \frac{1}{2}\kappa^{(2)}\lambda^{*}\max\left(\nu_{i-1},\nu_i,\nu_{i+1},\nu_{i+2}\right) \tag{3.43}$$

$$\varepsilon^{(4)}_{i+1/2} = \max\left(0, \frac{1}{2}\kappa^{(4)}\lambda^{*} - \varepsilon^{(2)}_{i+1/2}\right) \tag{3.44}$$

The cell centered value of $\varepsilon^{(4)}$ are obtained as arithmetic average of the cell face values. The variables ν_i are sensors to activate the second difference dissipation in regions of strong gradients, such as shocks. They are based on the pressure and temperature variations. λ^{*} is a measure of the inviscid fluxes and is commonly chosen as the spectral radius multiplied with the cell face area:

$$\lambda^{*} = \lambda^{*}_{i+1/2} = \left(\vec{v}\cdot\Delta\vec{S} + c\Delta S\right)_{i+1/2} \tag{3.45}$$

3.7 Mesh

As mentioned in paragraph 3.4, for the applications of engineering interest, the Partial Differential Equations (PDE) governing the fluid behaviour are not usually amenable to closed-form solutions and then the problem must be analysed trough numerical methods, typically finite elements, finite differences and finite volumes (implemented in FINE^{TM} solver). These approaches require a discretization both in the equations and in the flow domain. The control volume is split into smaller sub-domains, called *elements* or *cells*, usually characterized by a simple geometry: for three-dimensional simulations are commonly adopted tetrahedra and hexaedra, this last one being used in the present model. The set of all cells (or elements) is named grid or mesh and its proper generation have always represented an essential issue in the modelling process. The characteristics and the quality of the mesh have a great influence not only on the results and on the efficiency of the calculation, but also on the convergence of the model itself, as, for instance, influences the behaviour of the turbulence model. It is usually important, then, to understand the effects of the different parameters of the grid on the final results and on the resources consumption, increasing the overall number of cells, for example, could not be always effective on the final results, while requiring a substantial increase of the computational effort. To assess these information, a sensitivity analysis is performed on the given control volume, and it is fully presented in the next paragraph; in the following section, the final grid is presented with regard to the reasons of the choices.

3.7.1 Sensitivity analysis model

The program Autogrid5^{TM} usually performs an automatic meshing of the domain, with a default general-purpose parameter set. However these parameters can be changed to fulfil the specific goals of different applications. Pertaining to the influence of solidity, the effects of the following parameters have been investigated as they are expected to play an important role in the cascade behaviour:

- global number of cells
- spanwise discretization
- discretization on the blade to blade surface
- minimum dimension of the cell next to the hub and shroud of the channel
- minimum dimension of the cell next to the blade surface

To investigate the effects of these parameters, fifteen different grids have been developed and investigated; their characteristics are reported in 3.5. The results will be presented after the description of the model:

Quantity	Symbol	Value	Unit
pitch	s	0.02400	m
chord	c	0.03309	m
Blade height	h	0.1	m
Inlet distance from leading edge	$1 \cdot c$	0.003309	m
Outlet distance from trailing edge	$1 \cdot c$	0.003309	m

Table 3.3: Geometrical size of the blade used in the mesh analysis

Geometrical features For consistency reasons, the model used for the sensitivity analysis is the same presented in 3.3 ; as far as concerns the geometrical size, the baseline considered is presented in Table 3.3.

Turbulence models In this part of the work, two different turbulence models have been used, due to their different characteristics (see sec. 3.8)and the implementation in the solver. FINE^{TM} perform the analysis with the turbulence model defined by the users just for the last level, while using the Baldwin-Lomax scheme on all the previous ones; as this simple model does not permit to evaluate the effect of turbulence intensity, even if not really accurate, it guarantees a fast and regular solution process. Due to these characteristics, the first analysis of the grids has been performed imposing this scheme for all the levels, allowing to increase the comparability of two different meshes. Afterwards, in order to match the level of precision of the final investigation, the performances have been studied using the Yang Shih model.

Equation formulation The Navier-Stokes equation formulation has been used for the mesh analysis, to fulfil a proper description of the phenomena without neglecting the effects of viscosity.

Boundary condition The same boundary conditions of the main analysis have been imposed and they will be presented in sec. 3.5. In the inlet section absolute total pressure has been imposed, while in the outlet one an averaged static pressure is considered. As far as concerns the solid walls of the domain, two situations have been analysed, imposing slip and no-slip condition.

3.7.2 Mesh quality assessment

A quantitative evaluation is performed based on different aspects and in relation with the computation time:

- geometrical characteristics of the mesh

- impact on the performances

As far as concerns the geometrical characteristics of the mesh, the mesh quality report has been considered and evaluated on the basis of both the NUMECA indications reported in [29] and the experience gained by the work-team. Four parameters are considered for this kind of analysis:

- ✓ **Number of levels**: in relation to the multigrid approach used by the software, this number should be as high as possible to guarantee a fast convergence and a good stability. This number depends on the discretization of the spanwise and on the blade to blade topology. Usually good results are achieved with three grid levels.
- ✓ **Minimum skewness**: it is an index of the orthogonality of the grid; its value should be kept down as much as possible. 50° could be considered a threshold.
- ✓ **Maximum aspect ratio**: represents the ratio between the different dimension of the cells; even though this value should be maintained as low as possible, the limit proposed by NUMECA does not find a practical confirmation.
- ✓ **Maximum expansion ratio**: this index represents the ratio between the volume of the smallest and the biggest cell of the model. Both theory and practice suggest that this parameter is very important assessing the quality of the grid and then should not exceed the value of 1.8. This threshold represents a severe constraint while trying to keep a small cell size near to the walls to have a good resolution of the boundary layer and, at the same time, a small global number of cells to reduce the need of resources.

As far as concerns the performances, according to section 3.1, the effects of the changed parameters have been studied through the quantities to be measured in the future tests (Absolute total pressure, Static pressure, total temperature, flow angles) and the ones strictly related to them and significant for the study (mass-flow, pressure ratio, mach number, coefficient of loss). As reported in Table 3.4, two different kinds of performances are analysed:

Global Performances - An averaged value is considered; for mass-flow, static pressure, Mach number, flow angles the scalar value is simply integrated on the section, while total pressure is mass-weighted averaged.

Local Performances - The mass-averaged value along the pitch is extracted. Even though the span-wise profile of the different quantities allows to better enlighten the behaviour of the flow depending on the different tested characteristics, only the value at midspan will be considered, according to the approach, imposed by the TechSpace Aero , to map the operative range of the cascade.

Group	Quantity	Numerical assessment
Global performances	Massflow	scalar integral
	Pressure ratio	mass-weighted integral
	Static pressure	scalar integral
	Mach number	scalar integral
	Outlet flow angle	scalar integral
	Coefficient of loss	based on integral quantities
Local performances	Absolute total pressure	value at midspan
	Pressure ratio	value at midspan
	Static pressure	value at midspan
	Mach number	value at midspan
	Outlet flow angle	value at midspan
	Coefficient of loss	based on local quantities

Table 3.4: Quantity evaluated for the mesh quality assessment

3.7.3 Results

Convergence

the numerical scheme consists in a Jameson centered scheme for the spatial discretization coupled with a 4^{th} order Runge-Kutta for the time discretization; the Courant-Friedrichs-Lewy number set to 3 for all the computation. The study of the convergence has been performed in order to guarantee the comparability of the results; the effect on the convergence of the parameters of the mesh is not considered important for the goals of the present work and has not been studied. A limit in the maximum number of iterations has been chosen. An unrealistic value of 10^{-16} has been put as threshold for the residual arrest criterion, to avoid an untimely stop of the computation. The convergence assessment has been performed through two different quantities, the mass flow and the residuals of the density. In Figure 3.6, for instance, the complete history of mass flow convergence for mesh B using the Baldwin Lomax turbulence model is shown; all the computations present similar behaviour; the difference between inlet and outlet never exceeds $10^{-5}\, kg/s$, but is usually far lower. A slight difference in the steady mass flow can be found between the Euler and the Navier-Stokes walls results, the same for the different meshes. This difference is related to the presence of the boundary layer on the end-walls

Name	Number of grid points	Flow paths	Hub and Shroud cell width	Blade cell width	N. of levels	Min. Skewness	Max. AR	Max ER	Max ER (span-wise)
A	334983	33	0.01	0.01	4	46.768	1926.7	1.6591	1.6591
B	599775	33	0.01	0.01	3	51.046	1965.2	1.6591	1.6591
C	659815	65	0.01	0.01	4	46.768	700.74	1.5649	1.255
D	334983	33	0.01	0.001	4	44.003	19214	2.7285	1.6591
E	289707	33	0.001	0.01	3	43.343	2376.9	1.9617	1.9617
F	1181375	65	0.01	0.01	3	53.962	714.76	1.3301	1.255
G	1306695	65	0.01	0.001	3	51.342	7062.5	1.5133	1.255
H	1181375	65	0.001	0.01	3	51.046	1200.8	1.3675	1.367
I	779355	45	0.001	0.001	3	48.233	13430	1.6103	1.61
J	1161071	53	0.001	0.001	2	43.838	12038	1.5106	1.48
K	1755455	65	0.001	0.001	3	47.932	8603	1.5004	1.367
L	782403	41	0.001	0.001	3	47.54	14339	17036	1.704
M	1245727	49	0.001	0.001	4	50.8	12755	1.53	1.53
N	1237071	57	0.001	0.001	3	48.49	12755	1.51	1.43
O	1151255	49	0.001	0.001	4	52.52	12668	1.5379	1.538

Table 3.5: Characteristics of tested mesh

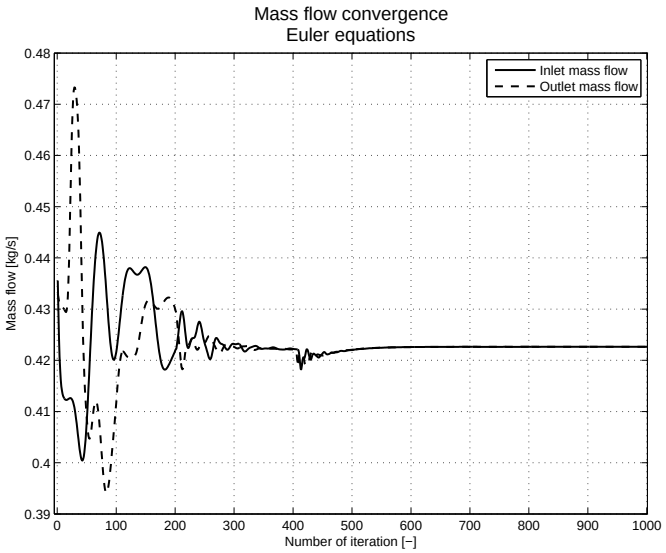

Figure 3.6: Mass flow convergence for mesh I, Euler walls

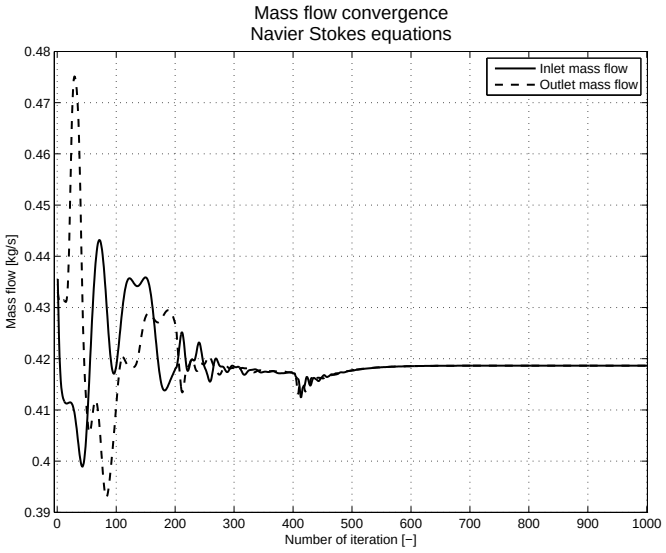

Figure 3.7: Mass flow convergence for mesh I, Navier-Stokes walls

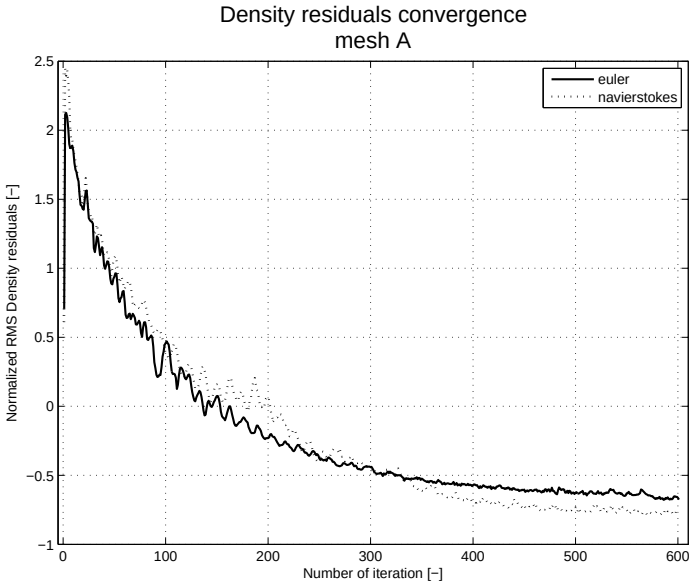

Figure 3.8: Convergence analysis on RMS density residuals for mesh I

The residuals are computed by FINE^{TM} /Turbo solver as a flux balance on all the surfaces of each cell;

$$RES = \sum \left(fluxes \right) \tag{3.46}$$

For the analysis, the root mean square of the density residuals has been considered, normalized with respect to the value at the first iteration:

$$\widehat{RMS}_{RES} = \log\left(RMS\left(\frac{RES}{Cell\ volume} \right) \right) \tag{3.47}$$

$$RMS_{RES,i} = \widehat{RMS}_{RES,i} - \widehat{RMS}_{RES,1^{st}it.} \tag{3.48}$$

In Figure 3.8 and 3.9 a comparison between the convergence for different equation set is presented, considering the iterations on the last grid level. Even though the behaviour between the different meshes appears to be quite different, presenting different oscillation and trends, some patterns can be found as the Navier-Stokes model presents a slower convergence to lower residual values for all the grids; even the order of magnitude of the oscillations is usually the same but the wave length is different.

Performance

Effect of the wall minimum cell size: The minimum cell size has an important influence on the model behaviour since it influences the accuracy in

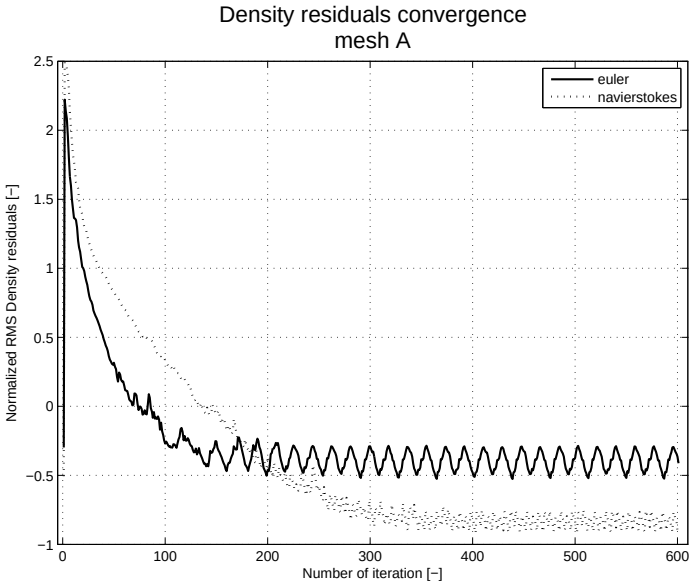

Figure 3.9: Convergence analysis on RMS density residuals for mesh A

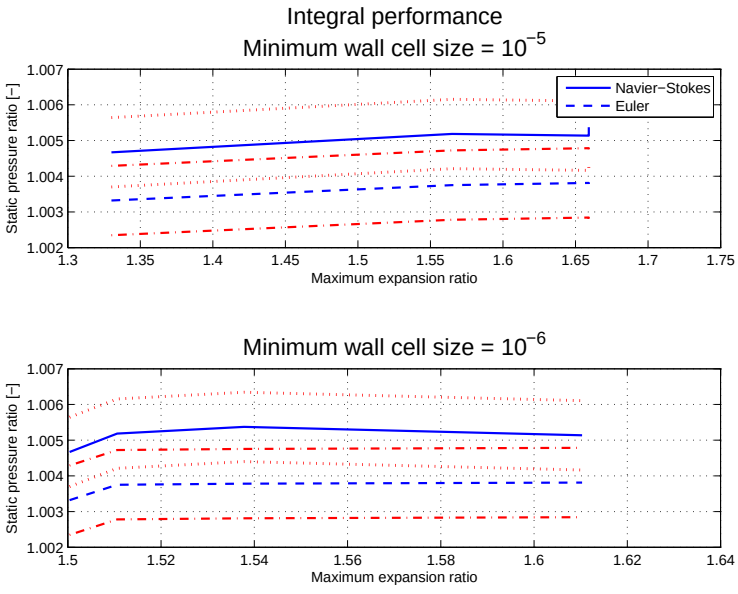

Figure 3.10: Integral static pressure ratio versus maximum expansion ratio for different value of minimum cell size

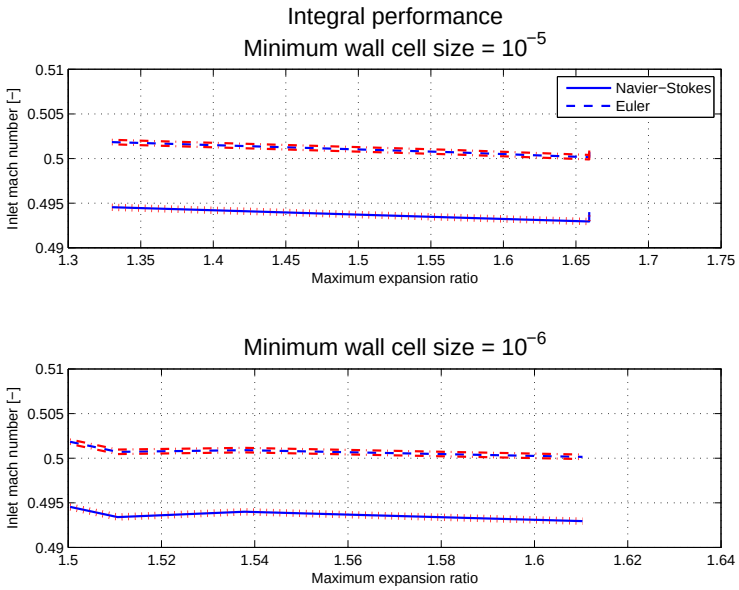

Figure 3.11: Integral inlet mach number versus maximum expansion ratio for different value of minimum cell size

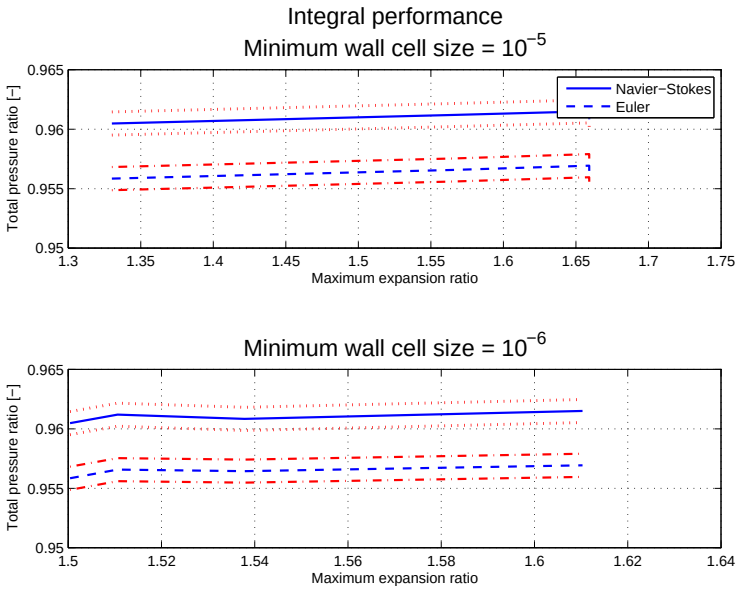

Figure 3.12: Integral total pressure ratio versus maximum expansion ratio for different value of minimum cell size

the description of the boundary layer, which usually is a very delicate part of the model. The turbulence model as well, is affected by this quantity since it determines the values of y^+, which plays a very important role in the closure of the equations. During the analysis, different values for this parameter have been imposed on the different boundaries of the domain (the blade and the hub and shroud surfaces), through the grids indicated as D,E,G,H; the values of 10^{-5} and 10^{-6} have been chosen matching the hints of the FINE^{TM} manuals with the previous experience. Unfortunately it was not possible to find a pattern or trend in the results as the change on the different surface probably influences in indirect ways various physical phenomena, as the vein contraction through the channel and the pressure and velocity gradients on the blades. These effects likely affect the span-wise distribution of the local and integral performances.

To perform the rest of the analysis, the grids mentioned before have not been considered and the minimum cell size has been set at the same value for the two different types of surfaces, to assess the influence of the other parameters.

Considering the global performances, for instance, in Figure 3.10, 3.11 and 3.12, some comparisons between the different grids(respectively A,B,C,F and I,J,K,O) are presented, plotted in function of the Maximum Expansion Ratio (MER). Even if a full relative estimation is impossible due to the different ranges of abscissae, it is still possible to enlighten a similar behaviour between the two groups, asymptotic towards the lower MERs . The red lines represent the uncertainty range of the experimental measurements; the difference between slip and no-slip condition is usually outstanding, while for many quantities the increase in the number of cells does not drive to a measurable improvement of the accuracy.

A comparison between the local performance, permits to enlighten better the role of this parameter; in Figure 3.13, 3.14 and 3.15, for instance, the same quantities used for the integral comparison are plotted; the curves present a real asymptotic behaviour, and even with the same previous comparability issue, the trend of the curves looks similar for the different simulations. One can also notice that the difference between the Euler and the Navier-Stokes walls performances are smaller than for integral performance.

If all conditions are equal, the effect of a change in the minimum cell size is mainly a different expansion ratio of the cells in the direction normal to the surfaces; a decrease in this parameter determines more irregularity in the dimension of the cells without any significant effect on the local performances; then for the final model, as the choice of the minimum cell size doesn't appear to affect significantly the computation cost, the lower value has been chosen.

Effect of the span-wise discretization In Figure 3.16 two different span-wise discretization are represented. This parameter has been controlled through two different quantities, the flow-path number, namely the number of times the blade to blade mesh is repeated and the percentage of mid-flow cells, which

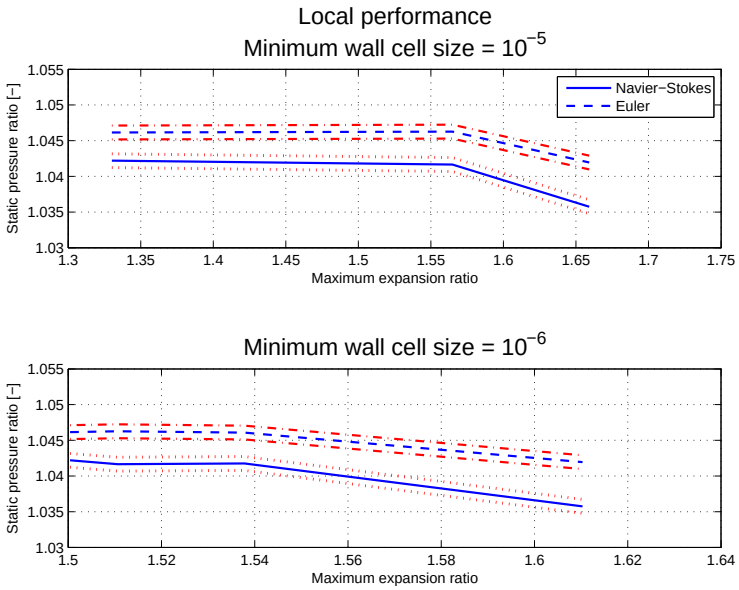

Figure 3.13: Local static pressure ratio versus maximum expansion ratio for different value of minimum cell size

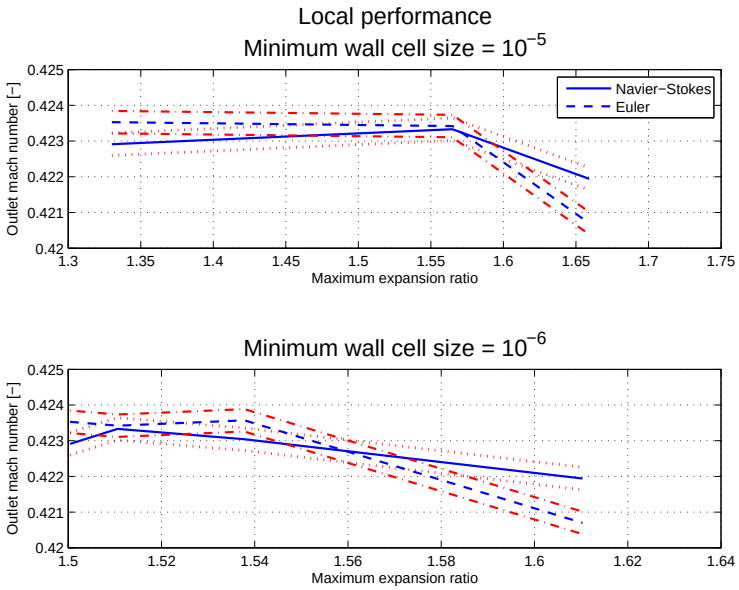

Figure 3.14: Local outlet mach number versus maximum expansion ratio for different value of minimum cell size

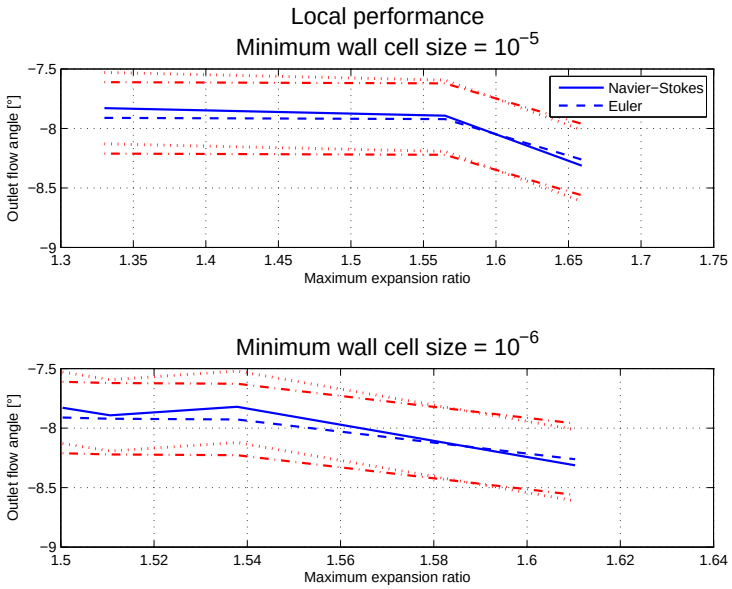

Figure 3.15: Local α_2 versus maximum expansion ratio for different value of minimum cell size

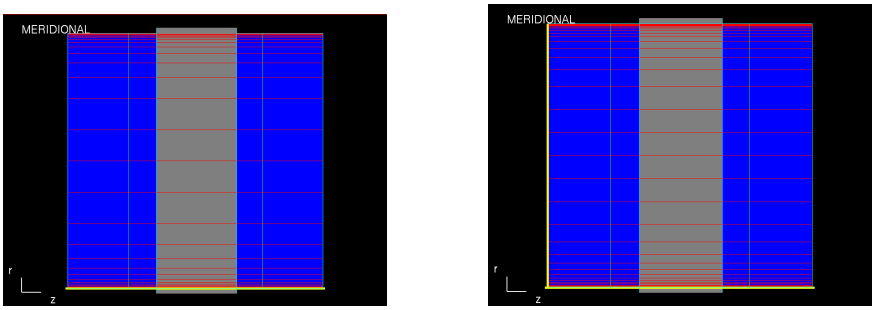

(a) mesh J (b) mesh K

Figure 3.16: Examples of different span-wise discretization

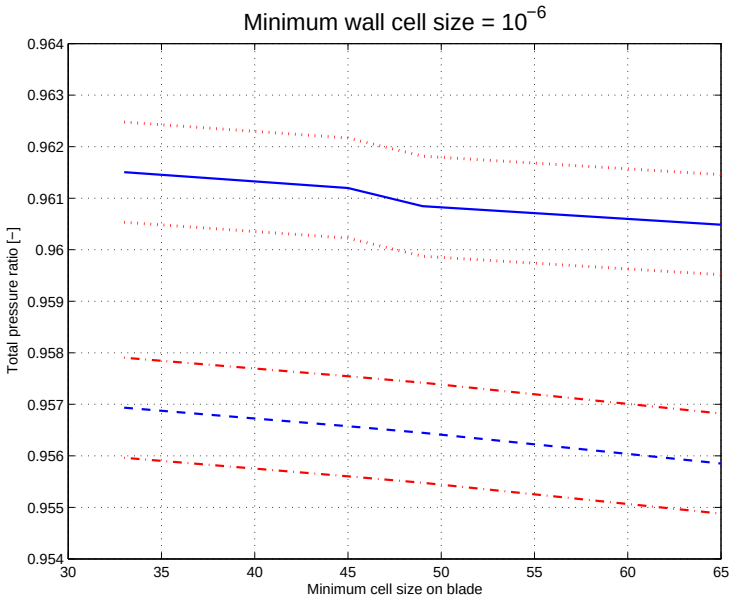

Figure 3.17: Integral total pressure ratio versus flow-path number

controls the distribution along the span-wise of the different "cutting" planes. As presented in Table 3.5, the first values has been changed in a range between 33 and 65, with special attention in the selection of the values, as this parameter strongly influences the number of grid levels, and so the quality of convergence. The percentage of mid-flow cells has been set to 10% and has not been changed; this choice imposes a slight constraint to the maximum expansion ratio along the span-wise and allows, at the same time, to have a good discretization near to the hub and shroud surfaces, as required for a good description of the boundary layer development on them. In Figure 3.17 and 3.18 the integral total pressure ratio and inlet mach number can be analysed; a slight asymptotic behaviour can be recognized from the values around 45.

Looking at the local performances, reported in Figure 3.19, 3.20 and 3.21, a clear asymptotic behaviour can be seen, starting from the value of 45. As the flow-path number has a strong influence on the computation cost because of its linear dependence with the global number of cells, it must be kept as low as possible. For this reason the value of 45 has been taken for the final grid.

Blade to blade surface discretization Three blade meshing topologies are available to generate grids for turbomachinery components, namely the default (O4H), HOH and HandI topologies. The O4H topology is aimed at fully automatic meshing for all kinds of turbomachinery, while the HOH and HandI topologies produce high quality grids but are not suitable for all applications ([29]); for this

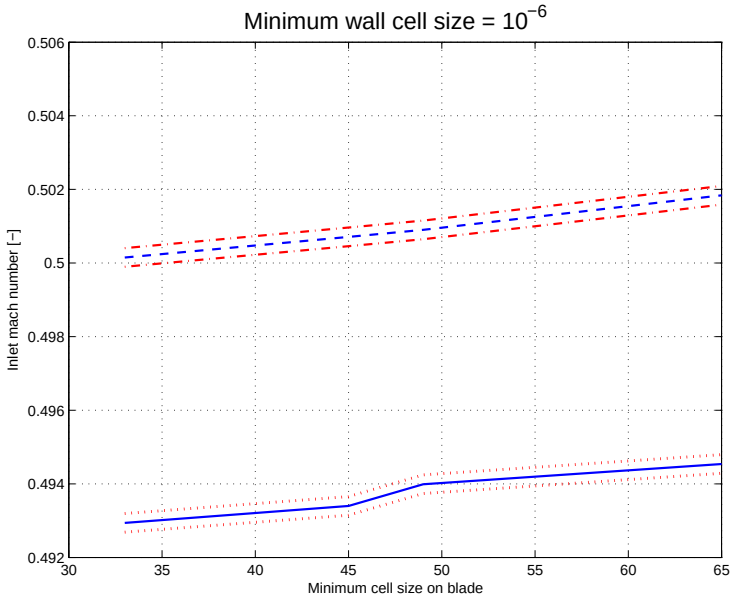

Figure 3.18: Integral inlet mach number versus flow-path number

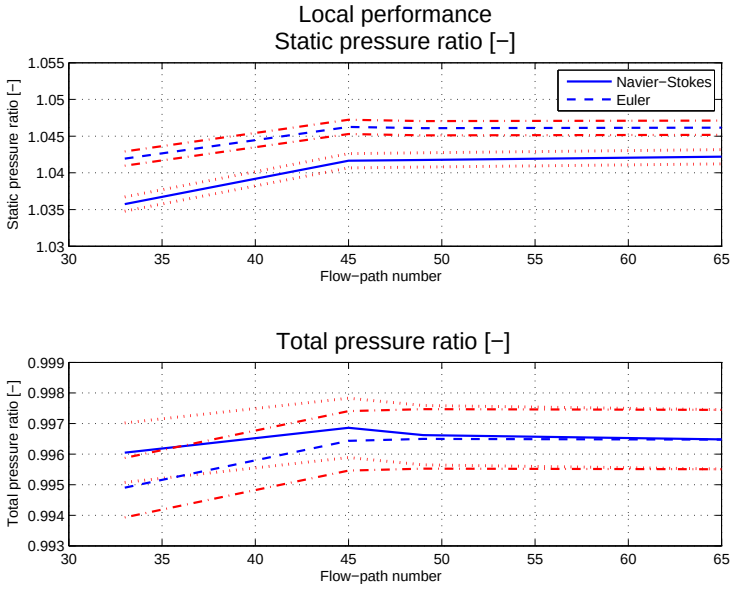

Figure 3.19: Local static and total pressure ratios versus flow path number

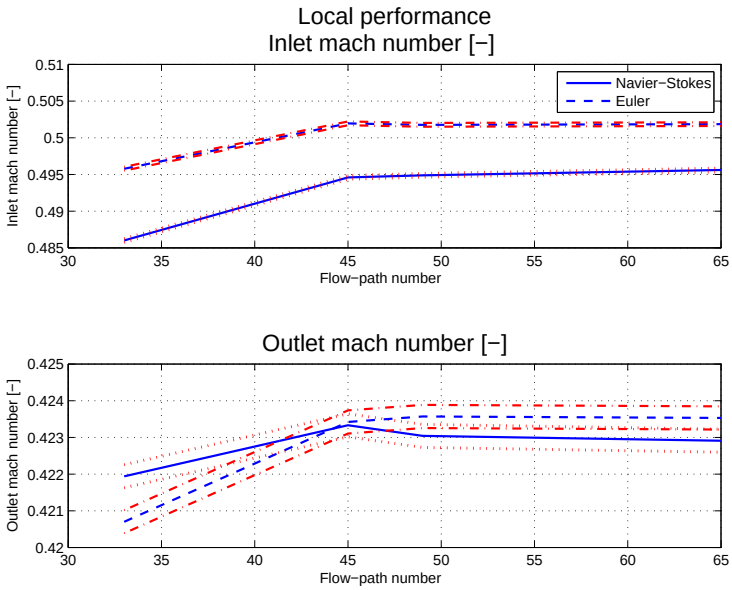

Figure 3.20: Local inlet and outlet mach numbers versus flow path number

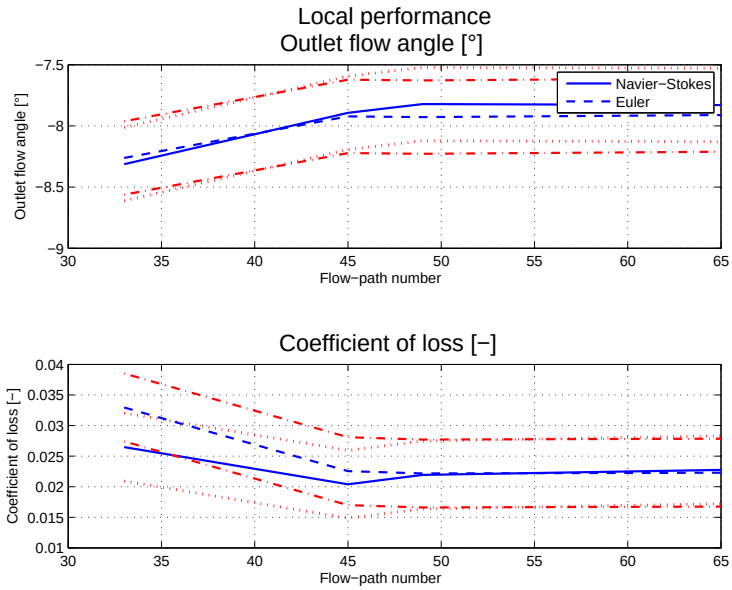

Figure 3.21: Local α_2 and Ω versus flow path number

reason the default O4H topology has been chosen; a sketch of this scheme is presented, as an example, in Figure 3.22. The numbers indicate the number of

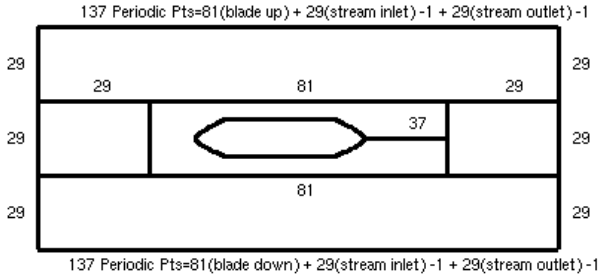

Figure 3.22: Topology for mesh J

partition of each interval. In the present work the influence of the partition of each single zone has not been studied, even if a special attention has been paid in the descriptions of the central square and the tail.

A direct attempt has been made to assess the influence of the blade to blade surface discretization, however due to the strong influence on the number of grid levels the blade to blade topology can unlikely be changed without affecting the convergence and then the comparability itself of the results. An indirect analysis can be performed considering the effect of the global number of cells, reported in the following paragraph.

Global number of cells This parameter indeed influences the computation cost through a relation more than proportional and, as well, the reliability of the model, unfortunately in a way far less than proportional.

The effect of the number of cells on the integral performances could be presented, for instance, through the plots in Figure 3.23 and 3.24. While both the pressure ratios and the loss coefficient present a similar behaviour, constant till the value of one million cells and then decreasing, the mach numbers present a positive constant slope.

As far as concerns the local performance a clear asymptotic behaviour starting from a global number of cell around 800000; for this reason, this threshold value has been chosen for the final grid;

3.7.4 Final grid

The final grid chosen for the assessment is named "I" in Table 3.5; it represents the best trade off between performances and costs of the computation. The topology is presented in Figure 3.28, while the convergence history of the

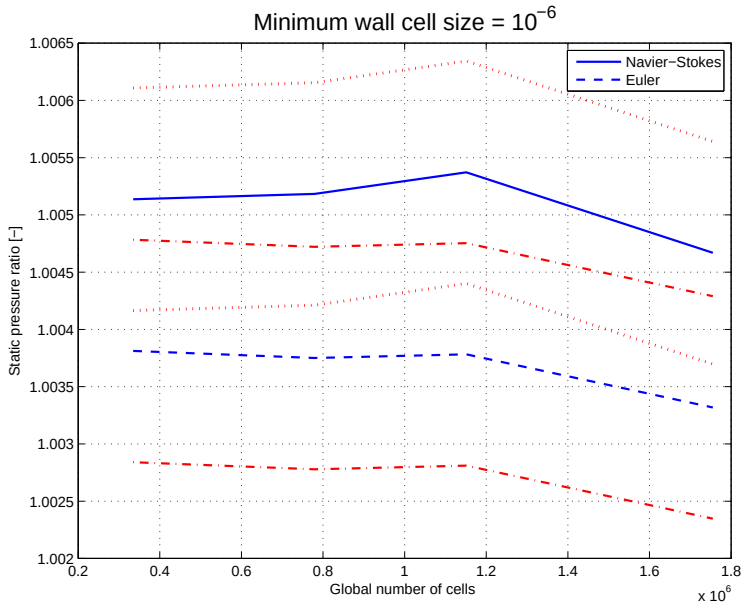

Figure 3.23: Integral static pressure ratio versus number of cells

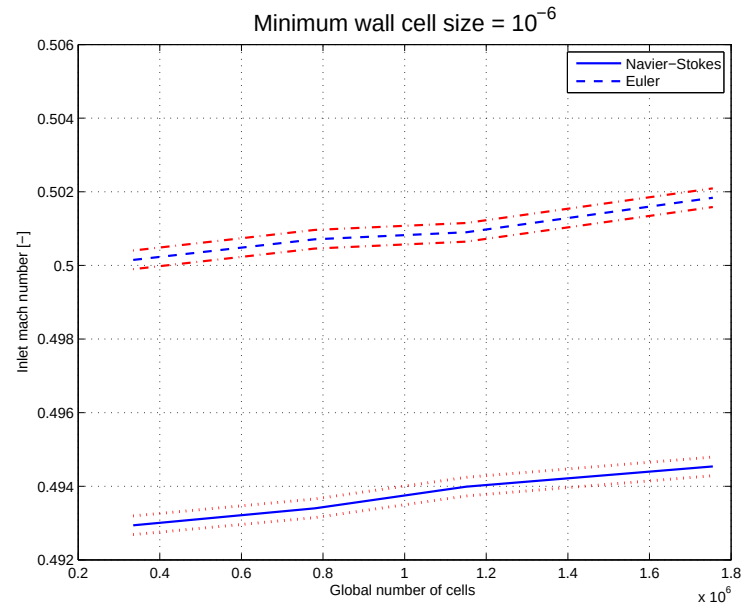

Figure 3.24: Integral inlet mach number versus number of cells

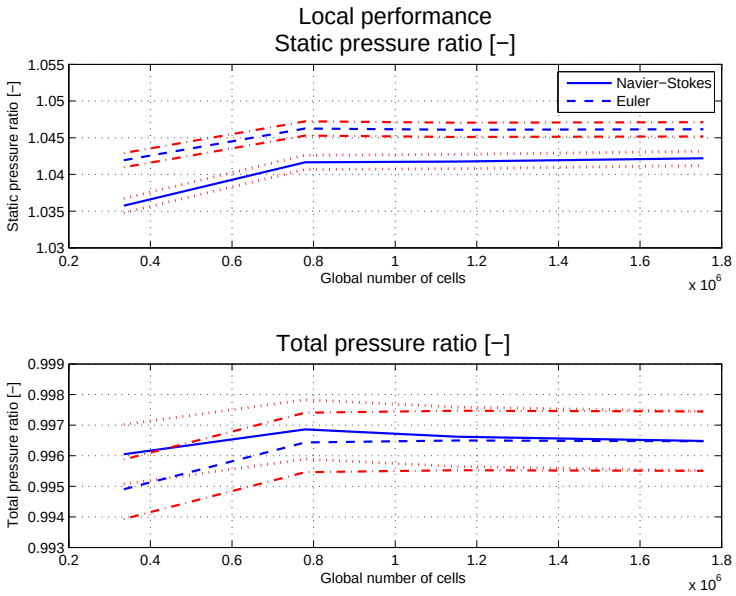

Figure 3.25: Local static and total pressure ratios versus number of cells

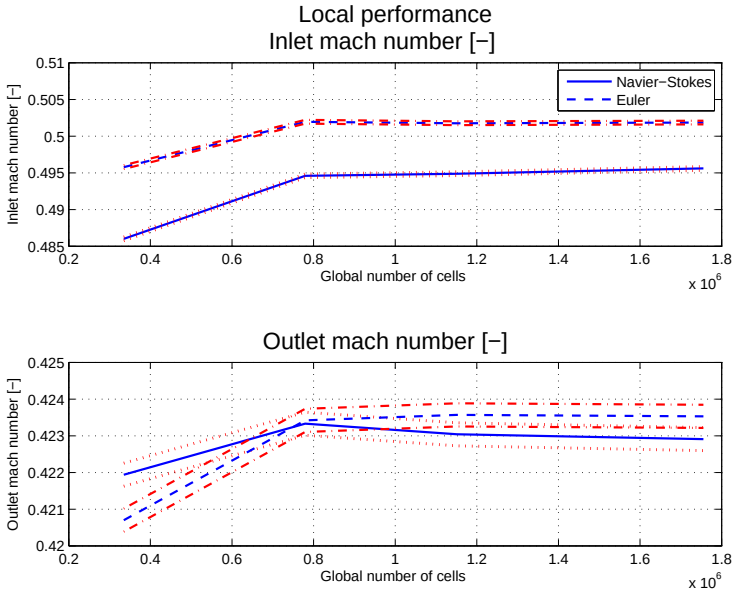

Figure 3.26: Local inlet and outlet mach numbers versus number of cells

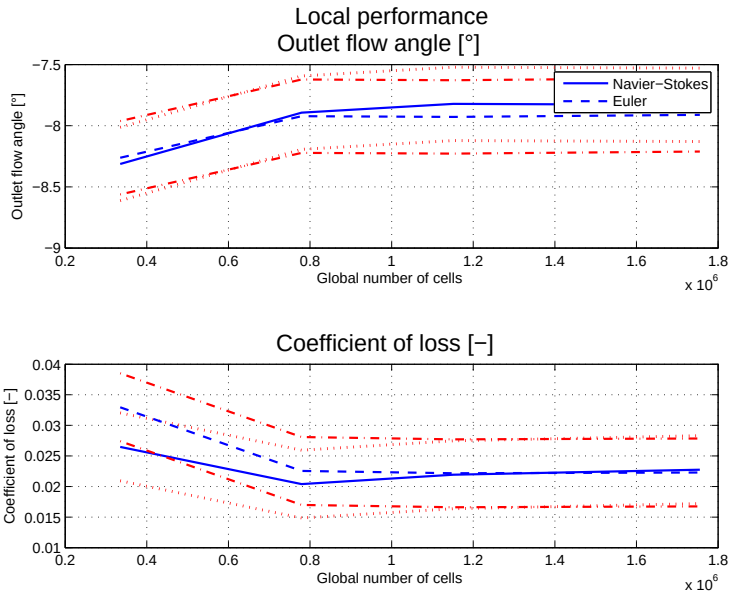

Figure 3.27: Local α_2 and Ω versus global number of cells

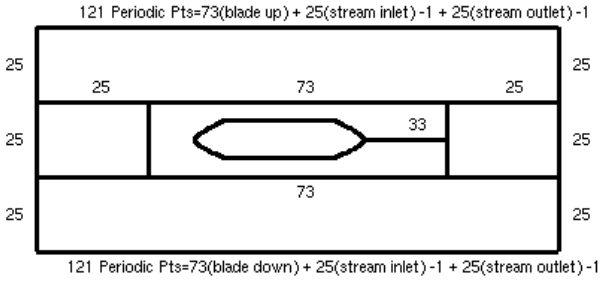

Figure 3.28: Topology for mesh I

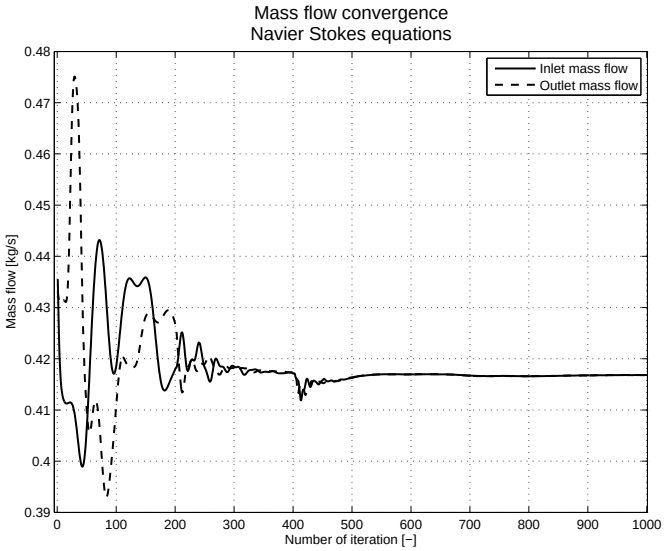

Figure 3.29: Mass flow convergence for mesh I, Navier-Stokes equations, Yang-Shih turbulence model

Navier-Stokes simulation with the Yang-Shih turbulence model is presented in Figure 3.29 and 3.30.

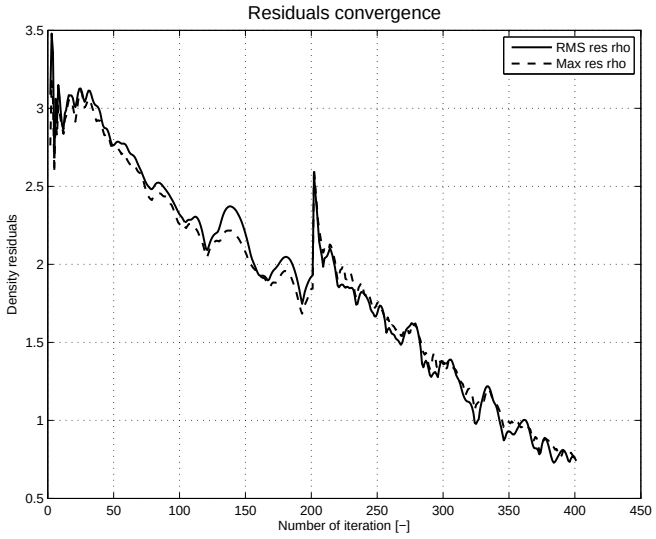

Figure 3.30: Density residuals convergence for mesh I, Navier-Stokes equations, Yang-Shih turbulence model

3.8 Turbulence modelling

In paragraph 3.4.1 the need of an additional "tool" to model and solve the further unknown quantities introduced by the time averaging of the Navier-Stokes equations was presented. It is clear, then, that the turbulence model represents a critical issue while performing a numerical investigation, as it influences the convergence, the accuracy of the results and the computation cost. In this frame it is of some interest the assessment of the behaviour of the model with respect to different turbulence models and different turbulence settings concerning mostly the turbulence intensity. As a matter of fact, regarding this quantity, the behaviour of the model for the main analysis is required as independent as possible. The study of the turbulence modelling influence has been attempted through five different models:

- ✓ Baldwin Lomax
- ✓ Spalart Allmaras
- ✓ Yang Shih
- ✓ Shear Stress Transport
- ✗ Launder Sharma

Unfortunately it was not possible to run all the simulations successfully with the Launder Sharma (LS) model due to the lack of experience in the use of this

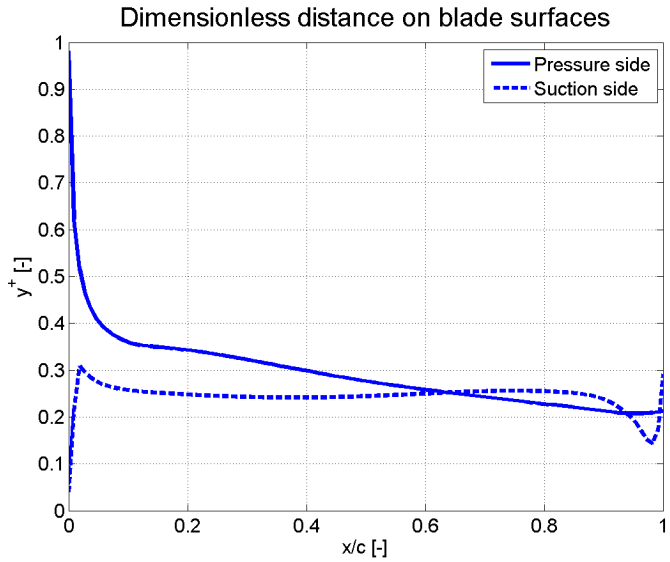

Figure 3.31: y^+ behaviour on pressure and suction side of the blade for turbulence intensity equal to 1% for the Shear Stress Transport model

scheme and its strong sensitivity to the initial condition. This model appeared to be very sensitive to the turbulence intensity allowing to run just one simulation with the lowest value of this parameter. After a presentation of the dimensionless wall distance (y^+) parameter, which plays an important role for the turbulence description, a short review of the used models and the respective settings will be presented, followed by the results of the analysis will be presented.

3.8.1 Dimensionless wall distance y^+

A non-dimensional wall distance for a wall-bounded flow can be defined in the following way:

$$y^+ = \frac{u_* \, y}{\nu} \tag{3.49}$$

where u_* is the friction velocity at the nearest wall, y is the distance to the nearest wall and ν is the local kinematic viscosity of the fluid.

For all the turbulence model presented in this analysis a value of y^+ in the range between 0 and 100 is required for models using wall functions. However, to guarantee a good description of the boundary layer in all the operative conditions, is common practice, specially for the two-equations models, to use a value below one. As presented, for instance, in Figure 3.31, this condition has been taken in great care in the model development.

Model	Mathematical system	Quantity modelled
Baldwin Lomax	algebraic	mixing-length
Spalart Allmaras	one-equation	μ_t model
Yang Shih	two-equations	k - ε model
Shear Stress Transport	two-equations	k - ω model
Launder Sharma	two-equations	k - ε model

Table 3.6: Turbulence models synopsis

3.8.2 Models review and settings

In Table 3.6 a synopsis of the turbulence models used for the computation is reported. The basic information about these models and the choice made for the boundary condition are explained afterwards. For the definition of many auxiliary function and the values of the different constants, refer to [30] and [31], while for more specification about the boundary conditions [32] can be considered.

Baldwin Lomax

This is based on the Boussinesq eddy viscosity approximation, shortly presented in 3.4.1, which permits to compute the Reynolds stress tensor as the product of an eddy viscosity and the mean strain-rate tensor (equation 3.20); the eddy viscosity is computed in terms of mixing length, analogous to the mean free path in a gas. This quantity is a property of the flow rather then an intrinsic characteristic of the fluid and, for this reason, they are defined as *incomplete*, because the mixing length must be specified in advance. The Baldwin Lomax model is a two layer model where the turbulent viscosity in the inner layer is determined using the Prandtls mixing length model, while in the outer layer it is determined from the mean flow and length scale. The influence on the mean flow equations through the turbulent kinetic energy is neglected. Taken n as the normal distance to the wall and n_c as its smallest value at which the inner and outer viscosity are equal, the turbulent viscosity is defined as follows:

$$\mu_t = \begin{cases} (\mu_t)_i & n \leq n_c \\ (\mu_t)_0 & n > n_c \end{cases} \tag{3.50}$$

The inner viscosity is

$$(\mu_t)_i = \rho\, l^2\, |\omega| \tag{3.51}$$

The terms can be defined as follows:

$$l = k\, n \left(1 - e^{\frac{-y^+}{A^+}}\right) \tag{3.52}$$

$$y^+ = \left(\frac{\sqrt{\rho_w \tau_w}}{\mu_w} \right) n \tag{3.53}$$

and ω is the magnitude of the vorticity vector, for instance, for fully three-dimensional flow:

$$\omega = \sqrt{\left(\frac{\partial V}{\partial x} - \frac{\partial U}{\partial y} \right)^2 + \left(\frac{\partial W}{\partial y} - \frac{\partial V}{\partial z} \right)^2 + \left(\frac{\partial U}{\partial z} - \frac{\partial W}{\partial x} \right)^2} \tag{3.54}$$

The outer viscosity is

$$\left(\mu_t\right)_0 = K C_{cp} \rho F_{wake} F_{Kleb}(n) \tag{3.55}$$

where F_{Kleb} is the Klebanoff's intermitting function, F_{wake} is the minimum between:

$$n_{max} F_{max} \tag{3.56}$$

and

$$\frac{C_{wk} n_{max} \left[\sqrt{\left(u^2 + v^2 + w^2\right)_{max}} - \sqrt{\left(u^2 + v^2 + w^2\right)_{min}} \right]^2}{F_{max}} \tag{3.57}$$

This model is very easy to set-up, as it doesn't require the specification of any additional boundary condition; moreover the matching between its simplicity and its good physical foundation, allows to get useful results with a small resources consumption.

Spalart Allmaras

The Spalart Allmaras is a one-equation complete model which can be considered a bridge between the Baldwin Lomax (BL) and the two-equations models; its characteristics of robustness and capability of treat complex flow can be considered the main advantages of this approach, together with the definition of the eddy viscosity which is, in this model, continuous. The principle of this model is the resolution of an additional transport equation for the eddy viscosity, considering an advective, a diffusive and a source term, implemented in a non-linear manner. The turbulent viscosity is given by:

$$\nu_t = \nu f_{v1} \tag{3.58}$$

where the function f_{v1}ca be defined given the ratio $\chi = \frac{\tilde{\nu}}{\nu}$ between the working variable $\tilde{\nu}$ and the molecular viscosity ν:

$$f_{v1} = \frac{\chi^3}{\chi^3 + c_{v1}} \tag{3.59}$$

The turbulent working variable obeys the transport equation:

$$\frac{\partial \tilde{\nu}}{\partial t} + \overrightarrow{v} \cdot \nabla \tilde{\nu} = \frac{1}{\sigma} \{ \nabla \times [(\nu + (1 + c_{b2}) \tilde{\nu}) \nabla \tilde{\nu}] - c_{b2} \tilde{\nu} \nabla \tilde{\nu} \} + S_T \tag{3.60}$$

ν_T	1.5E-05	3.5E-05	5.5E-05	7.5E-05	1.0E-4	1.0E-3	1.0E-2	1.0E-1
$\frac{\mu_t}{\mu}$	1.1	2.56	4.03	5.49	7.33	73.33	734.37	7358.79

Table 3.7: Imposed kinetic eddy viscosity and computed dynamic eddy viscosity for Spalart Allmaras model

where $\vec{v}$ is the velocity vector, S_T the source term and σ, c_{b2} constants.

The application of this model requires the definition of a boundary condition of ν; for turbomachinery application (ref. [32]) the value is given in terms of ratio:

$$\frac{\nu_t}{\nu} \in [1;5] \tag{3.61}$$

In this range, however, the behaviour of the flow does not appear to change substantially. Some authors report an equation to explicit the relation between the turbulent viscosity and the turbulent intensity:

$$\nu_t = \sqrt{\frac{3}{2}} \times U_{ref} I_{tu} D_h \times 0.07 \tag{3.62}$$

Since neither of this approaches seemed to cause noticeable change in the behaviour of the fluid, an extended range of ν_t has been imposed (as reported in Table 3.7), trying to understand the effect on the performances. Unfortunately, however, the comparison between this model, even neglecting the boundary conditions settings, and the other tested appears to be very hard, due to the high discrepancies in terms of dynamic viscosity.

Yang Shih

The Yang Shih (YS) model is a two-equation scheme where two additional equations are solved: one (3.63) for the turbulent kinetic energy κ and the other (3.64) for the turbulent dissipation rate ε, for which the exact equation is derived and solved through a suitable closure approximation.

$$\frac{\partial \rho\kappa}{\partial t} + \nabla\left(\rho\vec{w}\kappa - \left[\mu + \frac{\mu_t}{\sigma_\kappa}\right]\nabla\kappa\right) = \left\{\overline{\rho\overrightarrow{w''} \otimes \overrightarrow{w''}S}\right\} - \rho\varepsilon \tag{3.63}$$

$$\frac{\partial \rho\tilde{\varepsilon}}{\partial t} + \nabla\left(\rho\vec{w}\tilde{\varepsilon} - \left[\mu + \frac{\mu_t}{\sigma_\varepsilon}\right]\nabla\tilde{\varepsilon}\right) = \\ = -\frac{1}{T}\left(C_{\varepsilon 1} f_1 \left\{\overline{\rho\overrightarrow{w''} \otimes \overrightarrow{w''}S}\right\} - C_{\varepsilon 2} f_2 \rho\tilde{\varepsilon}\right) + E \tag{3.64}$$

where S is the mean strain tensor and $\left\{\overline{\rho\overrightarrow{w''} \otimes \overrightarrow{w''}S}\right\}$ the turbulent Reynolds stress tensor. The variable $\tilde{\varepsilon} = \varepsilon - D$ is the modified dissipation rate and μ_t is given by

Turbulence intensity	**1%**	**2%**	**5%**	**10%**
		First attempt		
κ	4.1334	16.5336	103.335	413.34
ε_I	1537.65	24602.4	961031	15376496
ε_{II}	356.717	2853.73	44589.6	356717
$\varepsilon_{mean_{I,II}}$	947.183	13728.1	502810	7866606
$\frac{\mu_t}{\mu}$	121.51	134.31	143.51	146.72
		Second attempt		
ε_I	1537.65	24602.4	961031	15376496
$\frac{\mu_t}{\mu}$	76.9122	85.0142	90.8375	92.8694

Table 3.8: Imposed turbulent kinetic energy, turbulent dissipation rate and computed dynamic eddy viscosity for Yang Shih model

the product of the terms: ρ, C_μ, f_μ, κ, T. This is a first order model, which means that the turbulent Reynolds stress tensor is related to the mean strain tensor in a linear way:

$$\left(\rho\overrightarrow{w''}\otimes\overrightarrow{w''}S\right)_{ij}=2\mu_t\left[S_{ij}-\frac{2}{3}\left(\nabla\overrightarrow{w}\right)\delta_{ij}\right]-\frac{2}{3}\rho\kappa\delta_{ij} \tag{3.65}$$

The model requires to impose κ and ε as boundary conditions. As far as concerns the estimation of kinetic turbulent energy, it can be easily derived from the desired turbulent intensity, as follows:

$$\kappa=\frac{\sqrt{\overline{u'^2}}}{U_{ref}} \tag{3.66}$$

while three different levels of turbulence intensity are tested, for the main analysis a value of 1% will be taken. To estimate ε, three possibilities are given from the manual of the software([32]):

- specify the ratio of the turbulent viscosity to the laminar viscosity (for turbomachinery application a $\frac{\mu_t}{mu}=50$)

$$\varepsilon_I=C_\mu\frac{\mu}{\mu_t}\frac{\rho_{ref}\kappa^2}{\mu_t} \tag{3.67}$$

- specify the turbulence length scale:

$$\varepsilon_{II}=\frac{C_\mu^{\frac{3}{4}}\kappa^{\frac{3}{2}}}{\ell} \tag{3.68}$$

where ℓ can be taken equal to the tenth part of the hydraulic diameter.

- derive ε from the asymptotic turbulent kinetic energy equation in the following way:

$$\varepsilon_{III} = -u\frac{\Delta\kappa}{L} \tag{3.69}$$

- specify the wall shear stress

$$\varepsilon_{IV} = \frac{\left(\frac{\tau_{wall}}{\rho}\right)^{\frac{3}{2}}}{l} \tag{3.70}$$

The experience suggested to try eight different values for ε, considering a weighted mean value between the results of the first and the second methods and checking the value of $\frac{\mu_t}{\mu}$. The used values are reported in Table 3.8.

Shear Stress Transport

The Shear Stress Transport (SST) model is a two-equation eddy viscosity model intended to solve the problems of the Wilcox $\kappa-\omega$ model, very sensitive to the small free stream value of ω in free shear layer and adverse pressure gradient boundary layer flows.

In the Wilcox $\kappa-\omega$ model two additional transport equations for turbulent kinetic energy and specific dissipation rate, ω, are solved:

$$\frac{D\kappa}{Dt} = P_\kappa - \beta'\omega\kappa + \frac{\partial}{\partial x_j}\left((\nu + \sigma_\kappa \nu_t)\frac{\partial\kappa}{\partial x_j}\right) \tag{3.71}$$

$$\frac{D\omega}{Dt} = \alpha\frac{\omega}{\kappa}P_\kappa - \beta'\omega^2 + \frac{\partial}{\partial x_j}\left((\nu + \sigma_\omega \nu_t)\frac{\partial\kappa}{\partial x_j}\right) \tag{3.72}$$

Where P_κ is the production rate of turbulence and the turbulent kinematic viscosity ν_t can be define as the ratio between the turbulent dissipation energy κ and the specific dissipation rate of the turbulent frequency ω. First proposed by Menter in 1994, the Shear Stress Transport model allows to use Wilcox $\kappa-\omega$ model near solid walls and the standard $\kappa-\varepsilon$, in a $\kappa-\omega$ formulation, near the boundary layers edge and free-shear layers.

To set-up this model, the same parameters as the YS turbulence model were used.

3.8.3 Results

The results of the computations have been studied with the same method of the mesh assessment, namely through the quantities that will be measured both integrally and locally.

The Spalart Allmaras simulations cannot be compared with the other simulations and are presented separately, in Figure 3.32 and 3.33. On a logaritmic

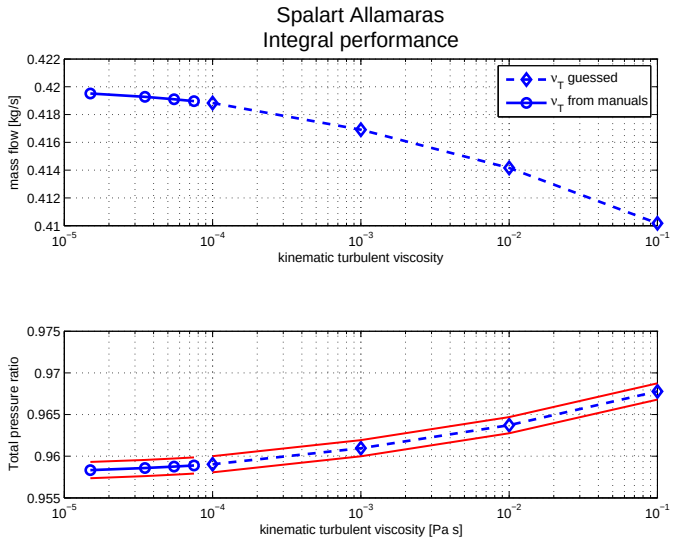

Figure 3.32: Mass flow and total pressure ratio for Spalart Allmaras turbulence model

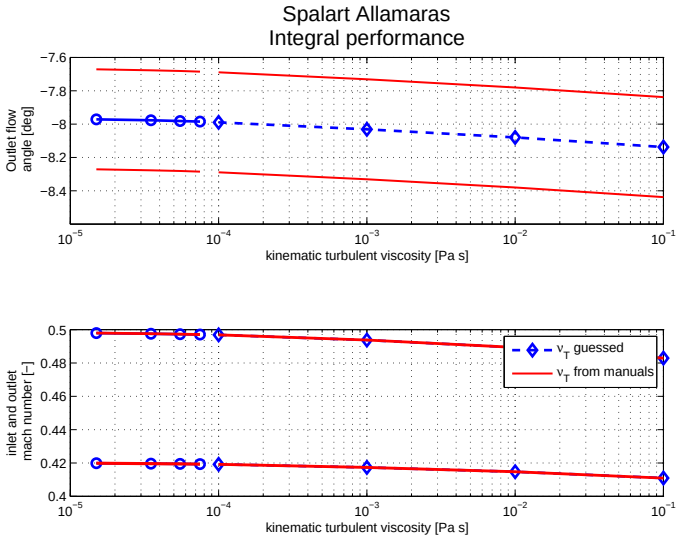

Figure 3.33: Outlet flow angle and inlet and outlet mach number for Spalart Allmaras turbulence model

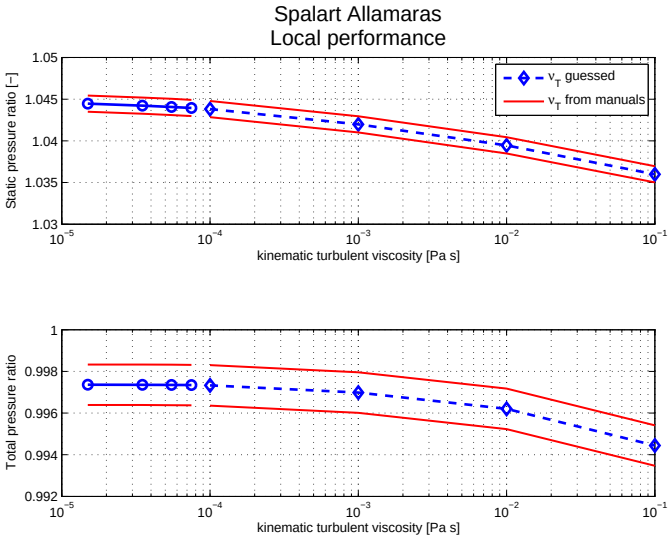

Figure 3.34: Mass flow and total pressure ratio for Spalart Allmaras turbulence model

scale the results from the two classes of values considered are presented; while the value from the manuals are presented by a continuous line, the other points represent the values chosen to stress the behaviour of the model with respect to the kinematic eddy viscosity.

Considering the total pressure ratio and the outlet flow angle the influence of this parameter appears to be of the same order of magnitude of the uncertainty. However, looking to the Mach number, the situation appears to be very different, due to the high accuracy of the measurements. This model will be abandoned for the main analysis because it does not permit to control the turbulence intensity and its level of accuracy is below the expectations.

In Figure 3.36 and 3.37 a comparison between the integral perfomances of the different models tested is presented. While for the Launder Sharma simulations the only value available was considered, for the Baldwin Lomax model, which does not allow to specify the intensity of the turbulence, the value was assumed constant in function of that quantity. The mass flow, the Mach number at the inlet and at the outlet present a decreasing trend; the flow angle appears to be almost constant in the range tested while the pressure ratio presents a minimum for $I_{tu} = 2\%$.

As far as concerns the local performances, some results are showed in Figure 3.38 and 3.39. The comparison between the different models is different as, for instance, the BL value appears to be a mean value, while representing a maximum in terms of integral quantities.

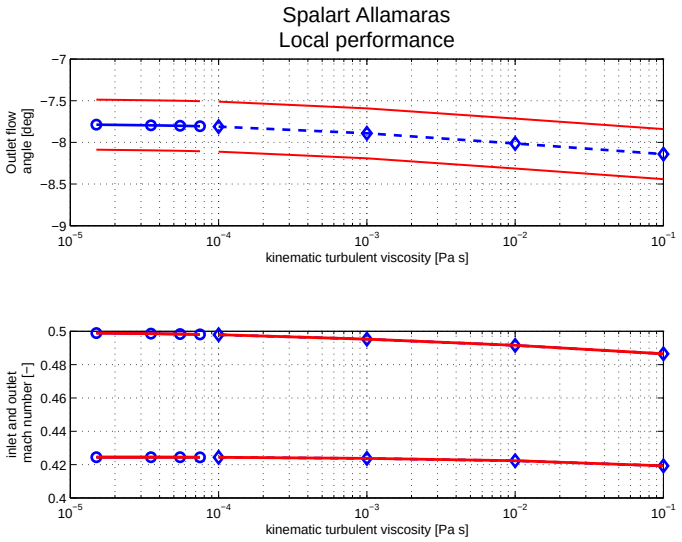

Figure 3.35: Outlet flow angle and inlet and outlet mach number for Spalart Allmaras turbulence model

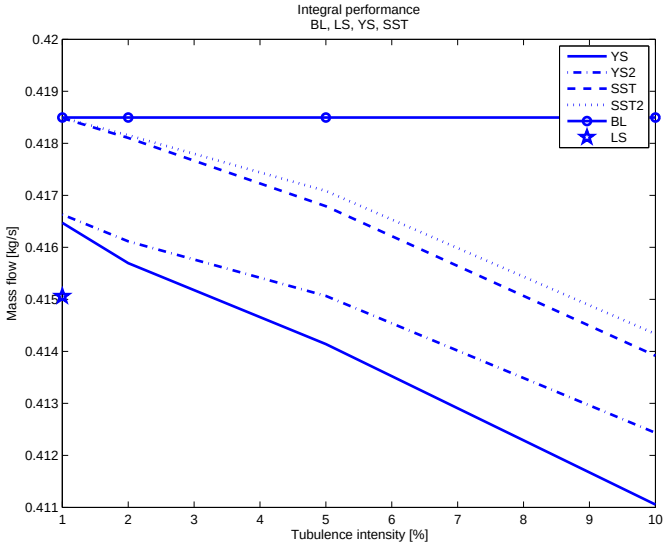

Figure 3.36: Mass flow angle for different turbulence models

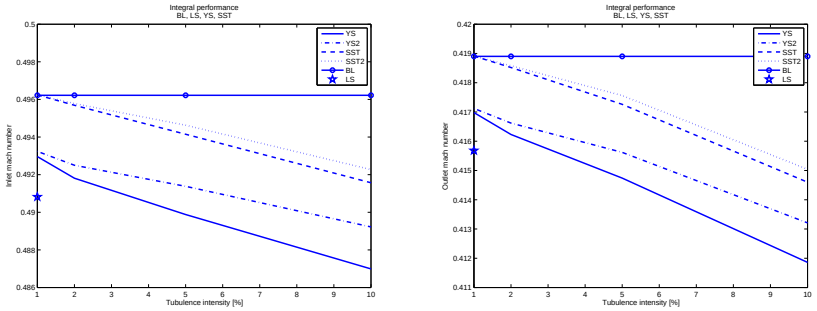

Figure 3.37: Inlet and outlet mach number for different turbulence models

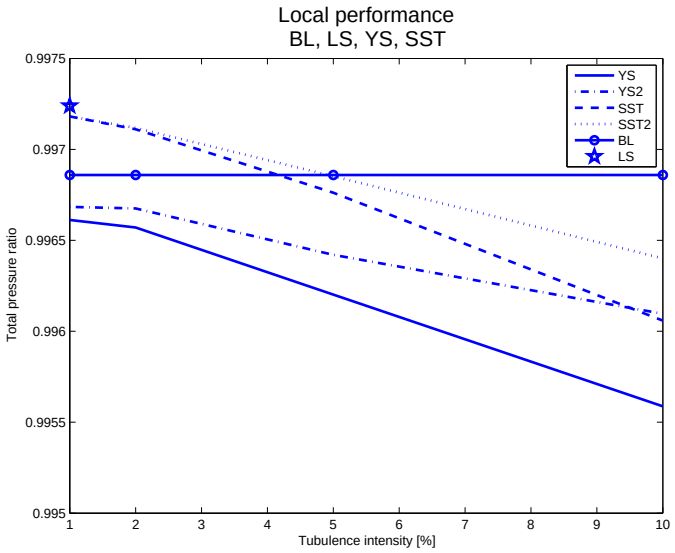

Figure 3.38: Total pressure ratio for different turbulence models

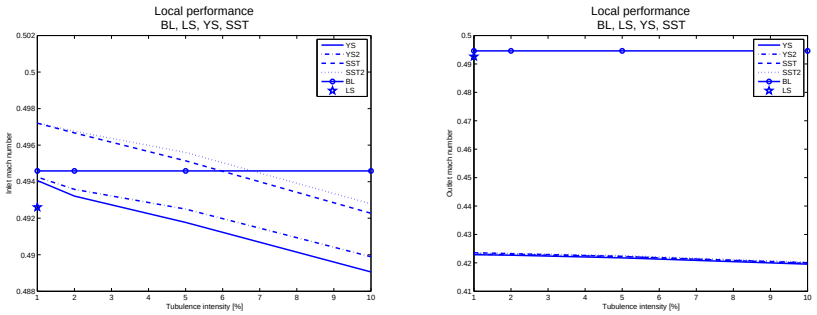

Figure 3.39: Inlet and outlet mach number for different turbulence models

Considering the two-equations models, it can be seen that the different settings in term of ε cause a different inclination for almost all the quantities starting from $I_{tu} = 2\%$, apparently in agreement with the highest turbulent dissipation rate of YS2 and SST2 which cause a slighter influence of the turbulence increase. However these characteristics do not affect the results and the differences are usually almost negligible for all the quantities, specially for low turbulence intensities. In addition, to neglect the influence of the turbulence, for the main analysis ε will be taken equal to the values computed through 3.67, for a turbulence intensity equal to 1%. Looking at the comparison between the SST and the YS models, a similar trend can be seen; the different ε appears to affect the second model more than the first, causing a higher slope and then a higher dependence of the performance on the turbulence intensity.

The complete analysis is performed using three different turbulence models for the following reasons:

Shear Stress Transport This model appears to be the best choice in terms of independence from the turbulence intensity and boundary layer treatment; it represents one of the most accurate and solid choice for turbomachinery applications, even in presence of separation.

Yang Shih The good experience of the work group reported in previous projects using this $\kappa - \varepsilon$ model, suggests the opportunity to evaluate its behaviour on the current model.

Baldwin Lomax The robustness and the low computational cost make this zero-equation turbulence model interesting when a first guess of the flow behaviour is needed. It seems of interest then, to quantify the error of the results from this model with more accurate predictions.

Chapter 4

Results

The main objective of the present work is the analysis of the performance and stability of a linear compressor cascade in cruise condition from choke to stall, varying the solidity. In this chapter the results of the investigation will be presented. Firstly the results from SST turbulence model are analysed; after the presentation of the incidence and Mach number ranges investigated, a phenomenological analysis of the limit conditions of the cascade is shown; the behaviour of the most interesting design quantity is then analysed in the whole incidence range for different inlet Mach number condition. The following section presents the comparison with the literature data. The effect of achieving the same solidity with different combinations of chord and pitch is then analysed, before the comparison between slip and no-slip boundary condition results. In the end the results from the three different turbulence model are presented, considering the main design parameters and a description of the flow topology.

4.1 Mach number and incidence ranges

The inlet Mach number range of interest for the test is set on the basis of the operative conditions of the stage, which lays between 0.45 and 0.6; an increase of this interval has been performed, where possible, from 0.4 and 0.8 to extend the application field and the validity of the results. The inlet Mach number can not be set directly as boundary condition and it is then extrapolated from the inlet total pressure imposed, after a iterative process; for each incidence condition, the Mach number interval is discretized into five values. While the lower value of 0.4 is easily set in every condition, some problems show up trying to reach the value of 0.8 in correspondence of the lowest and the highest incidences. For the lowest incidences the limit is set by the choke condition, while for the highest incidences the stall of the aerofoil does not allow to reach the desired values.

As far as concerns the incidence range, appears to be of great interest the study of the widest range possible due to the undeniable benefit coming to the stage control in terms of mass flow. The lower limit was set a priori at an incidence $i =$

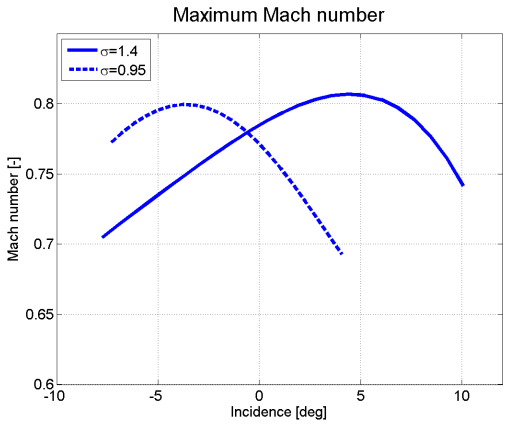

Figure 4.1: Maximum mach number reached for two different levels of solidity

$-13.5°$, but this condition appeared to present convergence problems for Mach number below 0.6, considering the SST turbulence model chosen for the analysis. The value $i = -7.4°$ was then considered for all the solidities tested. It must be said, however, that this value can hardly be considered of some interest for design purpose, because of the considerable value of losses registered. Regarding the upper limit, its value was chosen according to the capability of the solver to compute a stable solution; the stationary model used for the analysis does not allow, the description of a flow inherently characterized by a unstable behaviour, as it is near to stall condition. The highest positive incidence considered is then the highest possible to reach the desired value of Mach. This value, then, does not represent an absolute limit for the cascade, which could be tested in a wider range of incidence considering a reduced limit in Mach number.

In Figure 4.1 is presented the modelized behaviour of the maximum Mach number respect to incidence for two different values of solidity. As this model is based on the values imposed for the present analysis, the top of the curves is limited to a value around 0.8, but is known that these curves present a maximum corresponding to the unique incidence condition. However, neither this point nor the "tails" of the curves appear to be of interest for the current application and as a consequence, they are not investigated.

As presented in the previous chapter, the stall limit is expected to vary in function of solidity. The results which confirm this tendency will be presented in the following sections.

4.2 Limit conditions

4.2.1 Choke

The lower limit of the cascade incidence range is set by the choke condition. This phenomenon is characterized by the maximum flow rate and by the rise of shock waves through the flow which penalize both the performance and the regular behaviour of the cascade. At highly negative incidences the flow is forced to a remarkable rotation to go through the blade passage. The increase in the pressure ratio, in the present case realized through the increase of the upstream pressure, progressively prevents a smooth adaptation of the flow to the downstream conditions. The Mach number is increased and thus even being subsonic upstream could reach sonic condition inside the passage according to the local acceleration of the fluid, due to the shape of the blade. A sonic regime extended to the whole passage section forestall, the pressure wave to go upstream, causing a raise in the pressure ratio to be totally ineffective on the mass flow rate. In a real compressor stage, this condition is not dangerous by itself even if it is usually undesired, because it sets a limit to the adjustability of the machine; for this reason, as a limit for the present analysis, an incipient choke condition is considered, namely the lowest pressure ratio corresponding to the asymptotic value of the Mach number is imposed.

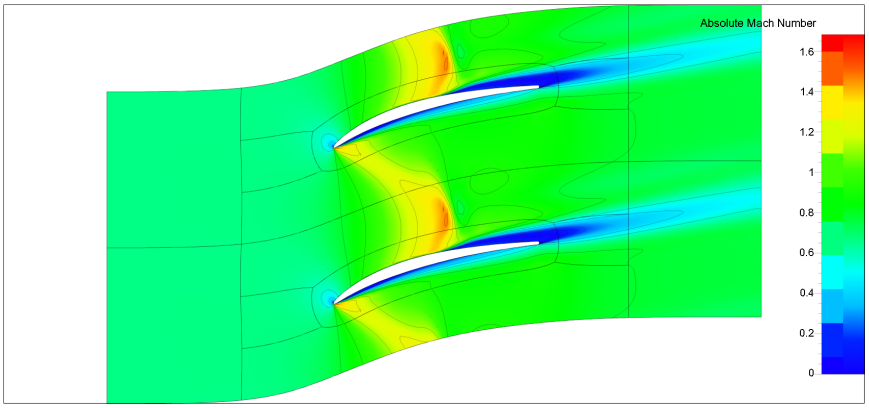

Figure 4.2: Choke - Mach number distribution on the blade to blade section at midspan; $\sigma = 1.38$, $M_1 = 0.5$

Analysing for instance the Mach number and static pressure distributions for the highest solidity on the blade to blade view of the passage at midpsan, shown in Figure 4.2 and 4.3, two phenomena appear to be of interest: the shockwave inside the channel and the separation zones around the blade.

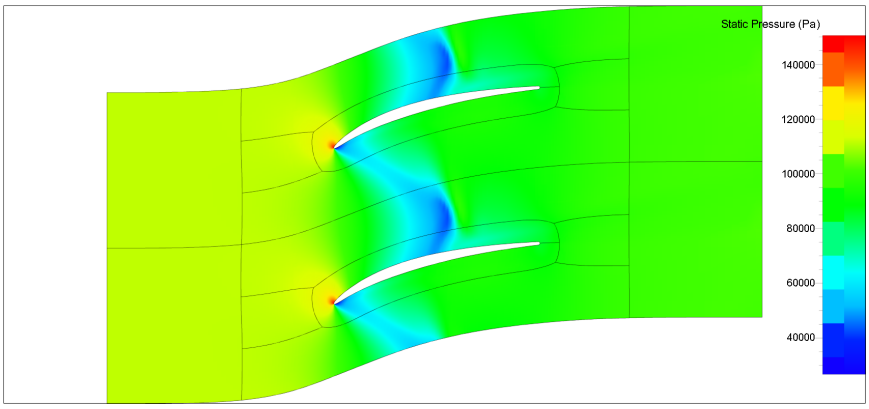

Figure 4.3: Choke - Static pressure distribution on the blade to blade section at midspan; $\sigma = 1.38$

Shock wave

The almost **normal shock wave** inside the passage is clearly noticeable from both the quantities here reported. The shock goes through the channel from the leading edge to a position around 60% of the chord on the extrados, where the intensity of the re-compression is higher, due to the velocity profile next to this side of the blade. As far as concerns the solidity effect on this phenomenon, it can be said that the position and the shape of the shock remain constant for all the tested configuration, while the distributions of Mach number and static pressure appear to change.

Looking at the distributions of the quantities on the blade, for instance the isoentropic Mach number, in Figure 4.4(a), these comments can be verified: the big drop in Mach number on the suction surface is located for all the configurations at 0.55 of the chord; as far as concerns the pressure side zone after the leading edge, it can be seen that for higher solidity the Mach is higher, even if the distribution is identical after 20% chord. Considering the plot in Figure 4.4(b), it can be seen that the effect of the choke on the blade is less important while increasing the distance from midspan. Looking at the friction coefficient in Figure 4.5 analogous observation can be remarked, even if a slight translation downstream of the shock effect on the back side is present. In the middle of the channel the effect of solidity is more important: as the chord to pitch ratio is decreased, the blockage effect is reduced as the acceleration of the flow. The pressure ratio over the shock is than lower and consequently the losses caused by the phenomenon.

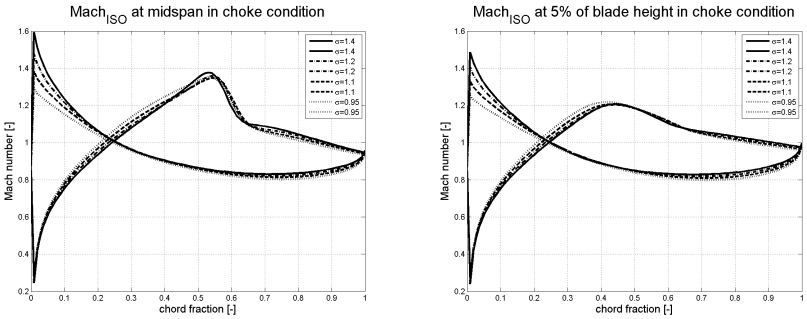

(a) (b)

Figure 4.4: Choke - Isoentropic Mach number distribution along the blade at midspan and at 5 % of the span height for different solidity configurations

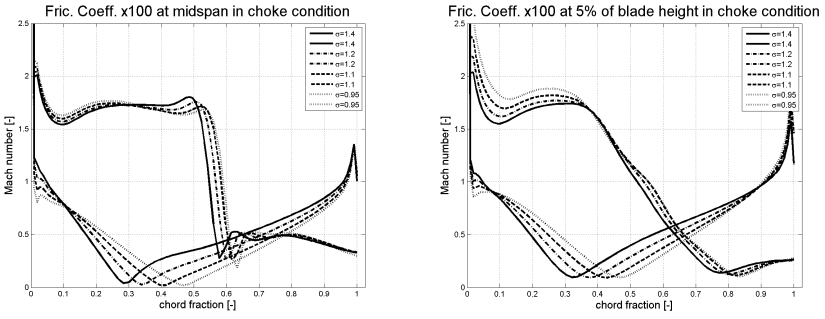

(a) (b)

Figure 4.5: Choke - Friction coefficient distribution along the blade at midspan and at 5 % of the span height for different solidity configurations

Flow separation zones

Considering the maps of Mach number and Total pressure (Figure 4.6), wide separation zones can be identified on both sides of the blade, in different positions. On the extrados near to the leading edge, the flow is accelerating, hence it remains attached to the wall; the detachment starts before the shock wave region, at a distance which increases slightly with the solidity. On the opposite side of the blade, the flow detaches right after the leading edge being gradually accelerated by the main stream drag; this behaviour is clearly noticeable in Figure 4.5(a), looking at the lower family of curves, which represent the friction coefficient along the convex side of the blade; the plot presents a minimum corresponding to the zone where the velocity is reversed. It can be seen that the minimum point is set in different position for different solidity, sliding downstream while decreasing this parameter.

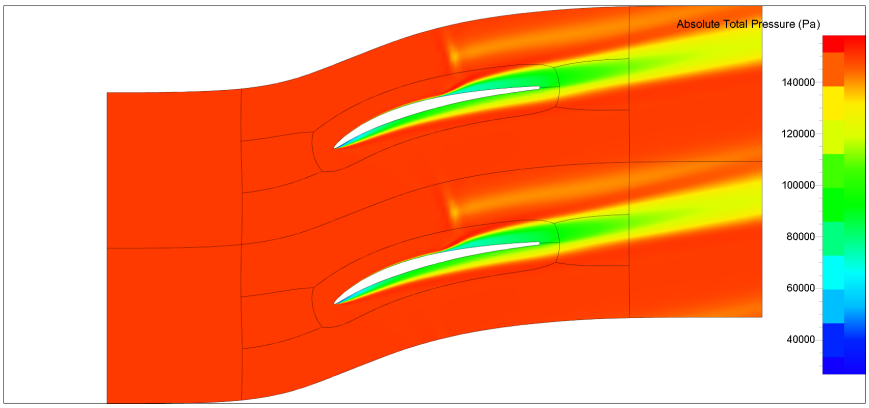

Figure 4.6: Choke - Total pressure distribution on the blade to blade section at midspan; $\sigma = 1.38$

On the trailing edge the wakes coming from the two sides of the blades are unified; in Figure 4.7 is represented the behaviour of the loss coefficient ($\omega = \frac{p_{01}-p_{02}}{p_{01}-p_1}$) along the pitch at midspan after 1 chord from the trailing edge. Considering an increase in solidity, three main facts can be noticed:

1. the maximum value of the losses increases
2. the pitchwise coordinate of the maximum loss shifts towards the extrados side of the channel (the deviation of the wake is higher)
3. the width of the curve increases

In Table 4.1 are reported the adimensionalized quantities representative of the previous observation, normalized to the value corresponding to the maximum solidity configuration; it is interesting to remark that while the peak pressure loss

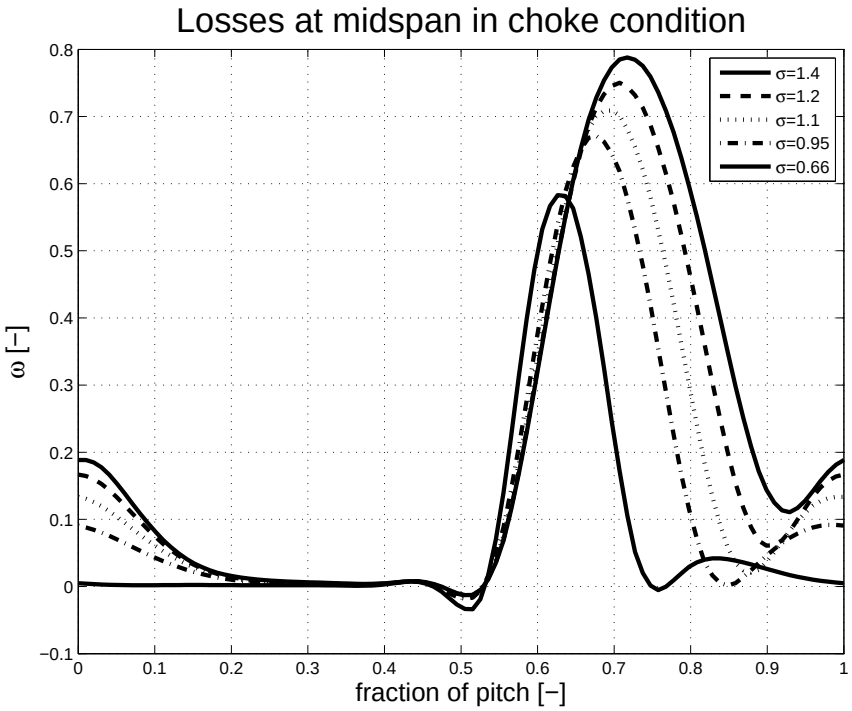

Figure 4.7: Choke - Loss coefficient distribution along the pitch at midspan on the surface at 1 chord from the trailing edge for different solidity configurations

decreases just of the 26% respect to the baseline, the integral value of the losses along the pitch falls down of more than a 65%, due to the lengthen of the wake.

σ	1.38	1.24	1.10	0.95	0.66
Maximum Loss value	1.0000	0.9415	0.8817	0.8167	0.7399
Maximum Loss coordinate	1.0000	0.9722	0.9444	0.9167	0.8750
$\frac{\int_p \omega_{\sigma_i}}{\int_p \omega_{\sigma=1.38}}$	1.0000	0.8388	0.6796	0.5251	0.3491

Table 4.1: Choke - Wake characteristics

As far as concerns the map of the losses on the outlet surface after 1 chord from the trailing edge, represented in Figure 4.8, it can be observed, together with the already remarked general increase in losses, the interaction with the end-wall boundary layer while the solidity is increasing.

4.2.2 Configuration near to stall

The characteristics of the model used for the present analysis, do not permit the description of the stall condition, due to the different nature of the phenomena involved. The positive incidence limit is set to the maximum value which allows to reach the convergence on the least desired value of Mach number. As expected from the literature, the stall margin decreases with the solidity following a linear relation.

As far as concerns the behaviour of the cascade, three different phenomena are considered: a shock on the suction side, a wide diffusion area on the pressure side and the development of the separation region.

Shock

Looking at the Mach number distribution, reported in Figure 4.9 for the maximum solidity configuration, it is possible to see an abrupt acceleration of the flow on the suction side some percentage of chord downstream the leading edge, followed by a sudden re-compression through a shock. Downstream the shock, the flow is characterized by high losses developing on the blade surface.

Considering the distribution of Mach number along the blade at midspan, reported in Figure 4.10(a), it can be seen that the intensity of the supersonic bubble decreases with solidity, even disappearing for the lower value; considering the position of the shock, it moves upstream while decreasing the chord to pitch ratio. Regarding the wake development, it is possible to see how the friction coefficient reaches its minimum value in correspondence to a different axial coordinate, increasing with solidity. The shape of the curve clearly shows the effects of the shock presence for the two highest solidities, while for the other

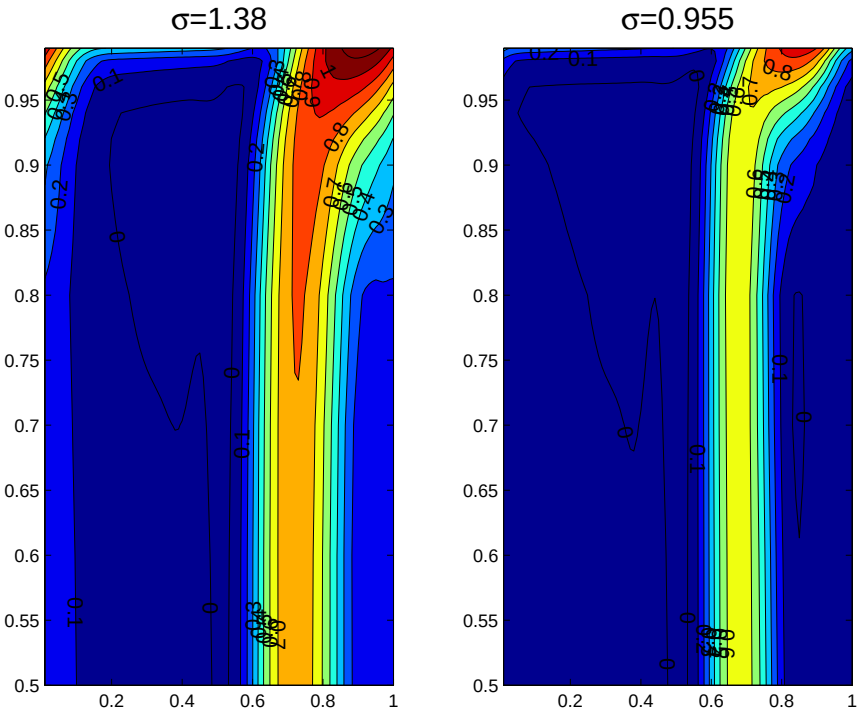

Figure 4.8: Choke - Loss coefficient distribution on the surface at 1 chord from the trailing edge for different solidity configurations

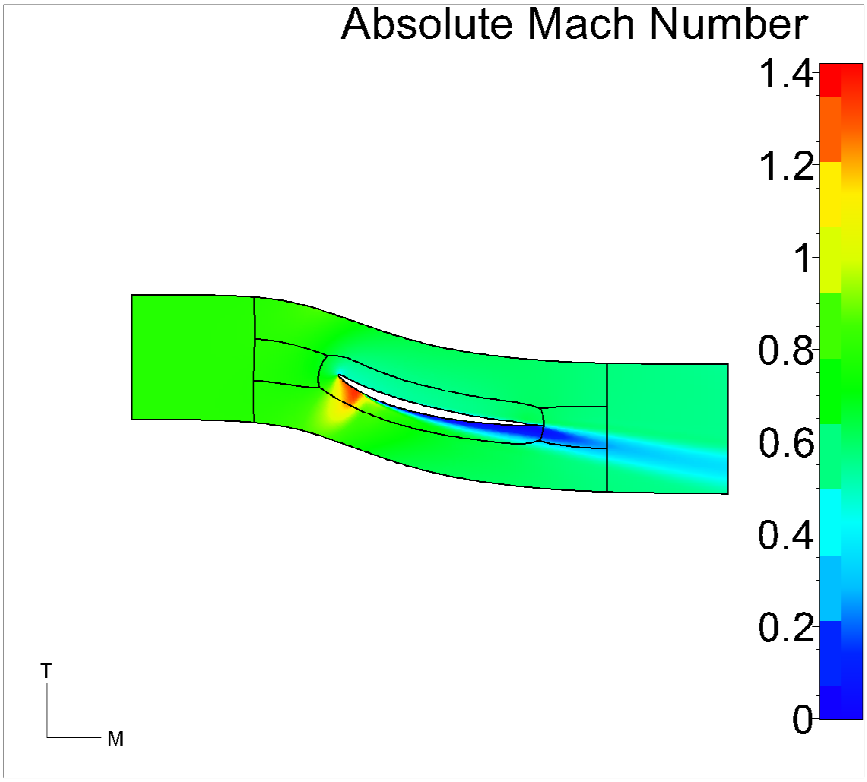

Figure 4.9: Mach number distribution on the blade to blade surface at midspan near to stall condition; $\sigma = 1.38$

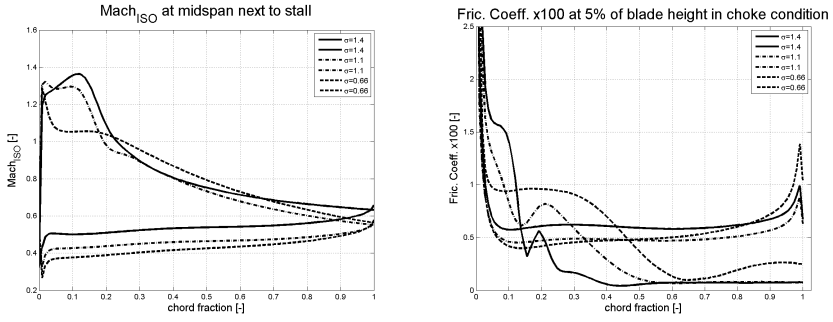

(a) (b)

Figure 4.10: Stall - Mach number and Friction coefficient distribution along the blade at midspan for different solidity configurations

configuration considered, a wide flat zone until 30% of the chord after the leading edge is noticeable. As far as concerns the wake characteristics the behaviour with respect to the solidity is analogous at the one outlined in choke condition; the sensitivity of the wake width and peak value respect to solidity is higher in this condition.

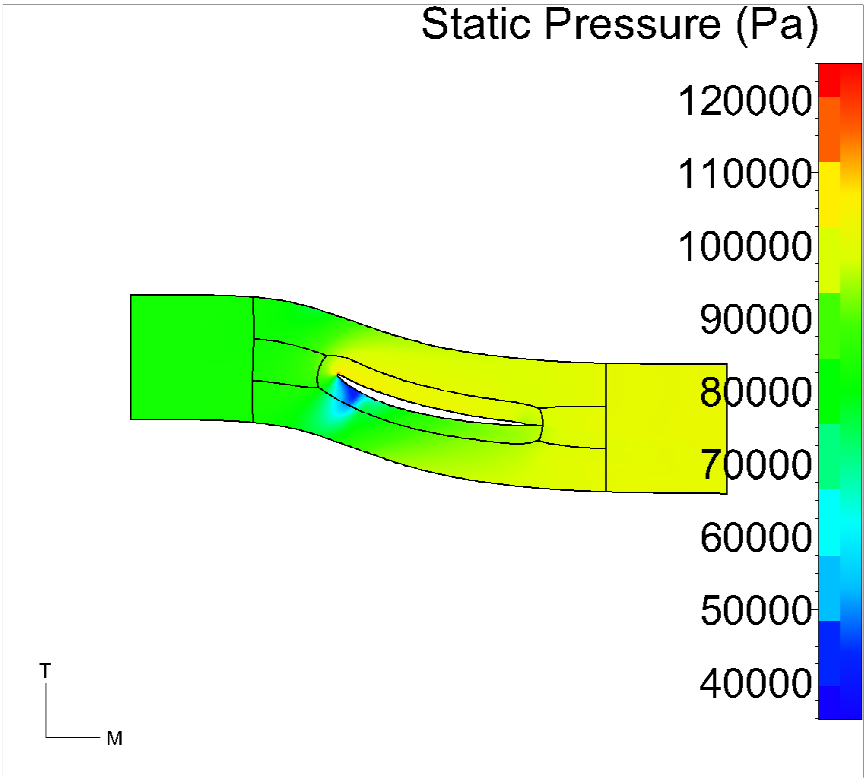

Figure 4.11: Static pressure distribution on the blade to blade surface at midspan near to stall condition; $\sigma = 1.38$

Diffusion

On the pressure side of the blade an extended diffusion area appears right after the leading edge. This behaviour can be outlined both from the reduction in Mach namber in plot 4.9 and increase in static pressure (Figure 4.11). On the blade it is possible to see the same behaviour, looking for instance, at curve in Figure 4.10(a). The decrease in solidity causes the increase of this phenomenon, extending its area upstream the channel.

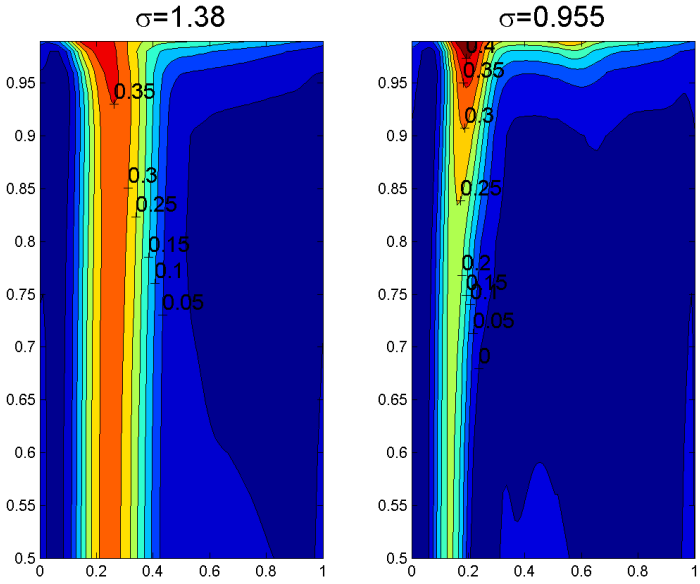

Figure 4.12: Losses distribution on the outlet surface one chord downstream for different solidity configuration

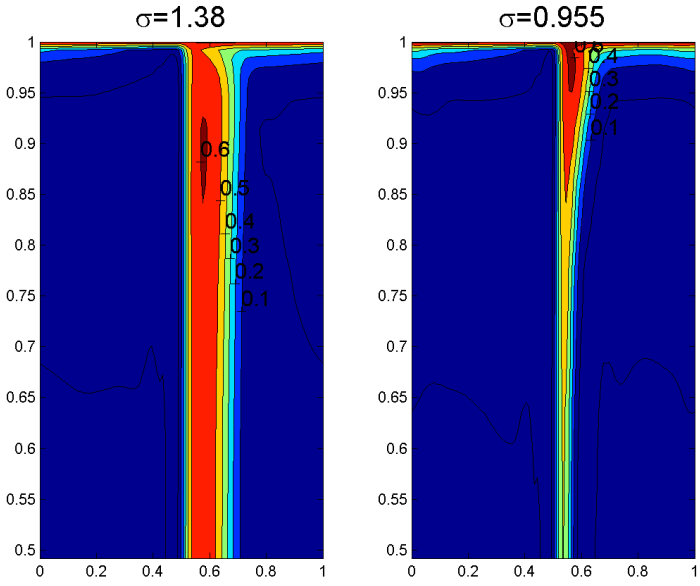

Figure 4.13: Losses distribution on the outlet surface at a distance of 15% chord downstream for different solidity configuration

Separation region

In Figure 4.12 and 4.13 is presented the behaviour of the losses on the outlet plane at two different distances from the trailing edge for two different values of solidity. Both the pictures show that the behaviour of the two configurations appears to be very different; while for the high solidity the track of the wake is almost constant until 95% of the blade height, for the low solidity is clearly represented a track of great separation which starts right after the maximum thickness and grows along the channel; considering the development of the losses distribution downstream the channel, one can say that the losses are redistributed on a wider surface of the channel. At low solidity while the core of the separation track remains around 95% of the blade height, the shape is modified, stretched in the span wise direction.

4.3 Cascade performance analysis

As presented in the previous chapter, two different types of quantities have been taken into account for the analysis; the mass-averaged values at midspan are named "local value", while the term "integral or global quantity" will be used for the mass-averaged value on the surface. The results presented in this section are extracted from a surface one chord downstream the trailing edge.

Turning

In Figure 4.14 is presented the turning ($\Delta\alpha = \alpha_1 - \alpha_2$) of the cascade at $M_1 = 0.5$. The curve presents a linear trend respect to the incidence, excluding the highest solidity in the last segment near to stall, where the slope decreases. It can be noticed that this quantity decreases with solidity, being more sensitive to this parameter at incidence near to stall; this difference increases with the Mach number.

As far as concerns the comparison between the global and the local values, the difference between the two is usually below the least measurable value of 0.3°; at high Mach number for positive incidences the gap slightly exceeded the threshold, specially for low solidity.

Deviation

The deviation ($\delta = \alpha_2 - \alpha_{geom}$) presents an increasing trend in respect to the incidence angle; the behaviour is not linear; while increasing the Mach number, the deviation decreases, with a proportional relation. The curves $\delta = \delta(M)$ present the same inclination for all the incidences. The solidity effect on this parameter appears to follow the theoretical expectation: decreasing the pitch to chord ratio the deviation decreases, as the guidance of the flow is reduced. While the comparison with the deviation rules at optimum incidence will be presented

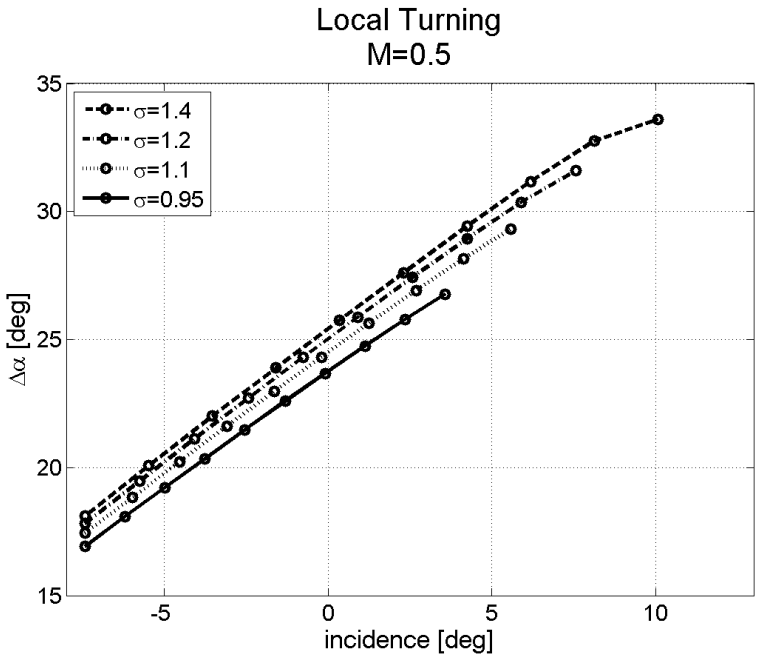

Figure 4.14: Turning in function of incidence for different solidity configurations

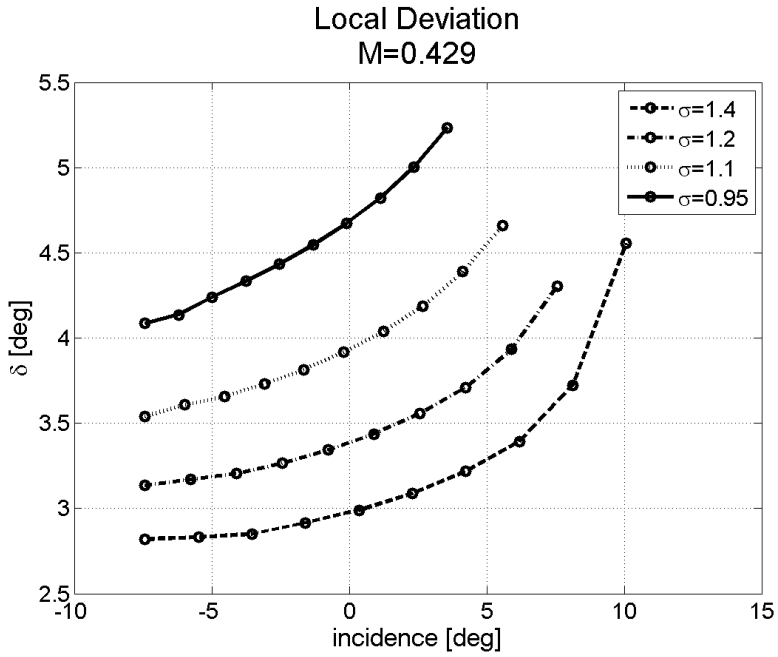

Figure 4.15: Deviation in function of incidence for different solidity configurations

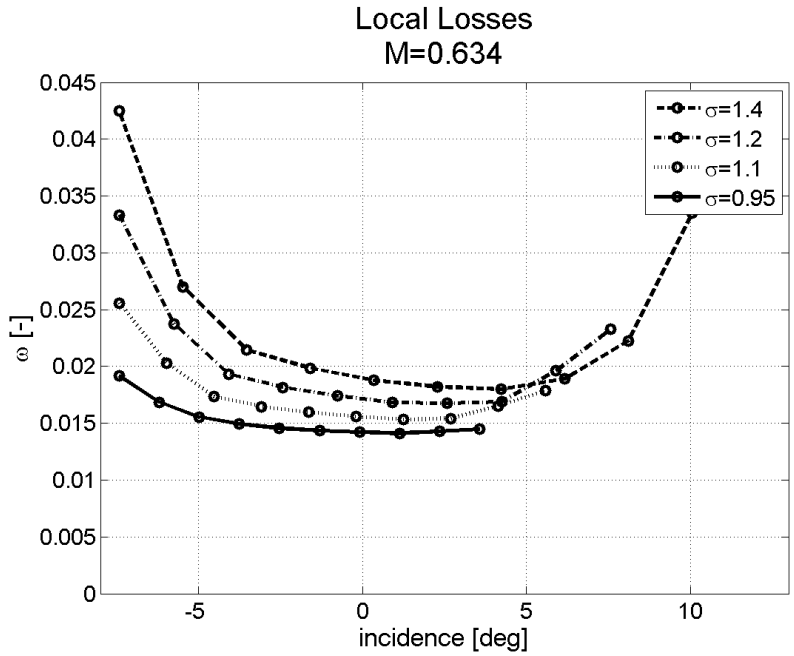

Figure 4.16: Total pressure loss parameter in function of incidence for different solidity configurations

afterwards, it can be noticed in this plot that the dependence of the deviation on the solidity is not constant varying the incidence, i.e. the curves are not parallel but, going towards negative incidence values, the solidity effect appears to be slightly reduced.

Excluding the high Mach number and high incidences conditions, the end-walls effects do not appear to influence this parameter in a measurable way, since the difference between local and integral data remains within the expected uncertainty range, even though it appears a slight difference in the shape of the local curve which presents, for the two highest solidities at the highest Mach, a minimum which does not correspond to the choke incidence, while looking at the global ones this translation of the minimum value is missing.

Losses

An example of the losses development in function of incidence for a given Mach is plotted in Figure 4.16. The curves present a minimum which lays in the positive range of incidences, although it is present a wide flat zone where the increase of the losses is very low and this permits to maintain good efficiency while varying the angle of attack, i.e. varying the mass flow. The flat region gets wider while decreasing the Mach number. While usually the losses at midspan increase

with the Mach number, their integral value on the whole section shows the opposite trend, presenting a slightly decrease for all the solidity but the highest, for which there is agreement between the two different quantities behaviour. The difference between local and integral loss can be considered as an index of the importance covered by the losses due to phenomena developing near to the end-wall boundaries. This index usually presents two different trends:

1. it decreases with the Mach
2. it increases in a large range of incidence, presenting a maximum next to the minimum local loss incidence and then decreasing until the last available condition

The solidity has a main role in determining the loss importance, as it influences both the size of the wet surfaces, hence the friction losses, and the profile losses. In the tested range of solidity the first source of loss is still the predominant, then the losses present a negative trend increasing the solidity. Some differences are noticeable while the solidity is increasing:

- the loss corresponding to the last available incidence is higher
- the minimum of the curve, even remaining in the positive range of incidence, moves towards zero incidence (as it will be presented afterwards)
- on the choke side the losses appear to be more sensitive to the solidity effect
- the solidity effect is slightly stronger while increasing the Mach
- the weight of the end-wall boundary interaction losses is more important for high solidities, specially at low incidence.

Diffusion factor

In general, the diffusion factor has a linear positive trend in function of incidence, as showed in Figure 4.17; an exception shows up considering the local value near to stall for high incidence: the curve presents a maximum and then decreases. This parameter appears to be proportional to the Mach number as well. The difference between the local and the global values is negligible at low Mach, slightly increasing with this parameter.

As expected, the solidity effect strongly influences the diffusion factor; this parameter decreases approximately as the fourth power of the inverse of solidity.

Massflow

One of the parameters heavily affected by a modification in solidity is the mass flow, which represents also a very important requirement for the whole design

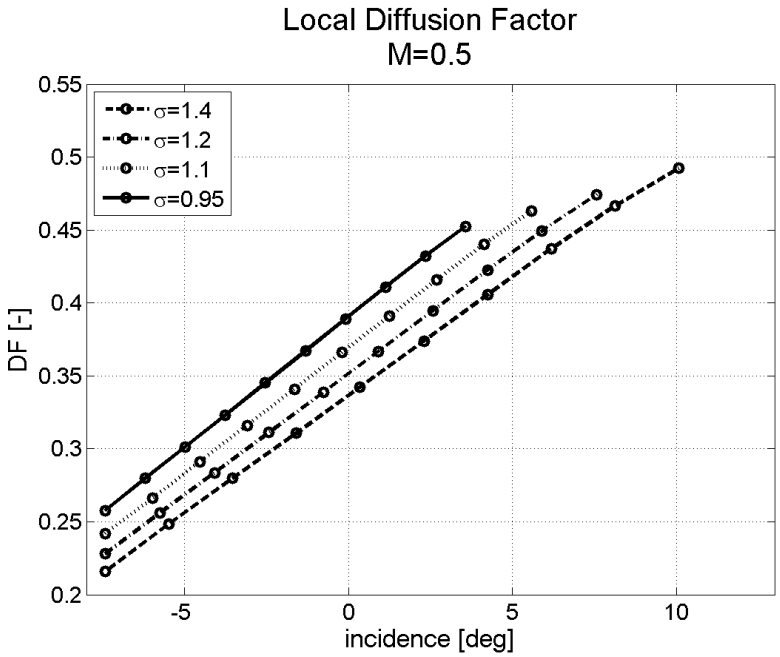

Figure 4.17: Total pressure loss parameter in function of incidence for different solidity configurations

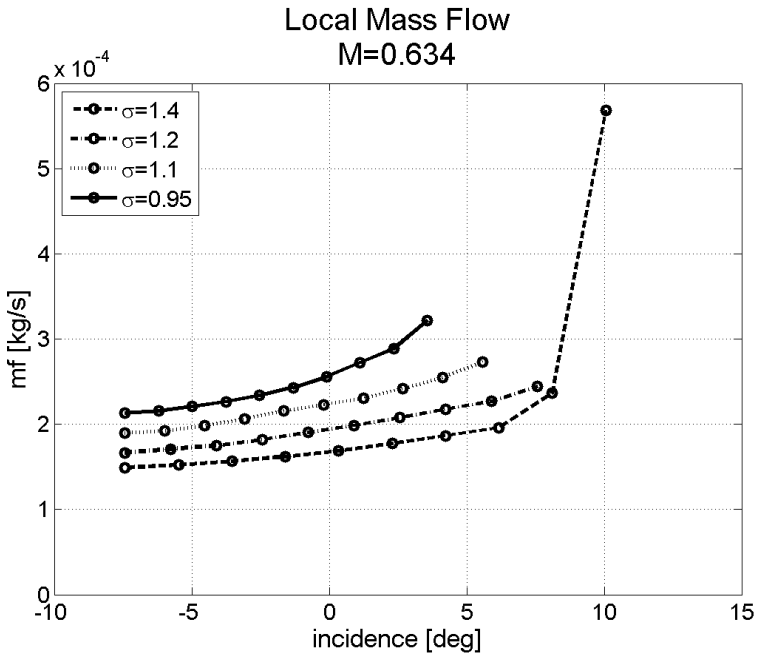

Figure 4.18: Mass flow at minimum loss incidence in function of incidence for different solidity

process of the stage. Considering the plot in Figure 4.18 it can be seen that the relation between the massflow and the solidity is linear, depending mostly on the variation in pitch through which the solidity is varied to obtain the present plot. A slight increase of the impact of solidity is noticeable increasing the incidence. From the designer point of view, this modification in the mass flow implies an important overhaul of the design of the channel as it affects, for instance, the variation of the blade height on the meridional plane.

4.4 Comparison with literature data

The correlations used to evaluate the solidity are usually given for the design incidence; while for Lieblein, Carter and Zweifel this condition is considered as the mean incidence between the two stall conditions, Howell defines a different design condition based on the turning. In Figure 4.19 is presented the behaviour of the design incidence respect to the solidity; while the condition used by Howell clearly implies a linear trend, the other condition does not present a clear trend. It is important to observe, however, that the difference in optimum losses incidence represents an important point while assessing the performance for different solidities in design condition.

4.4.1 Deviation rules

In paragraph 2.3.1 the correlations to compute the deviation have been presented; the geometrical data from the cascade are used to evaluate the difference from the expected deviation: the comparison is reported in Figure 4.20; the following remarks can be outlined:

1. the correlation by Howell, even if accurately predicts the shape of the curve, sets the deviation for all the solidity configuration to a negative value, suggesting that it is not suitable for the current cascade blading.

2. the correlation by Carter over-predicts the deviation, especially at high solidity; the difference with the actual deviation is always around 1°.

3. the correlation by Lieblein predicts very well the behaviour of the cascade, especially at high solidity. The error increases while decreasing solidity, but until a value of 0.95 it remains below 1.5°.

4.4.2 Loading criteria

The most used loading criteria have been presented in paragraph 2.3.2; all of them are based on the definition of a coefficient solidity-dependant clamed to be meaningful to determine the blade loading and then impose a limit on this parameter to compute the desired solidity. In the following paragraph is presented the inverse procedure, computing the coefficients on the available

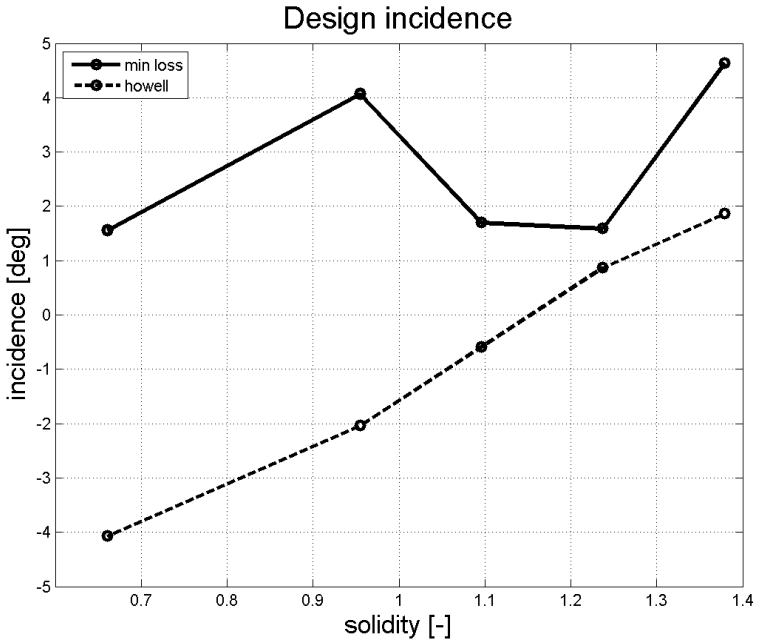

Figure 4.19: Design incidences in function of solidity

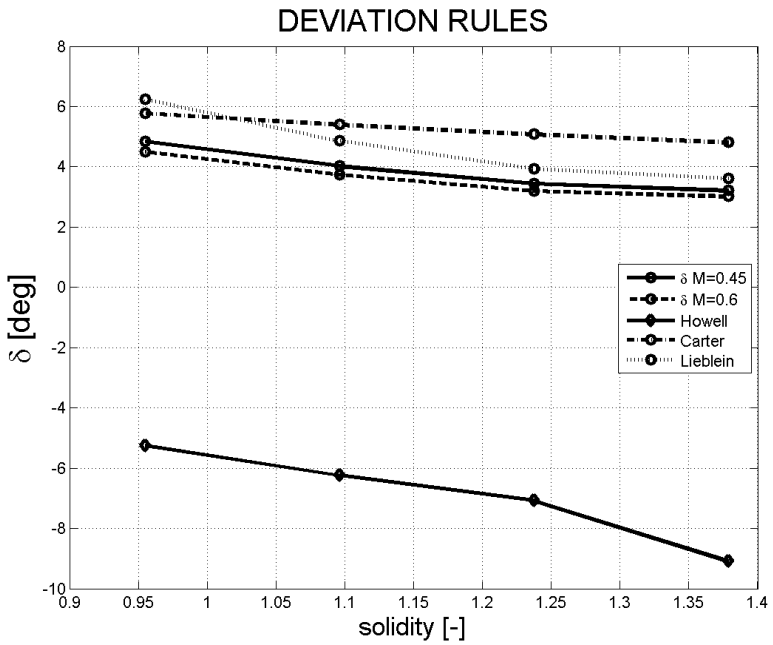

Figure 4.20: Deviation rules comparison

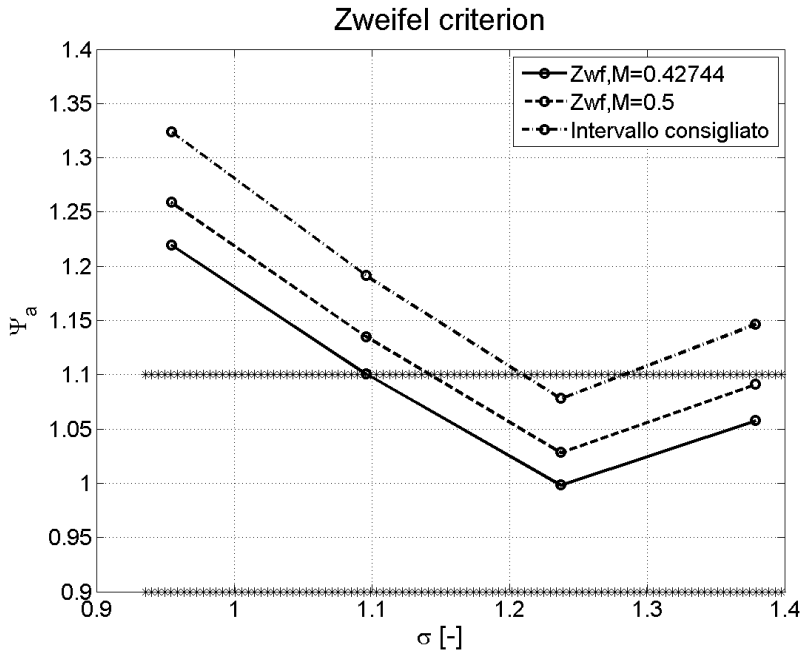

Figure 4.21: Zweifel coefficient

solidity data to compare the results of the computation with the limit set by the authors.

Zweifel

The definition of the Zweifel coefficient is based on the comparison between the pressure distribution observed for the blade and an ideal pressure distribution, i.e. the total pressure equal to its maximum level on the whole suction side of the blade, falling to the outlet static pressure at the trailing edge while on the pressure surface it assumes the value of p_2 from the leading edge on. Looking at the computed value of Zweifel coefficient in Figure 4.21, it appears that all the cascade configurations, including the baseline which represents the state of art, present the tendency to operate outside the suggested range:

$$\Psi_a \in [0.9, 1.1]$$

in most part of the condition of interest. It could be asserted that the margin range choice seems questionable and could be extended on the upper side, as presented by Zweifel himself in the original paper.

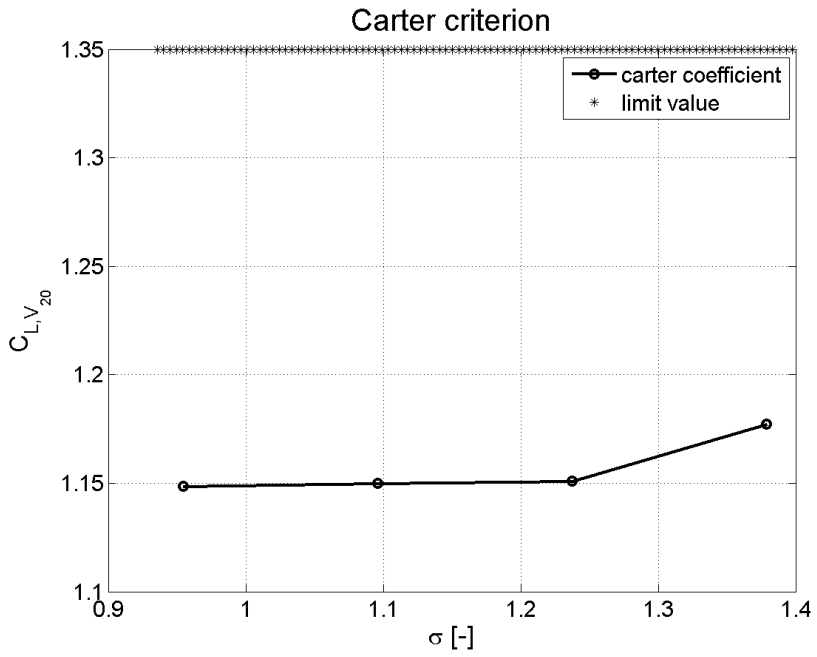

Figure 4.22: Carter coefficient

Carter

The behaviour of the Carter coefficient is presented in Figure 4.22; the coefficient is not affected significantly by the Mach number variation and it does not appear to be influenced significantly by the change in solidity, showing a behaviour mostly dependent on the incidence.

Lieblein

Instead of the total pressure loss coefficient, the Lieblein correlation uses a different parameter to represent the loss, i.e. the ratio between the momentum thickness and the chord; this quantity can be computed through different assumptions with different degrees of approximation:

$$\zeta_1 = \omega \frac{\cos\alpha_2}{2\sigma} \qquad \zeta_2 = \omega \frac{\cos\alpha_2}{2\sigma} \left(\frac{\cos\alpha_2}{\cos\alpha_1}\right)^2 \qquad \zeta_3 = \omega \frac{\cos\alpha_2}{2\sigma} \left(\frac{v_1}{v_2}\right)^2$$

Optimum incidence condition In Figure 4.23 is presented the comparison between the three different parameters versus the diffusion factor (equation 2.17); the following remarks can be outlined:

- at optimum incidence the diffusion factor lays in a range between 0.37 to 0.47

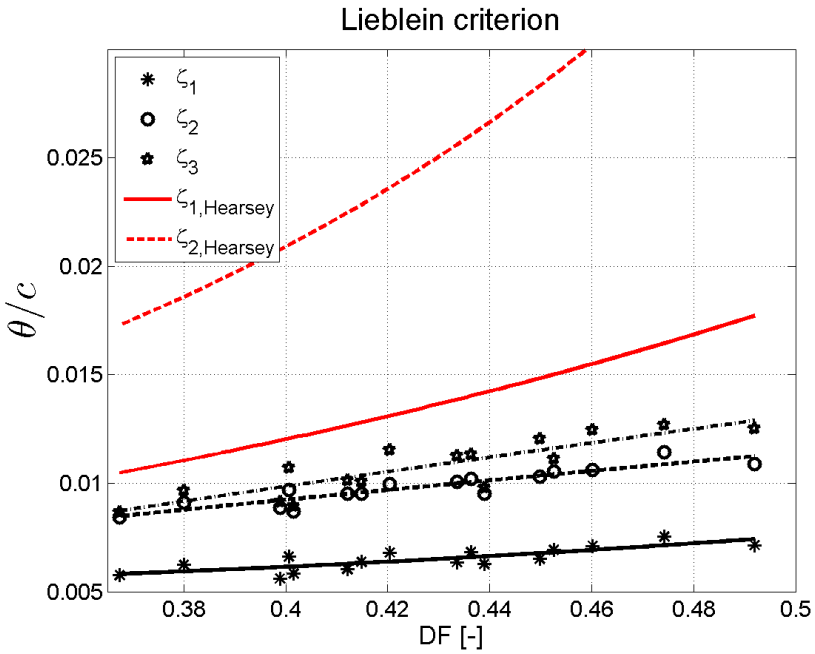

Figure 4.23: Lieblein Diffusion Factor

- the numerical data appear to fit the theory by Lieblein, even with some exceptions for very low solidity configuration.

- the computed results present a good agreement with the experimental data from Lieblein, here reported in Figure 2.10.

- the parameter ζ_1, which is the easiest to compute and also the one with the highest degree of approximation, appears to underestimate the losses.

- the AVDR, taken into account just by ζ_3 parameter, plays an important role in losses behaviour; the error committed using the efficiency forecasts based on ζ_2 increases while lowering the chord to pitch ratio.

- the empirical correlation for ζ_1 suggested by Hearsey seem to overestimate the paramter: the shapes of the curves corresponds to the computed results but the value is too high, in disagreement also with Lieblein's data.

- considering the reported correlation for ζ_2, from Hearsey, as well, the discrepancies both with computed data and Lieblein's results appear to be very strong, suggesting that the exponential law used by the author is not adaptable to every kind of cascade.

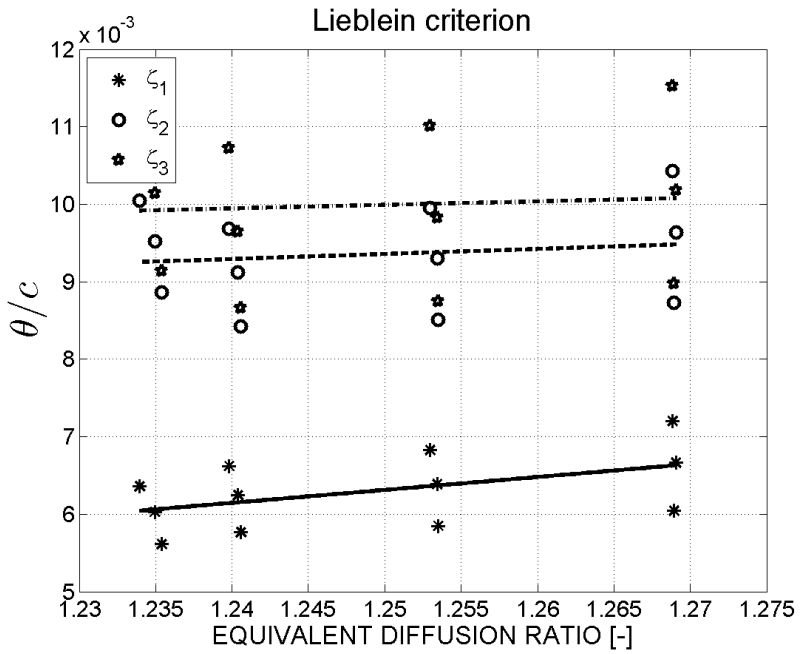

Figure 4.24: Lieblein Diffusion Ratio

Lieblein suggests also to look at the momentum thickness in function of an equivalent diffusion ratio; at minim losses incidence it can be defined follows:

$$D_{eq} = \frac{V_{1m}}{V_{2m}} \left[1.12 + 0.61 \frac{\cos^2 \alpha_1}{\sigma} \frac{V_{1t} - V_{2t}}{\overline{V_m}} \right]$$

the behaviour of the losses in respect to this parameter is reported in Figure 4.24. The results, even if they spot in a limited range of D_{eq}, are coherent with experimental data from Lieblein, increasing while the diffusion ratio is increasing.

Off-design performance Considering the whole incidence range tested, it could be of some interest to look how the parameters behave off design condition. The plot in Figure 4.25 shows, for instance, the trend of the ζ_3 parameter to estimate the momentum thickness versus the diffusion factor. Two main remarks can be outlined from the plot:

- the three different curves correspond to three different Mach numbers
- for low values of diffusion factor, the losses increase presenting a minimum condition which varies in function of Mach number

Globally, however, the computed behaviour seems to be coherent with the design condition, suggesting that the validity of the Diffusion factor model for estimate

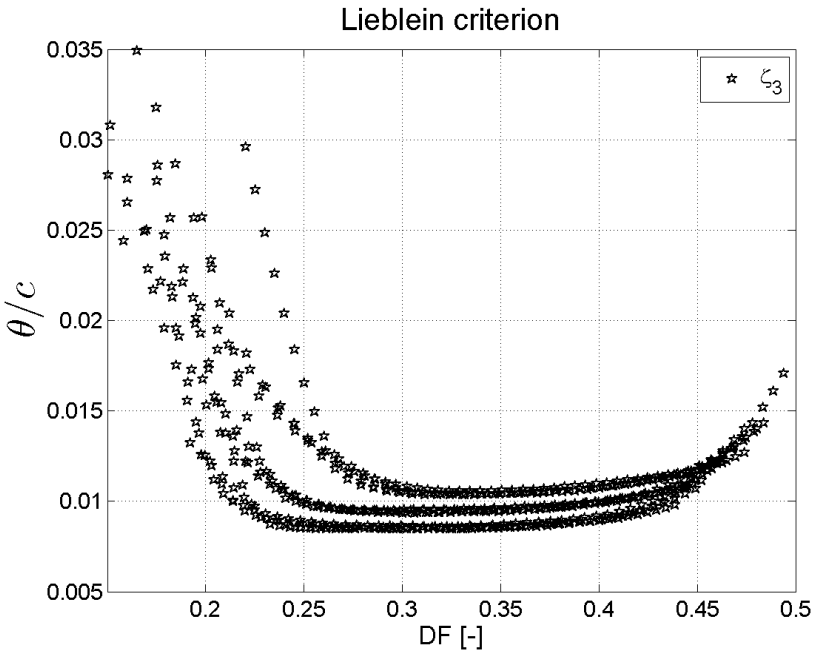

Figure 4.25: Lieblein Diffusion Factor - Off design

loss can be extended to a wider range of incidence; for the tested cascade this range can be assumed to start from $i = -4.5°$ until last computed incidence before stall.

4.5 Comparison between variation in chord and variation in pitch to achieve the same solidity

An objective of the present work was the assessment of the effects of solidity through a variation in chord with respect to a variation in pitch. As presented in chapter 2, in most of the solidity effect investigations performed in the past, the pitch to chord ratio has been usually varied through a variation in pitch, namely in the number of blade. As a matter of fact, the variation in chord presents some additional factors to consider during the analysis. Recalling the definition of the Reynolds number for an aerofoil:

$$Re = \frac{v \cdot c}{\nu} \tag{4.1}$$

where v is the inlet velocity, c is the chord of the profile and ν is the kinematic viscosity, it can be noticed that a modification in chord is affecting a parameter which can play a crucial role in determining the behaviour of the flow, as briefly addressed in section 2.3.5. In the present analysis the maximum reduction in

chord reaches the 30% of the baseline, but this variation does not seem to affect the Reynolds number significantly, which remains constant and does not show transition problems.

From the numerical point of view, as the mesh is automatically generated by the software Autogrid5^{TM} , a change in the blade to blade design, such as a reduction in chord, affects the mesh of the domain; while the topology setting remains constant in terms of number of cells in each block, the cell size changes, as a consequence of the blade resizing. From one side this behaviour permits to adapt the mesh to the reduced scale of the physical problem but, on the other side, could prevent the compatibility of the results due to the mesh refinement coming from the rescaling. The mesh sensitivity analysis showed in section 3.7 guarantees that, at zero incidence condition for $M_1 = 0.5$, both local and global performance are not affected in a measurable way by a mesh refinement in the blade to blade plane. Hence if some differences appear in the performance between configurations presenting the same solidity with different combination of chord and pitch, they could be due to a different physical behaviour. This comparability condition, however, is not guaranteed in other incidence and Mach conditions, whereas the mesh differences can cause a difference in the performance which exceeds the threshold set by the uncertainty of the measurements. Moreover it is given the possibility that the same performance in terms of local and global quantities is the result of two different behaviours of the cascade, hence it appears interesting the verification of this condition.

4.5.1 Results

In terms of incidence range no difference can be noticed between the computation presenting the same solidity: on both negative and positive incidence sides the limit assumes the same value.

Turning

In terms of turning, the difference registered between the configurations is always below the least measurable value of 0.3°at midspan. Considering a different spanwise location, 5% of the blade height, for instance, even if the slope with respect to incidence decreases, the absolute value of the turning difference is measurable: the percentage difference reaches for the lowest solidity at highest incidence the value of 2%, exceeding the threshold value of 0.3°from $i = -3.8°$ and $i = 3°$ respectively for $\sigma = 0.95$ and $\sigma = 1.1$. In this section the Mach number does not appear to influence significantly the different behaviour in term of turning.

Diffusion Factor

While considering different configurations of chord and pitch presenting the same solidity, the difference in terms of diffusion factor computed at midspan does not always present a clear trend with respect to incidence; while in the

middle range of incidence a linear relation can be outlined, some irregularities are present assessing the ends of the curves, for every condition of mach number and solidity. The difference value usually lays below 1.6% decreasing while inlet Mach is increasing and solidity is increasing. In every condition the diffusion factor computed varying the chord is higher. Looking at the value integrated on the whole section, the same irregularities can be noticed for higly negative and positive incidence, even if between $i = -4°$and $i = 2.5°$the difference between the computation appear to be constant and below 0.1%, in the whole range of incidence, however, the difference does not exceed the value of 1%. It is interesting to note that, compared to the midspan value, the global one presents an opposite behaviour respect both solidity and Mach number and at low solidity and low Mach number the configuration with increased pitch presents a higher value. At 5% of the blade height the differences are more stressed, reaching occasionally the 5%, usually presenting a stronger variation with Mach number in respect to the midspan quantity for all the solidity configurations.

Losses

The differences in terms of losses are not measurable for both midspan and integral performance, however some trends can be outlined in the slightly different behaviour of the configurations. Considering the value at midspan the variation in chord always determines lower losses and a decrease in solidity and Mach seems to favour this behaviour; for $M_1 = 0.45$ and $\sigma = 0.95$, the relative difference reaches the value of 34%, but its strong dependence on solidity and Mach makes it quickly reduce while increasing these parameters, laying between 5% and 20% in the greatest part of conditions and configurations tested. In the incidence range the absolute difference remains almost constant for all the solidity and Mach number of interest. The difference in terms of integral value seems less influenced by the Mach number, but presents a linear trend with solidity; the relative difference however is considerably lower than the local value, never exceeding 11%. Considering a section at 5% of the blade height two important remarks can be outlined:

- the relative difference appears to reach high values (50% in some configurations)
- the Mach number does not affect significantly the losses in any configuration

Hence, even if globally the losses are not significantly affected by the different choice of varying solidity through the pitch or trough the chord, it appears of some interest to investigate the differences remarked at different blade height which could imply a different development and distribution of the losses on the outlet surface. In Figure 4.26 the comparison between the losses distribution is shown for two different configurations of chord and pitch presenting $\sigma = 0.95$

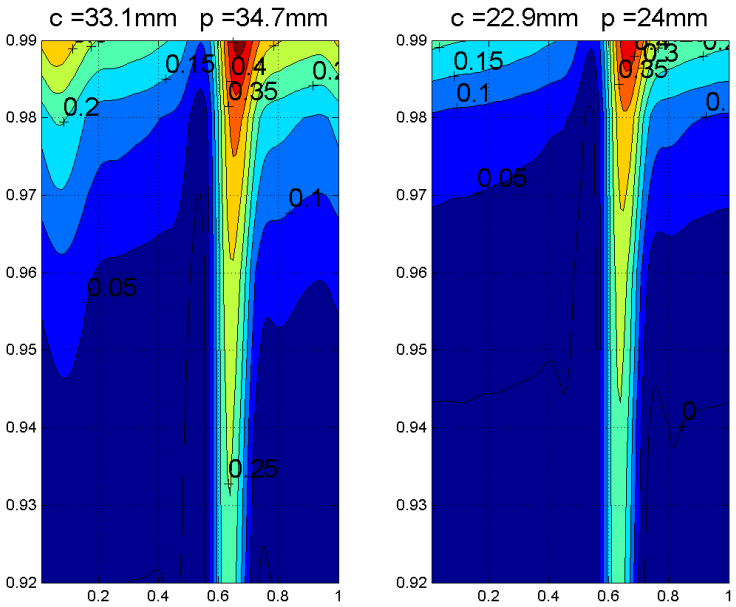

Figure 4.26: Comparison between the losses distribution for different configurations of chord and pitch presenting the same solidity near to end wall boundary; $M_1 = 0.41$, $i = -4.42°$

near to the end wall boundary. It can clearly be seen that the plot on the left side presents a higher peak value and extended regions characterized by higher losses, has a consequence of a different development of the end wall boundary layer. This is probably due to the different geometry of model: the configuration with reduced chord present an inlet surface which is nearer to the leading edge, hence the boundary layer is less developed. Some differences can be observed also in the development of the wake which is usually slightly wider in the increased pitch configurations, for which it can also be noticed a greater extension in the spanwise dierection of the regione where the losses reach the value of 0.25.

4.5.2 Conclusions

On the basis of the previous analysis, the following remarks can be outlined:

1. the performance at midspan and the global performance are not significantly affected by the different choice in chord and pitch, the main design parameters varying within a range which can be considered as a consequence of the different mesh used.

2. a different behaviour can be possibly outlined near to the end walls, where a pitch increase can cause stronger losses and a slightly higher diffusion

factor. This effect, however, is probably due to the different geometries used rather than to a Reynolds effect.

3. as far as concerns the set-up of the experimental test, a difference between the variation in chord and pitch does not affect the results in a measurable way.

4.6 Comparison between slip and no-slip end wall boundary condition

The main analysis has been conducted imposing no-slip boundary condition to describe the viscous flow as real as possible; some configurations (see Table 4.2), however, have been tested imposing on the end-wall boundaries a slip condition, that is, as described in section 3.5, a condition of inviscid flow. A comparison between the two solutions can give a hint on the effect of the end-wall boundary layer development on the performance at midspan and then on the role of three-dimensional effects on the 2D behaviour of the cascade. A $\kappa-\varepsilon$ turbulence model in the formulation by Yang-Shih is used for this investigation. A full comparison between this turbulence model and the Shear Stress Transport model presented above is reported afterwards.

The first observation which can be outlined is a different extension of the incidence range, usually wider for the slip condition. With the exception of the baseline, the test with slip boundary condition can usually reach higher positive incidence, exceeding of 3°for solidity equal to 0.95 and 0.66. This means that, for high incidences (both positive and negative) that stall is triggered by end-wall boundary layer separation.

In terms of turning there are no effects on the midspan performance considering the two different formulations, for all the solidities tested, in the whole range of incidence and Mach number imposed. Considering the mass-averaged value along the pitch at 5% of the blade height, however, some differences can be remarked, specially at high incidence; while imposing the no-slip condition, the

SOLIDITY			**PITCH** (mm)	
VALUES			24	34.67
			100%	*69.2%*
CHORD	33.09	*100%*	**1.38**	**0.95**
(mm)	22.91	*69.2%*	**0.95**	**0.66**

Table 4.2: Configurations investigated with slip boundary condition

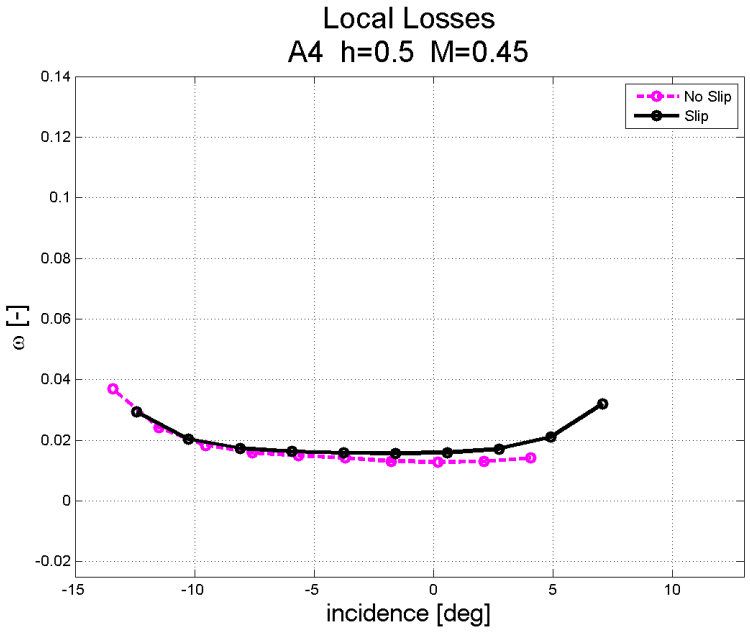

Figure 4.27: Comparison between local losses at midspan between slip and no-slip condition

turning appears to be lower, this effect increases as the solidity is decreasing.

Looking at the diffusion factor a slight discrepancy occurs both at midspan and near to the end wall; the slip condition always predicts a higher diffusion factor with a constant difference in the whole incidence range and independently from the Mach number.

The Losses behaviour appears to be of great interest because. At midspan (see Figure 4.27) no meaningful disagreement can be remarked, even if the values appear to be slightly lower with the no slip condition. At 5% of the blade height, as expected, the boundary layer presence enhances whole loss curves shift considerably, specially at high incidence: while with slip condition the behaviour of the losses is the same at midspan, presenting a large flat zone in the incidence midrange, the no-slip boundaries imply a shift in the minimum loss incidence towards the negative losses and an increased slope going towards stall incidence as shown in Figure 4.28. The difference is stronger at low mach number and low solidity. The different behaviour near to the end wall boundary could explain the remarked difference in the incidence range: the reason of the positive incidence computable limit relies in the development of the corner separation which is mainly caused by the behaviour of the end wall boundary layer. Then it can be expected that the limits of the numerical analysis in terms of maximum incidence reachable could be partially overcome within the experimental analysis, where the measurements can be performed even in presence of strong separation.

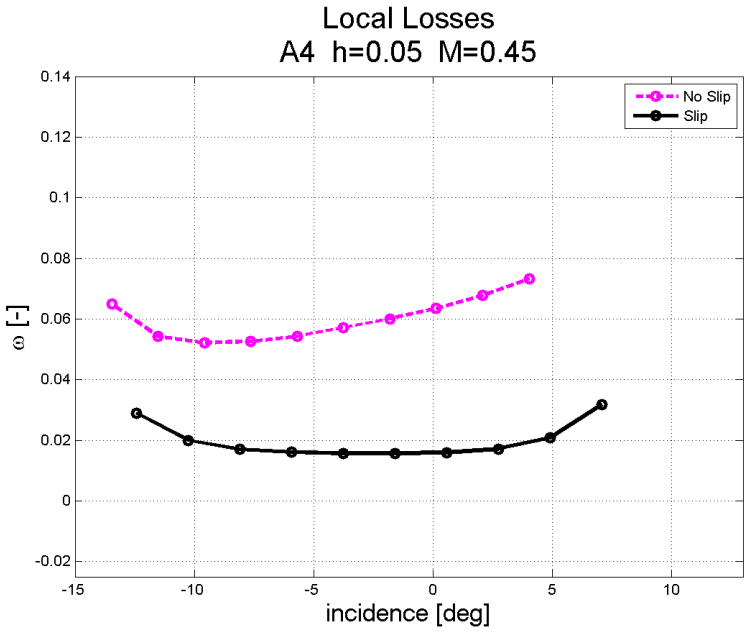

Figure 4.28: Comparison between local losses at 5% of the blade height between slip and no-slip condition

4.7 Turbulence model comparison

4.7.1 Global and local performance in the whole incidence range

The first difference between the tested turbulence models concerns the extension of the incidence range: SST shows the most limited range of incidence, exhibiting early convergence problems on both positive and negative side of the interval. As shown before the $\kappa-\omega$ model shows good convergence up to an incidence $i = -7.4°$, while the other two models allow to reach $i = -13.4°$ without any problem. It must be said also that on the negative side the angle of attack has been limited a priori to the range of interest but the possibility of investigating lower incidences is not expected to show convergence problems within reasonable limits. The last computable value is not expected to vary noticeably with solidity as well, but it appears that the stall margin is slightly reduced using the SST turbulence model. Even if these considerations quantitatively depend on the discretization of the incidence range, the increased sensitivity of the $\kappa-\omega$ to the irregularities of the flow is clearly detectable in the present analysis.

Turning

Considering the mass-averaged value at midspan, the turning predicted by the three different turbulence models does not present consistent variations; usually

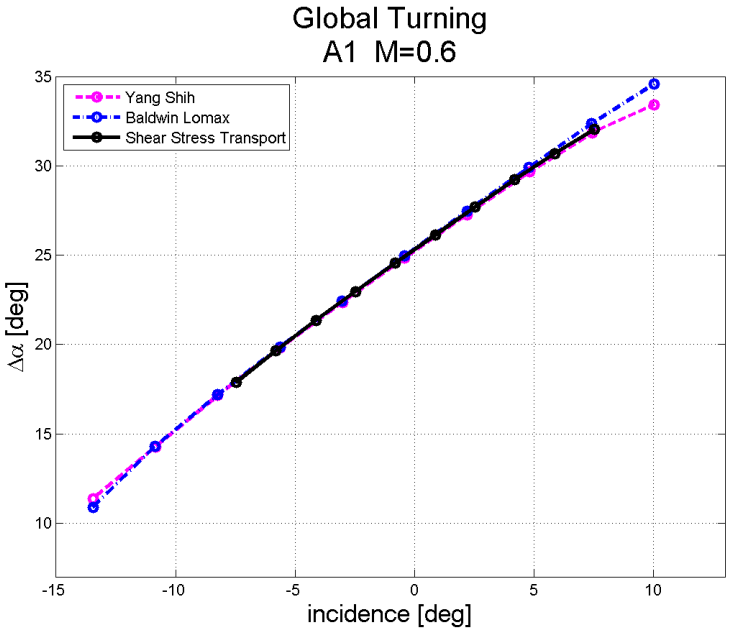

Figure 4.29: Comparison between integral turning prediction with different turbulence models

the results from Baldwin Lomax slightly exceed the prediction of the other two models, perfectly overlapped each other: this small difference is more noticeable at very high and very low incidences, specially increasing the Mach number. Considering a section at 5% of the blade height, a good agreement between the three turbulence models can be observed in a great part of the incidence range, from the first negative incidence to 60% of the last available value; approaching the stall condition the difference became more stressed: the $\kappa - \varepsilon$ model presents a stronger underestimation of the turning, while BL and SST remain in agreement until 75% of the stall margin, SST underpredicting the quantity at higher incidence. The integral value presents a similar behaviour, but the differences are barely noticeable (Figure 4.29).

Diffusion Factor

Some differences in term of diffusion factor can be observed at midspan between the three models, specially when the Mach number is increasing: Baldwin Lomax always predicts higher values in the whole range of incidence. The predict from SST are slightly lower while Yang Shih reports the lowest values; as for the turning, the differences are more visible in the last 25% fraction of the incidence range and they increase going towards stall. Considering the integral quantity, the predictions overlap almost perfectly. Near to end wall boundaries specially at

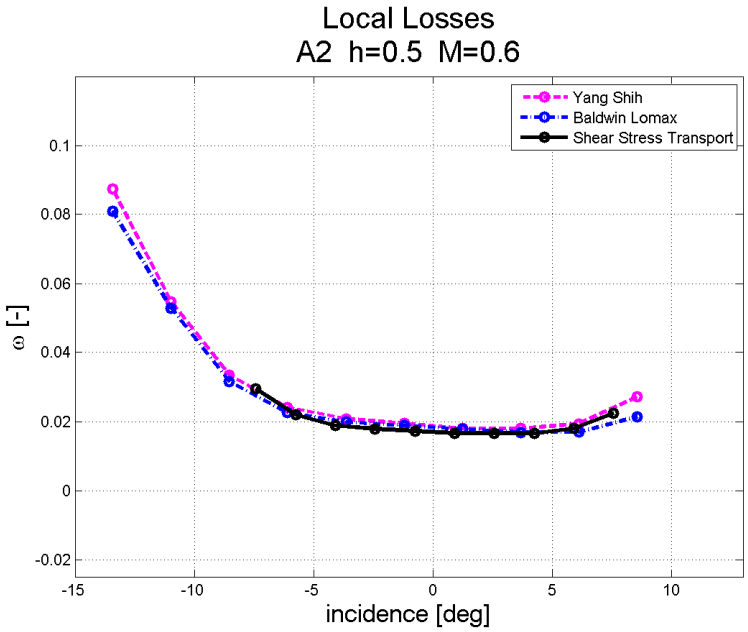

Figure 4.30: Comparison between local losses at midspan prediction with different turbulence models

low incidence the Baldwin Lomax turbulence model tends to underpredict the diffusion factor.

Losses

The turbulence model choice appears to be a critical aspects under the profile of the loss prediction. Considering the performance at midspan (Figure 4.30). it can be noticed not only a difference in the value prediction, but also in the shape of the curve in respect to incidence: considering the typical behaviour of the losses, previously shown in this chapter, the flat zone predicted by the SST model appears to be less extended than the others predicting a raise respectively for higher negative and positive incidences. Regarding the YS model in respect to BL prediction, it can be said that the increase for highest positive and negative incidences are more marked. The YS prediction are always higher than the others, specially increasing the Mach, while SST usually presents the lowest values, with the exception, as said, of the ends of the curves, where Baldwin Lomax tends to underpredict the dissipation. The variation in solidity does not seem to affect the difference in the behaviour of the models. As far as concerns the integral values the prediction by Baldwin Lomax and Shear Stress Transport are always overlapping but on the last reachable incidence, where the YS model predicts higher losses. the overprediction of Yang Shih results is higher than at midspan,

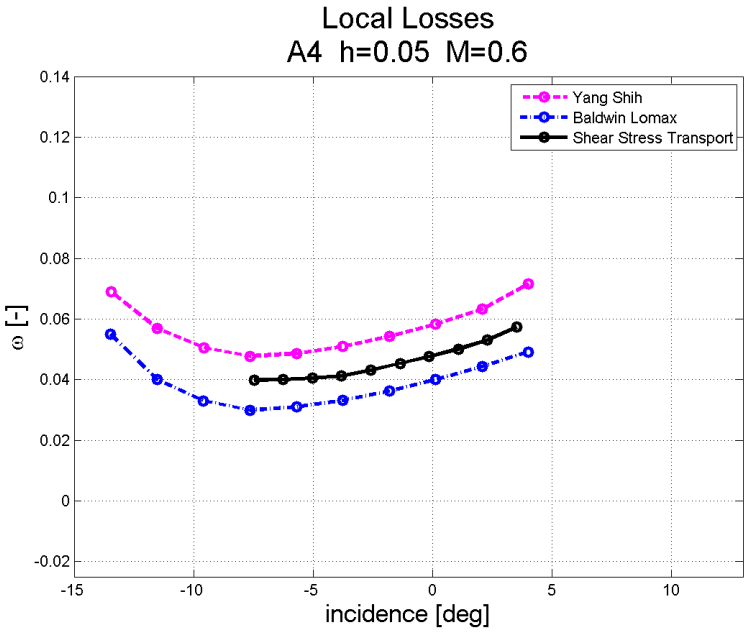

Figure 4.31: Comparison between local losses at 5% span prediction with different turbulence models

the difference being always above 5E-3; considering the absolute value of the dissipation, this gap is very high. It is interesting to observe that at 5% of the blade height the disagreement in the predictions varies with solidity: while at high solidity the Baldwin Lomax and the SST models provide overlapping results, being both lower than Yang Shih, decreasing solidity the difference between SST and BL raises, as the first progressively predicts higher losses. On the contrary of what happens at midspan the shape of the curve versus incidence has the same shape varying the turbulence model: YS and BL curves are always parallel.

4.7.2 Effect of the turbulence model in choke condition

The first noticeable effect of the turbulence modelling at choke condition regards the different incidence limits reachable by the different models: the SST shows convergence problems starting from around $i = -10.4°$in some specific condition of Mach number, while BL and YS models do not present any problem at least until the negative value $i = -13.4°$ which represents the least value of incidence of interest for the present analysis, hence further values have not been tested.

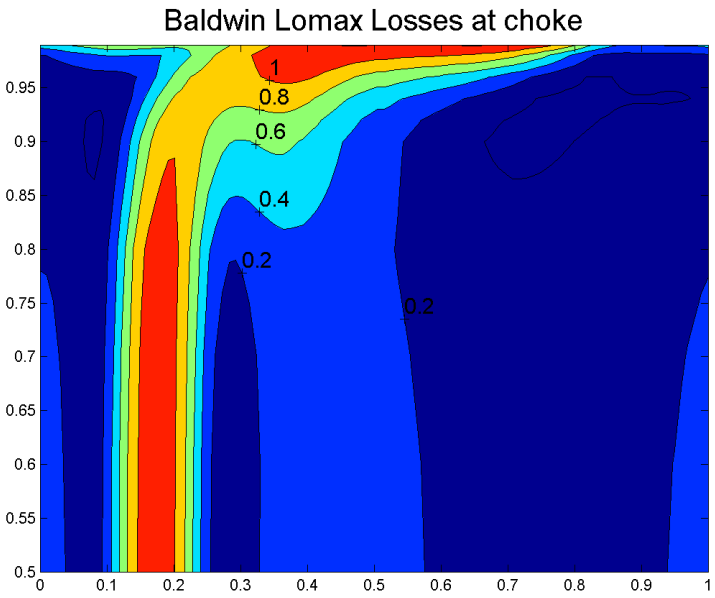

Figure 4.32: Baldwin Lomax prediction of Losses distribution on the outlet plane; $i = -13.4°$, $M_1 = 0.65$, $p_{01} = 154\ kPa$

Highly negative incidence

The results computed for $i = -13.4°$ must be considered very carefully, as the steady model used for the present computation is probably brought to its limit and the accuracy and reliability of the results are strongly questionable.

Considering the distribution of the losses on the outlet plane, here represented in Figure 4.32 and 4.33, some remarkable differences can be noticed:

- the Baldwin Lomax model describes a more narrow wake, characterized by loss coefficient which reaches the unitary value, while YS is limited at 0.8.
- Yang Shih describes a wider, more diffused, wake.
- according to Yang Shih prediction, the flow is characterized by a small (around 20% of the surface) low dissipation section; going towards the wake the losses gradually increase presenting, in an area between -15% and +15% of the blade height, a local maximum at a distance around 20% of pitch (indicated by the circle marker in the picture); between this section and the wake there is again a low loss area. Baldwin Lomax describes a wider central zone characterized by losses reaching a higher minimum value which apparently increases with a slightly higher gradient approaching the wake.

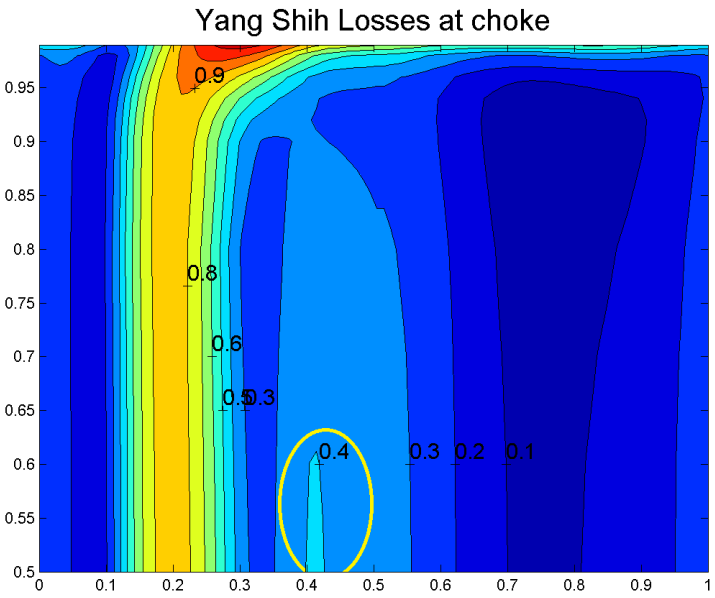

Figure 4.33: Yang Shih prediction of Losses distribution on the outlet plane; $i = -13.4°$, $M_1 = 0.65$, $p_{01} = 154\ kPa$

- the trace of the corner vortex is more intense in the Baldwin Lomax results and it is also more spread on the end wall.

Also looking at the Mach number distribution on the blade to blade plane at midspan, reported in Figure 4.34(a) and 4.34(b), considerable disagreements show up in the description of the fluid behaviour. The shockwave affects the whole section of the channel according to the $\kappa - \varepsilon$ model, while Baldwin Lomax describes a less critical behaviour, where the same phenomenon takes place in a smaller region of the channel, near to the convex surface of the blade. The acceleration on the front part of the blade seems to be underpredicted by the zero-equation model, as well, hence the behaviour of the boundary layer presents remarkable difference, its growth on the pressure side being overestimated and causing a recirculation area situated right after the nose of the blade. This behaviour does not match with the other model, probably due to the position and the characteristics of the shockwave after the leading edge which seems to reattach the flow to the blade. The two equation model forecasts an opposite interaction with the shockwave on the suction side which promotes the separation of the flow and determines a recirculation area before the trailing edge; this phenomenon is totally neglected in Baldwin Lomax results. The overall result is that while YS predicts chocking, this is not predicted by the BL.

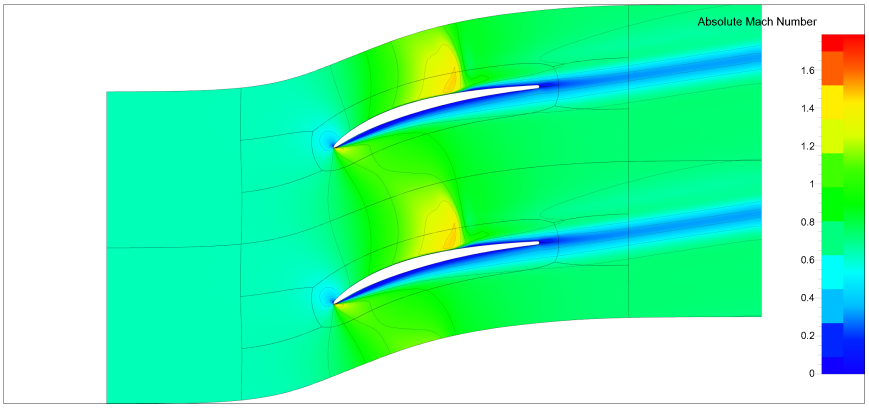

(a) Baldwin Lomax

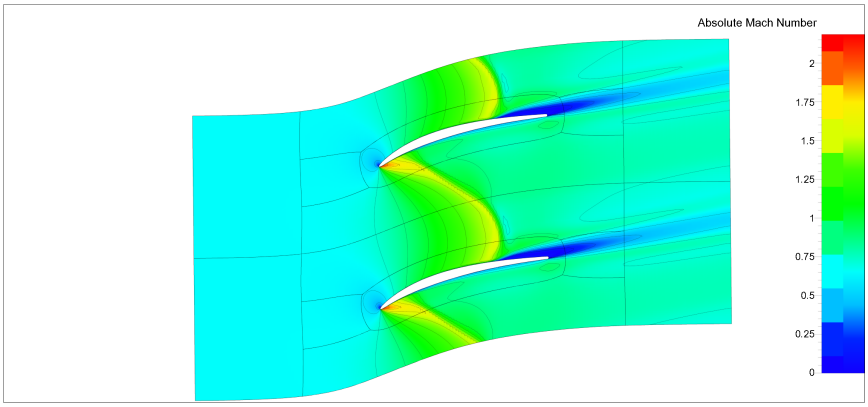

(b) Yang Shih

Figure 4.34: Mach number distribution on the blade to blade plane at midspan; $i = -13.4°$, $M_1 = 0.65$, $p_{01} = 155\ kPa$

Choke condition

The Figure 4.35 shows the comparison between the different distribution of Mach number on the blade to blade plane at midspan predicted by the different turbulence models for $i = -7.4°$, which is the limit incidence for SST model. The following remarks can be outlined:

- Unlike the condition $i = -13.4°$ the main behaviour of the flow is roughly characterized in the same way by the three models, even if the topology of the flow is not identical.

- two weak shocks are captured by all the three models; one starts from a point on the intradox 10% of the chord after the leading and parallel to the direction linking the nose of one blade with the tail of its adjacent, the other from a point around 25% chord before the trailing edge directed towards the tail of the other blade

- A strong normal shock, joining the transversal one previously described, is registered in all the three simulations. While Baldwin Lomax foresees its position around 25% upstream of the trailing edge, in both YS and SST computations it lays at a distance around 10% of the chord. The shock is extended through the whole channel (excluding the boundary layers), but the flat surface of the area characterised by the higher compression varies from almost the 35% of the passage in BL results against the 12% registered by both the two equations models. The acceleration of the flow is less important in the zero equation model while reaching almost Mach 2 in the YS forecast and a slightly lower value for SST.

- The YS and SST models allow to capture a shock normal to the direction of the flow 10% of chord after the trailing edge; the shock is more remarkable and extended considering the SST model, where, after the first shock inside the passage the fluid accelerates to supersonic velocity and compresses again on the whole section; on the other side, the loss generated by the stronger first shock prevents the re-acceleration of a great region of the channel.

- the characteristics of the wake also change according to the turbulence model used: while Baldwin Lomax describes a strong narrow wake inside which strong recirculation areas are present reaching locally considerable values ($M \simeq 0.4$), the other two models show a thicker wake gradually energized by the main flow. It can be observed for YS that the acceleration of the wake is widely spaced than for SST. YS predicts a higher dissipation rate.

The distribution of the loss coefficient on the outlet plane is presented in Figure 4.36. In 4.36(a) and 4.36(b) are clearly noticeable the trace of losses due to the

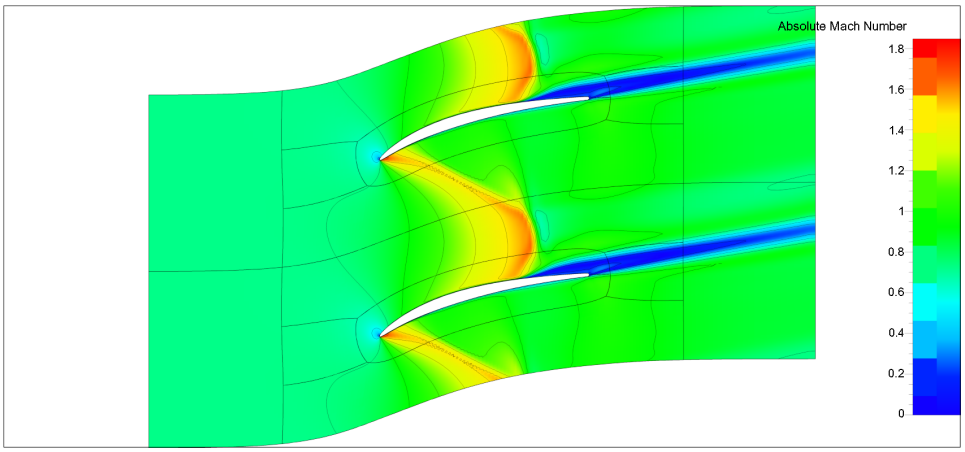

(a) Baldwin Lomax

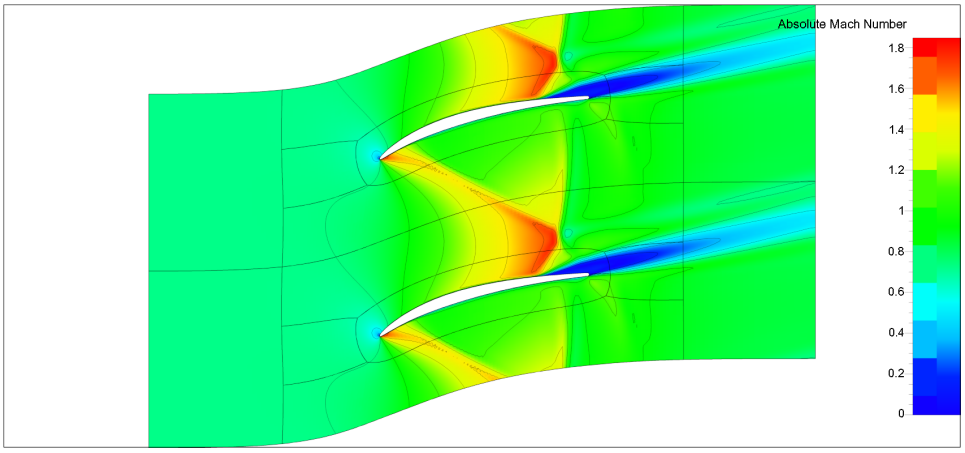

(b) Yang Shih

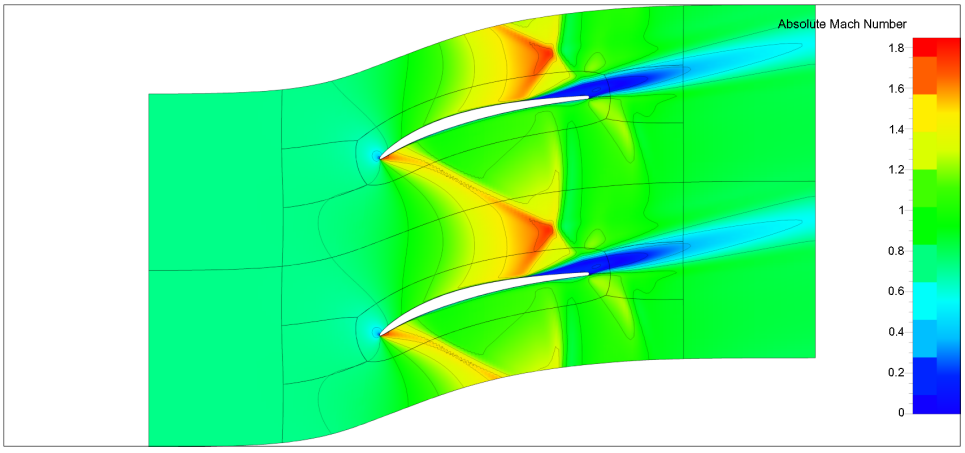

(c) Shear Stress Transport

Figure 4.35: Mach number distribution on the blade to blade plane at midspan; $i = -7.4°$, $M_1 = 0.73$, $p_{01} = 165\ kPa$

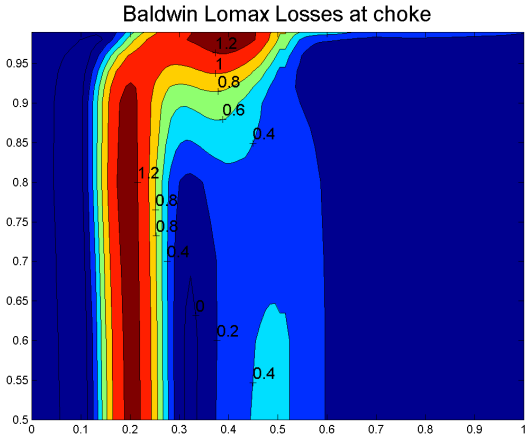

(a) Baldwin Lomax

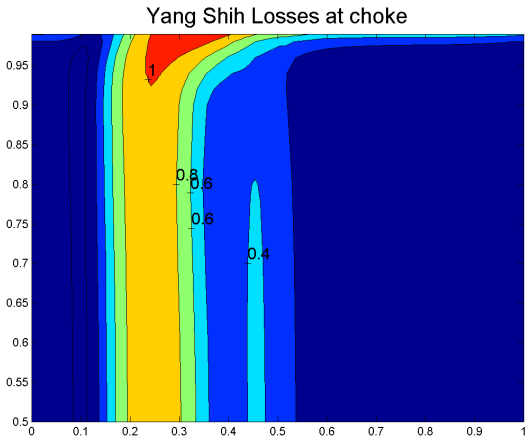

(b) Yang Shih

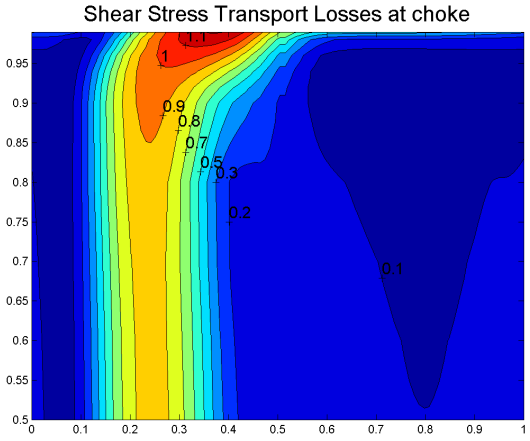

(c) Shear Stress Transport

Figure 4.36: Pressure loss coefficient on the outlet plane; $i = -7.4°$, $M_1 = 0.73$, $p_{01} = 165\ kPa$

shock inside the passage, which is not present in the SST results; this is probably due to the fact that, according to SST predictions, the shock is less intense. As outlined before, the intensity of wake is higher for the zero equation model, while the other two present a more diffused one. The losses on the secundary surface appear to be more redistributed in the results of the SST model, which presents a more gradual increase going towards the core of the wake. On the convex side of the blade, after the maximum thickness section, a wide recirculation area develops in the corners with hub and shroud surfaces. The trace of this corner separation is outstandingly different, more intense and extended with a circular shape according to Baldwin Lomax results, barely noticeable in YS prediction. SST turbulence model predicts an intermediate behaviour.

4.7.3 Effect of the turbulence model in stall condition

Looking at the different Mach number distributions on the blade to blade plane at midspan according to the three different models reported in Figure 4.37, it is possible to see that the turbulence model heavily affects the results in this condition. The following remarks can be outlined:

- Unlike in choke condition, the inlet Mach number varies even if the imposed pressure is the same. This variation is present in the whole Mach range tried, but is more noticeable after $M > 0.6$.

- The Baldwin Lomax model describes a recirculation zone on the suction side which is almost extended to half of the channel and it is characterized by a core with high upstream directed velocity.

- The supersonic bubble on the suction side after the leading edge is barely noticeable in BL results, while it is more intense and widely extended using the other two models, specially in SST computations.

- The separation on the suction side after the shock following the supersonic bubble develops differently according to YS and SST, probably due to the different description of the upstream phenomena: while for the first one the fluid detaches abruptly some percentage of chord after the shock on the nose and the separation area reaches a maximum thickness extended to one fifth of the channel, the second one describes a progressive growth of the boundary layer which maximum extensions in the pitchwise does not exceed some percentage of chord.

- The development of the wake is a consequence of the previously described phenomena: it is wider for BL turbulence model, characterized by a redistribution of the losses on the outlet plane; the YS model forecasts a thinner wake characterized by a high intensity core. In SST results the re-energization of the wake is maximum and the wake is weaker.

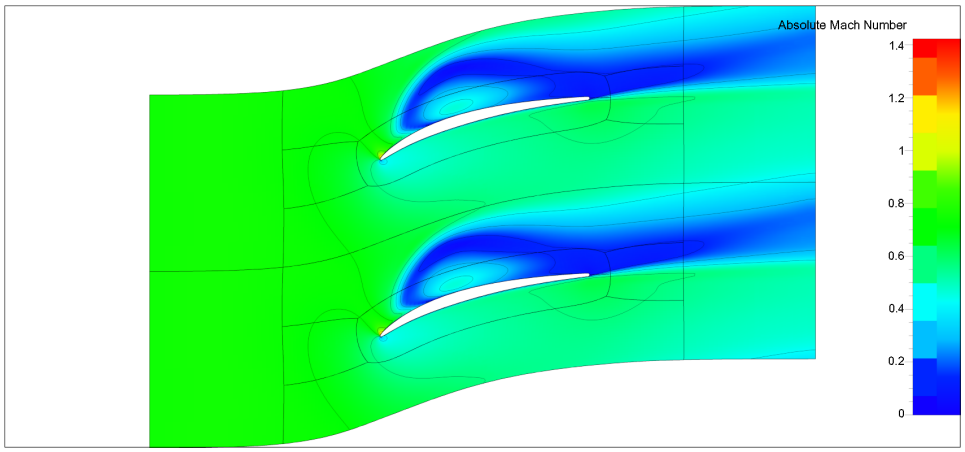

(a) Baldwin Lomax, $M_1 = 0.759$

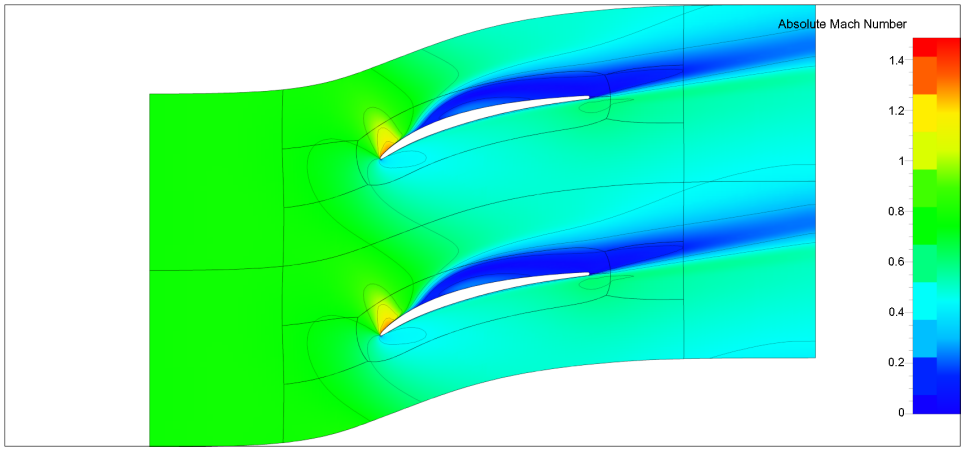

(b) Yang Shih, $M_1 = 0.780$

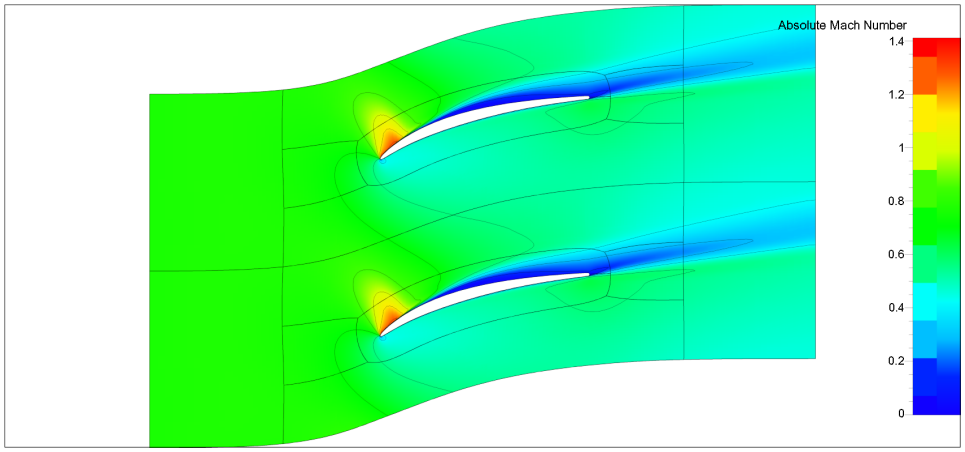

(c) Shear Stress Transport, $M_1 = 0.767$

Figure 4.37: Mach number distribution on the blade to blade plane at midspan; $i = 7.6°$, $p_{01} = 125\ kPa$

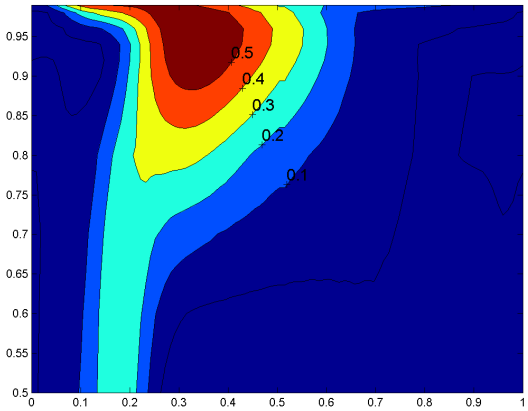

(a) Baldwin Lomax

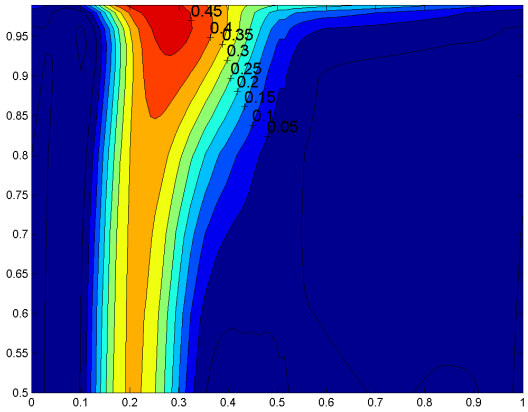

(b) Yang Shih

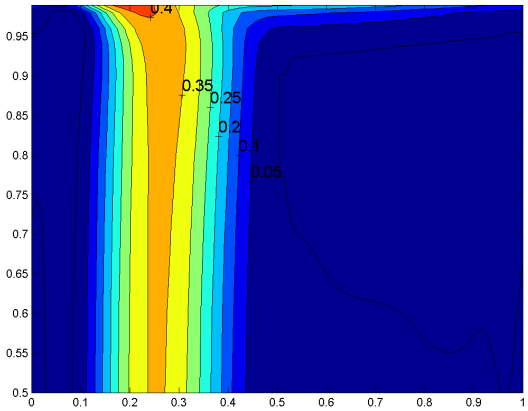

(c) Shear Stress Transport

Figure 4.38: Pressure loss coefficient on the outlet plane; $i = -7.4°$, $p_{01} = 125\ kPa$

Looking at the losses distribution on the secondary plane (Figure 4.38), it is possible to better visualize the behaviour of the wake at midspan and analyse the track of the corner separation. While in BL and YS results a round loss spot is present, more extended and intense in the first one, the loss distribution along the spanwise direction for SST turbulence model does not present significant variation, unless for a slight interaction with the boundary layer near to hub and shroud.

4.7.4 Conclusions

Considering the comparison between the turbulence models used for the present analysis, the following remarks can be outlined:

- the turbulence model influences the extension of the computable incidence range: while the shear stress transport analysis is limited on both choke and stall side, both YS and BL model present convergence problems only near to stall and it was not possible within the present investigation to find a highly negative incidence limit.
- considering the performance at midspan in a Mach range between 0.45 and 0.6, the difference in terms of turning and diffusion factor are usually noticeable near to choke and near to stall.
- the loss computation always leads to very different results, even without pushing the inlet conditions.
- the BL model does not describe properly the behaviour of the flow, specially at highly positive and negative incidence. In general this model appears to underestimate the intensity of the phenomena.
- the flow topology predicted by the two-equations models is usually similar even if the intensity of the phenomena is usually differently assessed.
- the difference between the turbulence models is usually analogous for different solidity configurations. However, considering the losses near to the end walls boundaries in respect to solidity, A smaller slope is registered according to the SST turbulence model.

The strong sensitivity of the calculations with respect to the turbulence model has been showed; the present investigation confirm the expectation on the low accuracy of BL results. As far as concerns the two-equations models, even if one can say that SST seems more sensitive to the imposed conditions and to slight flow behaviour modifications, it is necessary to wait for the experimental results to express a proper judgement on the accuracy of the results.

Chapter 5

Conclusions

5.1 Summary

The design of newer environmental friendly and silent engines requires the validation of new architectures and concepts involving outstanding mechanical and aerodynamic challenges. As far as concerns the design of the axial flow compressor, it appears of great interest the study of the solidity effect on the compressor performance and stability because of its link with the number and the size of the blades. According to a preliminary analysis, performed on a numerical model of 1.5 compressor stage, a reduction in solidity could allow to achieve a considerable engine weight reduction without afflicting substantially the performance, although reducing the incidence range. The assessment of the solidity effect is performed through a numerical analysis thanks to the computational fluid dynamics software FINE/Turbo^{TM} produced by NUMECA International. The behaviour of a linear cascade is studied to obtain the loss correlation in the Mach number range of interest ($M_1 \in [0.45, 0.6]$) for a specific profile, designed by the Belgian company TechspaceAero. As an experimental analysis will be performed as well, a second objective of the numerical investigation is then to foresee the main behaviour of the cascade to design a proper set-up of the tests.

Firstly the numerical model has been set up, assessing the effect at design conditions of some mesh parameter on the performance. The values of minimum cell size on both blade and hub and shroud surfaces, the discretisation on the blade to blade plane and in the spanwise direction have been chosen to maximize the accuracy of the results in agreement with the computational effort requested by the great number of computations to perform. On the final mesh, the following turbulence models have been tested: Baldwin Lomax, Spalart Allmaras, Yang Shih, Launder Sharma, Shear Stress Transport; the independence of the behaviour of the model from the imposed turbulence intensity has been assessed, as well.

Then, the cascade map has been computed from choke to stall in a Mach number range between $M_1 = 0.3$ and $M_1 = 0.8$ where possible. Eight combinations of pitch and chord have been analysed, to assess five different values of

solidity. The study has been carried out with three different turbulence models: Baldwin Lomax, Yang Shih and Shear Stress Transport, after having eliminated the Spalart Allmaras (SA) and LS in a preliminary phase.

The linear trend of losses with solidity has been confirmed, but no minimum condition showed up in tested range of solidity, confirming the expectation of a minimum condition for lower values of solidity, which usually corresponds to conditions out of interest. The decrease of stall margin has been confirmed, as well, showing again a linear trend.

The results have been compared with the literature data, showing good agreement in terms of deviation prediction with Lieblein correlation. In terms of losses the data show good agreement with Lieblein correlations in function of diffusion factor, while considering the equivalent diffusion ratio proposed a dependence with the inlet Mach number, firstly neglected by Lieblein but already suggested by Hearsey, has been confirmed, together with the evaluation of the different possible parameters coming from the literature. The possibility of extending the correlations out of the minimum loss condition has been verified and confirmed within a limited range of incidence.

The achievement of the certain solidity through a different combination of pitch and chord has been investigated; no substantial difference is observed considering the performance averaged on the whole outlet surface and along the pitch at midspan, but the behaviour of the flow , specially in terms of corner separation is different, due to the slight change in the cascade aspect ratio.

A comparison has been performed imposing slip and no-slip condition; while the performance at midspan are not significantly affected by this boundary condition choice, appears of great interest the reduced incidence range of no-slip computation, where the corner separation appears to play a main role in the determination of the limit of the numerical model. Another possible consequence of this observation is that the maximum incidence reachable by the experimental cascade, will probably be higher.

The complete map of the cascade has been assessed through three different turbulence models; the reachable limits of the incidence range are different and the computation of the losses show a certain disagreement. In a limited range of Mach number, excluding choke and stall incidence, the main design quantities do not show appreciable disagreement. The BL model has been verified to be inaccurate specially while approaching choke and stall condition. The performance of the two-equations models will be verified experimentally because it was not possible to formulate a proper final judgement within the framework of the numerical analysis

5.2 Future works

The present analysis will be developed towards three different directions, presented below.

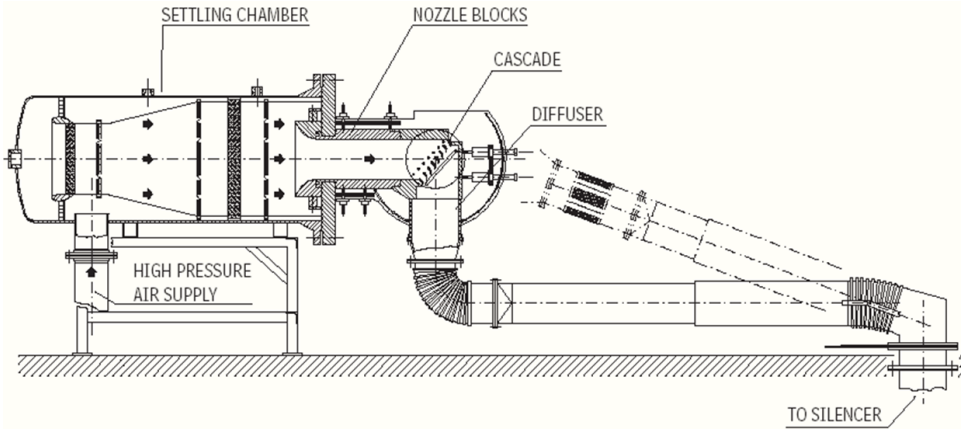

Figure 5.1: Schematic of VKI C3 high speed wind tunnel

5.2.1 Further development of the numerical model

As far as concerns the development of the numerical model, two different actions are planned:

Spalart-Allmaras model

It appears of interest to complete the assessment of the turbulence modelling effect on the current problem performing the analysis with the one-equation model by Spalart Allmaras. The characteristics of this model suggest that it could allow to reach accurate results with a smaller computational effort, compared with the two-equations models.

Profile variation

To guarantee a better comparability with the literature and increase the validity of the present investigation, the analysis will be repeated with Double circular arc and Multi-circular arc profiles.

5.2.2 Experimental validation

The numerical model will be validated through an experimental campaign in the C3 high speed wind tunnel at VKI. Figure 5.1 shows a schematic of the wind tunnel. The flow traverses the settling chamber through three mesh screens and two honeycombs, whose presence is intended to reduce turbulence. From there, the flow is guided through a convergent nozzle to the cascade. The latter is mounted on a rotating mechanism that can be easily turned to change the inlet flow incidence. Downstream the test section, the flow discharges to atmosphere via a diffuser.

Four configurations of pitch and chord will be tested corresponding to three different value of solidity. The performance at midspan will be analysed in a

Mach number range between 0.45 and 0.6 in the range of incidence from choke to stall.

5.2.3 Integration with design tools

As discussed in the first chapter, the solidity must be chosen very early in the design process but its choice is usually driven by the experience and sensitivity of the designer rather than proper optimization criteria. The most interesting development of the present work would be then, to formally express a relation useful for design purpose, even if a minimum loss condition is not available.

In this direction a first step is the integration of the solidity choice in a axial compressor design software solving Not Isentropic Simple Radial Equilibrium (NISRE) equations. Through the VKI developed Computer Aided Design and Optimization Tool for Turbomachinery Applications (CADO), a single objective optimization of a rotor solidity distribution along the span can be performed, parametrized by the maximum diffusion factor.

Notation

List of Symbols

α	Angolo assoluto del flusso
β	Angolo relativo del flusso
κ	Angolo del ferro
ϕ	Inarcamento del profilo
δ	Deviazione
ω	Coefficiente di perdita di pressione tot.
σ	Solidity
γ	Angolo di calettamento
Z	Numero di pale
ρ	Densità
c	Corda aerodinamica
s	Passo
i	Incidenza
t	Spessore della pala
M	Numero di Mach
p	Pressione
v	Velocità assoluta del flusso
ϵ^*	Deflessione di progetto secondo Howell
DF	Diffusion Factor
D_{eq}	Equivalent Diffusion Ratio
Ψ_a	Coefficeinte di Zweifel

Acronyms

VKI Von Karman Institute for Fluid Dynamics

NACA National Advisory Committee for Aeronautics

NASA National Aeronautics and Space Administration

CTRD Compressor and Turbine Research Division

DVL Deutsche Versuchsanstalt für Luftfahrt

RR Rolls Royce

GE General Electric

DREAM Validation of Radical Engine Architecture systems

ACARE Advisory Council for Aviation Research and Innovation in Europe

DCA Double circular arc

LP low pressure

DDOR Direct Drive Open Rotor

CFD computational fluid dynamics

IGV Inlet guide vane

GUI graphical user interface

DNS Direct Numerical Simulation

LES Large Eddy Simulation

RANS Reynolds Average Navier-Stokes

PDE Partial Differential Equations

MER Maximum Expansion Ratio

BL Baldwin Lomax

SA Spalart Allmaras

YS Yang Shih

SST Shear Stress Transport

LS Launder Sharma

AVDR Axial Velocity Density Ratio

TSA TechspaceAero

NISRE Not Isentropic Simple Radial Equilibrium

CADO Computer Aided Design and Optimization Tool for Turbomachinery Applications

Bibliography

[1] T. Obrecht. Hp compressor preliminary design. In *Advances in axial compressor aerodynamics*. 2006.

[2] J. Sans. The effect of solidity on compressor performance and stability. Technical report, Von Karman Institute for Fluid Dynamics, 2011.

[3] Sir C.A. Parsons. Turbo-compressor and pump. 710,884, October 1902.

[4] S. Lieblein, Schwenk F.C., and R.L. Broderick. Experimental flow in two dimensional cascades. In *Aerodynamic design of axial-flow compressor*, volume II, research memorandum VI. Cleveland, Ohio.

[5] C. C. Koch and L. H. Jr. Smith. Loss sources and magnitudes of axial compressors. *Journal of engineering for power*, 98:411–424, 1976.

[6] P.I. Wright and D.C. Miller. An improved compressor performance prediction model. In *Turbomachinery : Latest developments in a changing scene*, pages 69–82. Bury St Edmunds, UK, Mechanical Engineering Publications Ltd, 1991.

[7] A.R. Howell. Fluid dynamics of axial-flow compressors. In *Proceeding of the Institution of Mechanical Engineers*, volume 153, pages 441–452, 1946.

[8] A. D. S. Carter. The low speed performance of related aerofoils in cascade. Technical paper R.55, NGTE, September 1949.

[9] O. Zweifel. Spacing of turbo-machine blading, especially with large angular deflection. *The Brown Boveri Review*, 32:436–444, 1945.

[10] S.L. Dixon. *Fluid Mechanics, Thermodynamics of Turbomachinery*. Butterworth-Heinemann, 1998.

[11] S. Lieblein, Schwenk F.C., and R.L. Broderick. Diffusion factor for estimating losses and limiting blade loadings in axial-flow-compressor blade elements. Research Memorandum E53D01, NACA, Cleveland, Ohio, June 1953.

[12] J.C. Emery, L.J. Herrig, and Felix A.R. Erwin J.R. Systematic two-dimensional cascade tests of naca 65-series compressor blades at low speeds. Technical paper, NACA, 1951.

[13] H. Starken, F.A.E. Breugelmans, and P. Schimming. Investigation of the axial velocity density ratio in high turning cascades. *American Society of Mechanical Engineers*, 1975.

[14] N.A. Cumpsty. *Compressor aerodynamics*. Longam Scientific and Technical, 1989.

[15] W. Heilmann, H. Starken, and H. Weyer. Cascade wind tunnel tests on blades designed for transonic and supersonic compressors. In *AGARD Conference Proceeding*, volume 34.

[16] Schwenk F. C. and G. W. Jr. Lewis. Experimental investigation of a transonic axial-flow-compressor rotor with double-circular-arc airfoil blade sections: comparison of blade-element performance with three levels of solidity. Research Memorandum E55F01, NACA, Cleveland, Ohio, June 1955.

[17] Schwenk F.C. and G.W.Jr. Lewis. Experimental investigation of a transonic axial-flow compressor rotor with 1.5-chord length and aspect ractio of 3.0: Iii-blade element and over-all performance at three level of solidity. Research Memorandum E56D06, NACA, Cleveland, Ohio, August 1956.

[18] R.J. Robbins, W.H.and Jackson and S. Lieblein. *Aerodynamic design of axial-flow compressor*, 1965. NASA SP-36.

[19] R.M. Standahar and G.K. Serovy. Some effect of changing solidity by varying the number of blades on performance of an axial flow compressor stage. Research memorandum E52A31, NACA, Cleveland, Ohio, Aprile 1952.

[20] A. A. Medeiros and J. E. Hatch. Effect of various blade modifications on performance of a 16-stage axial-flow compressor. Research memorandum E52A31, NACA, Cleveland, Ohio, 1952.

[21] R.C. Turner and R.A. Burrows. The low speed performance of low stagger compressor blading at three pitch/chord ratios. Technical report, NGTE, 1960.

[22] R.D. Moore, W.M. Osborn, and D.C. Urasek. Performance of a single stage transonic compressor with a blade-tip solidity of 1.3. Technical memorandum, NASA, 1972.

[23] R.D. Moore, W.M. Osborn, and D.C. Urasek. Performance of a single stage transonic compressor with a blade-tip solidity of 1.5 and comparison with 1.3-1.7 solidity stages. Technical memorandum, NASA, 1973.

[24] R.D. Moore, W.M. Osborn, and D.C. Urasek. Performance of a single stage transonic compressor with a blade-tip solidity of 1.7. Technical memorandum, NASA, 1972.

[25] A.B. McKenzie. The selection of fan blade geometry for optimum efficiency. In *Proceedings of institution of mechanical engineering*, 1988.

[26] R.M. Hearsey. Practical compressor aerodynamic design. In *Advanced topics in turbomachinery design*. 1986.

[27] G.L. Liu. Simple formulae for optimal solidity of two-dimensional compressor cascades based on diffusion concept. *International Journal of Turbo and Jet engines*, 1993.

[28] A.B. McKenzie. The design of axial compressor blading based on tests of a low speed compressor. In *Proceedings of institution of mechanical engineering*, 1980.

[29] NUMECA International. *User Manual Autogrid5^{TM} v 8, Automated Grid Generator for Turbomachinery*, 2010.

[30] NUMECA International. *Theorethical Manual FINE^{TM} /Turbo v 8.7, Flow Integrated Environment.*

[31] D.C. Wilcox. *Turbulence modelling for CFD*. 2006.

[32] NUMECA International. *User Manual FINE^{TM} v 8, Flow Integrated Environment*, 2010.

[33] W.R. Britsch, W.M. Osborn, and M.R. Laessing. Effects of diffusion factor, aspect ratio and solidity on overall performance of 14 compressor middle stages. Technical paper 1523, NASA, Cleveland, Ohio, September 1979.

[34] J.P. Gostelow. *Cascade aerodynamics*. Pergamon press, Sidney, 1983.

[35] J. H. Horlock. *Axial flow compressors, fluid mechanics and thermodynamics*. Butterworths Scientific Publications, 1958.

[36] A.J. Wennerstrom. Low aspect ratio axial flow compressors : why and what it means. *Journal of Turbomachinery*, 111(4):357–365, 1989.

[37] S. Lieblein. Loss and stall analysis of compressor cascades. *Journal of Basic Engineering*, 81(4):387–400, July 1959.

[38] P. Kundu and I. Cohen. *Fluid Mechanics*. Elsevier Academic Press, 2001.

[39] S. Lieblein. Incidence and deviation angle correlation for compressor cascades. *Journal of Basic Engineering*, 82(4):575–587, Sept 1960.

[40] C. Osnaghi. *Teoria delle turbomacchine*. Esculapio, 2002.

[41] Fluent inc., Centerra Resource Park 10 Cavendish Court Lebanon, NH 03766. *Fluent 6.3 User's guide*, September 2006.